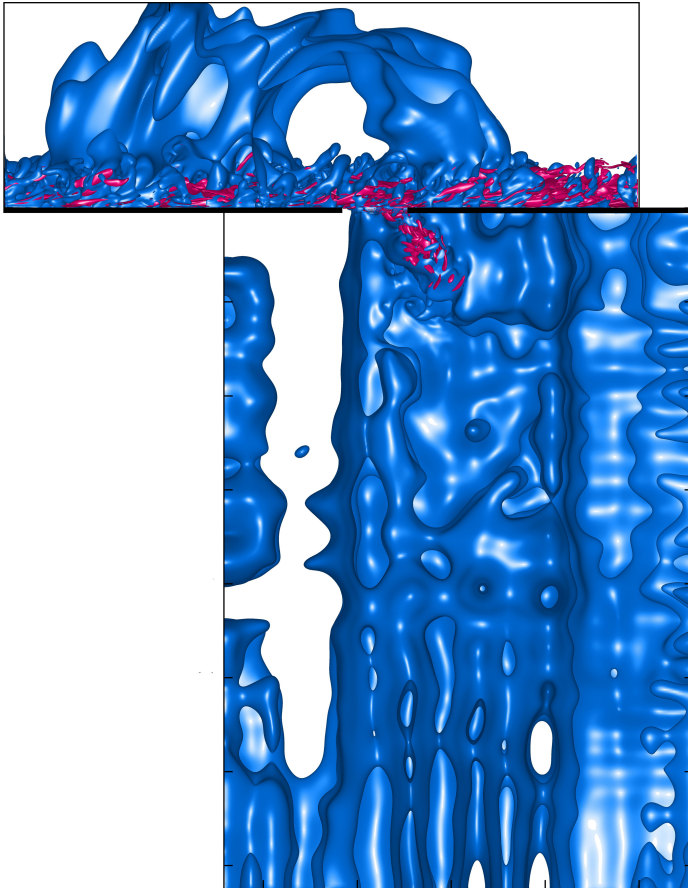


Lewin Stein

# Simulation and Modeling of a Helmholtz Resonator under Grazing Turbulent Flow



The front ( $xy$ -view) and back cover ( $xz$ -view) show two instantaneous isosurfaces resulting from a Direct Numerical Simulation of a Helmholtz resonator excited by grazing turbulent flow: the vorticity isosurface with  $|\nabla \times \mathbf{u}| = 3000 \text{ Hz}$  ( $St_{neck} = \pm 2.80$ ) is pink; the pressure isosurface with  $p = 100\,010 \text{ Pa}$  is blue; walls are black. In the back cover, a white rectangle highlights the underlying opening of the Helmholtz resonator. To simulate 40 ms of physical time,  $7 \times 10^6$  CPU-hours with a grid composed of  $1.2 \times 10^9$  gridpoints are invested.

# Simulation and Modeling of a Helmholtz Resonator under Grazing Turbulent Flow

vorgelegt von  
M. Sc. Lewin Stein  
geb. in Vorwerk



von der Fakultät V - Verkehrs- und Maschinensysteme  
der Technischen Universität Berlin  
zur Erlangung des akademischen Grades

Doktor der Naturwissenschaften  
Dr. rer. nat.

genehmigte Dissertation

Promotionsausschuss

Vorsitzender: Prof. Dr.-Ing. habil. Manfred Zehn  
Gutachter: Prof. Dr. sc. techn. habil. Jörn Sesterhenn  
Gutachter: Prof. Dr.-Ing. Jan Delfs  
Gutachter: Dr. Ph.D Peter Jordan

Tag der wissenschaftlichen Aussprache: 14.12 2018

Berlin 2019

This work was carried out at the Numerical Fluid Dynamics group of



cf<sup>d</sup> | caa

INSTITUTE OF FLUID DYNAMICS  
AND TECHNICAL ACOUSTICS

---

Comments or corrections are always welcome and can be sent to  
lewinstein(at)web.de.

<https://doi.org/10.14279/depositonce-8183>

DepositOnce  
Repositorium der Technischen Universität Berlin  
Germany

This work is licensed under a  
Creative Commons Attribution-ShareAlike 4.0 International License.



# Abstract

When gas flows along a surface containing a cavity or gap, this fluid-dynamical process is likely linked with acoustical effects. Primarily, in the transport and energy sector, the phenomenon occurs frequently: gas flows around land and air vehicles or streams inside duct systems and engines. A key challenge for these examples is either to prevent cavity noise before it arises or to reduce existing tonal noise by installing a cavity absorber.

The present thesis deals with a Helmholtz resonator beneath a turbulent flat plate flow. This representative example includes all the mentioned phenomena of acoustic excitation or damping under realistic conditions.

For the first time, a Direct Numerical Simulation of a three-dimensional Helmholtz resonator excited by a turbulent flow is conducted, and an unprecedented database is set up. To effectively simulate on a high performance computing center, a multi-block parallelization method is developed and implemented for complex geometries.

A universal acoustic model of the Helmholtz resonator under grazing flow is derived, based on the new numerical database, previous theories by Howe, and experiments by Golliard. This acoustic model stands out through its uniquely defined and physically meaningful parameters, instead of fitted constants. Utilizing the lumped element method, the model consists of exchangeable impedance elements which guarantee a flexible use.

---

The model enables the user to understand and to trace back how a modification of design parameters like the spatial form or the type of incoming flow affects the sound spectrum. The model is validated for low Mach number flows ( $M=0.01-0.14$ ) and frequencies around the Helmholtz resonator base frequency. Hence, an industrial user is no longer dependent on expensive and time-consuming test series within this typical range of operation. A priori, rather than by trial-and-error approach, the sound absorption spectrum can be easily tuned for specific frequencies.

Consequently, the developed model simplifies the design process of cavity absorbers. Furthermore, the model predicts fluid and acoustic resonance conditions and such allows the design engineer to avoid tonal cavity noise in advance. In doing so, the user of the model can circumvent noise pollution and material wear before it occurs.

# Zusammenfassung

Wenn Gas über eine Fläche strömt, die einen Hohlraum oder Spalt aufweist, ist dieser fluiddynamische Prozess oft mit akustischen Effekten gekoppelt. Insbesondere in der Transport- und Energiebranche tritt das Phänomen häufig auf: Hier strömt Gas um Land- und Luftfahrzeuge oder innerhalb von Rohrsystemen und Motoren. Ein zentrales Anliegen bei diesen Beispielen ist es, die Entstehung von Hohlkammer-Lärm zu verhindern oder bereits bestehende Töne durch die Installation von Hohlkammerabsorbern zu reduzieren.

Die vorliegende Dissertation beschäftigt sich mit einem Helmholtzresonator, angeströmt durch eine turbulente Plattenströmung. Dieses repräsentative Beispiel beinhaltet all die genannten Phänomene von Schallerzeugung sowie von Schalldämpfung unter realitätsnahen Bedingungen.

Erstmalig wird eine Direkte Numerische Simulation eines dreidimensionalen Helmholtzresonators, welcher durch turbulente Strömung angeregt ist, durchgeführt und eine Datenbasis aufgebaut. Um die Simulation effizient auf einem Höchstleistungsrechenzentrum auszuführen, wird eine Multi-Block-Parallelisierungsmethode für komplexe Geometrien entwickelt und implementiert.

Ein universelles, akustisches Modell des überströmten Helmholtzresonators wird basierend auf der neuen numerischen Datenbasis, auf bisherigen Theorien von Howe und auf Experimenten von Golliard hergeleitet. Das akustische Modell hebt sich hervor durch seine eindeutig definierten und physikalisch aussagekräftigen Parameter, anstatt durch angepasste Konstanten. Durch die Verwendung von austauschbaren, konzentrierten Impedanzelementen ist das Modell variabel einsetzbar.

---

Mit Hilfe des Modells kann verstanden und nachverfolgt werden, wie eine Änderung von Auslegungsparametern (z.B. von Geometrie oder der Art der einfallenden Strömung) auf das Klangspektrum wirkt. Das Modell ist für kleine Machzahlen ( $M=0.01-0.14$ ) und für Frequenzen nahe der Helmholtzresonator Grundfrequenz validiert. Innerhalb dieses typischen Betriebsbereiches ist ein Anwender somit nicht mehr auf aufwändige Versuchsreihen angewiesen. Ohne Versuche kann das Schallabsorptionsspektrum direkt auf bestimmte Frequenzen abgestimmt werden.

Damit wurde ein Modell entwickelt, welches die Auslegung von Hohlkammerabsorbern vereinfacht. Außerdem kann das Modell fluid-dynamische sowie akustische Resonanzbedingungen vorhersagen und erlaubt es dem Konstruktionsingenieur, Pfeifen von Kavitäten schon vor dem ersten Praxis-Test zu vermeiden. So kann Lärmbelastung und Materialabnutzung verhindert werden, bevor sie entsteht.

# Acknowledgements

Firstly, I would like to express my gratitude to those, with whom I discussed the matter of this thesis and who contributed with their ideas: my advisor Prof. Jörn Sesterhenn, my committee members Prof. Manfred Zehn, Prof. Jan Delfs and Dr. Peter Jordan, the researchers outside my group Dr. Joachim Golliard, Dr. Klaus Ehrenfried and Dr. Michael Schlegel and especially my friends and colleagues Prof. Julius Reiss, Dr. Juan Jose Pena Fernandez, Dr. Mathias Lemke, Dr. Jens Brouwer, Gabriele Camerlengo, Laurent Bernier, Sergio Bengoechea Lozano, and Sophie Knechtel.

Second, I am grateful for the financial support I got in the past five years: the scholarship by the Elsa-Neumann-Stipendium (formally known as NaFöG), and the funding through the two projects “Acoustic Investigation of a Hollow Chamber in Turbulent Flow” (Project identifier 378373148), “Shape Optimization and Sensitivity Analysis of a Liner under Grazing Flow” (Project identifier 265959900) granted by the German Research Foundation (DFG).

Third, I want to acknowledge the enormous computational resources provided by the High-Performance Computing Center Stuttgart (ACID11700), the Leibniz Supercomputing Centre (pr83gi), and the North-German Supercomputing Alliance (beistein).

My special thanks go to my “Muck-Schnuck”.



# Table of Contents

<b>Abbreviations</b>	<b>v</b>
<b>Symbols</b>	<b>vii</b>
<b>1 Introduction</b>	<b>1</b>
1.1 Motivation . . . . .	1
1.2 State of the Art . . . . .	2
1.3 Objective . . . . .	8
1.4 Outline . . . . .	10
<b>2 Object of Research</b>	<b>13</b>
2.1 Auxiliary Case: Turbulent Flow over a Flat Plate . . . . .	13
2.2 Main Case: Helmholtz Resonator under a Grazing TBL	14
<b>3 Fluid Dynamical Theory</b>	<b>17</b>
3.1 Compressible Navier-Stokes Equations . . . . .	17
3.2 Turbulent Boundary Layer . . . . .	23
<b>4 Acoustical Theory and Modeling</b>	<b>29</b>
4.1 Acoustic Wave Equation . . . . .	30
4.2 Lumped-Element Method . . . . .	32
4.2.1 Generic Helmholtz Resonator Model . . . . .	37
4.2.2 Generic Helmholtz Resonator Model Applications	38
4.3 The New Helmholtz Resonator Model . . . . .	41
4.4 Howe’s Conductivity Model of an Opening . . . . .	43
<b>5 Computational Fluid Dynamics</b>	<b>49</b>
5.1 Direct Numerical Simulation Method . . . . .	49
5.2 Skew-Symmetric Compressible Navier-Stokes Equations	51
5.3 Direct Numerical Simulation Setup . . . . .	53

## TABLE OF CONTENTS

---

<b>6</b>	<b>Modal Analysis</b>	<b>61</b>
6.1	Dynamic Mode Decomposition . . . . .	61
6.2	Resolvent Analysis . . . . .	67
<b>7</b>	<b>Fluid Dynamical Results and Discussion</b>	<b>69</b>
7.1	Mean Velocity Profiles . . . . .	70
7.2	Instantaneous Velocity Fluctuations . . . . .	76
7.3	Turbulent Boundary Layer Spectra . . . . .	82
7.3.1	The $k_x - \omega$ -Spectrum . . . . .	82
7.3.2	Goody's Spectral Turbulent Boundary Layer Model	87
7.4	New Method to set Howe's Mean Velocities . . . . .	89
7.4.1	General Turbulent Convection Velocity . . . . .	89
7.4.2	Specification of Howe's Mean Velocity . . . . .	91
7.4.3	Specification of Howe's Velocity Ratio . . . . .	97
<b>8</b>	<b>Acoustical Results and Discussion</b>	<b>99</b>
8.1	Helmholtz Resonator Model with New Parameters . . . . .	99
8.2	Model Interpretation, Validation, and Validity Range . . . . .	101
8.2.1	Flow-Acoustic Interaction Impedance . . . . .	101
8.2.2	A New View on the Model Parameters $u_+, \beta$ . . . . .	103
8.2.3	Validation of the Helmholtz Resonator Model . . . . .	105
8.2.4	Validity Range of the Model . . . . .	107
8.3	Influence of the Boundary Layer Thickness on $u_+$ . . . . .	110
8.4	Spectral Analysis . . . . .	112
8.4.1	Dynamic Mode Decomposition of Pressure . . . . .	115
8.4.2	Identification of Kelvin-Helmholtz Waves . . . . .	117
8.4.3	Vortex Sheet Displacement . . . . .	120
8.4.4	Resolvent Analysis of Characteristic Frequencies . . . . .	122
<b>9</b>	<b>Conclusion</b>	<b>125</b>

---

## TABLE OF CONTENTS

---

<b>Appendix A Thermodynamics</b>	<b>129</b>
A.1 The Ideal Gas . . . . .	129
<b>Appendix B Finite Differences</b>	<b>133</b>
B.1 Finite Differences Derivation Schemes . . . . .	134
B.2 Fully Conservative Finite Differences . . . . .	138
B.3 Challenges of Skew-Symmetric Finite-Differences . . . . .	141
<b>Appendix C Boundary Conditions</b>	<b>145</b>
C.1 Method of Characteristics . . . . .	145
C.2 Non-Reflective Boundary Conditions with Characteristics	150
C.3 Non-Reflecting Boundary Conditions with a Sponge Layer	152
C.4 Symmetric Boundary Condition: Adiabatic, No-Slip Wall	154
<b>Appendix D Parallelization</b>	<b>155</b>
D.1 Single-Block Parallelization . . . . .	155
D.2 Multi-Block Parallelization . . . . .	156
D.3 Scaling Tests . . . . .	157
<b>My Publications</b>	<b>161</b>
Original Papers . . . . .	161
Conferences . . . . .	162
Supervised Master Theses . . . . .	163
<b>References</b>	<b>165</b>



# Abbreviations

<b>DFT</b>	Discrete Fourier Transformation
<b>DMD</b>	Dynamic Mode Decomposition
<b>DNS</b>	Direct Numerical Simulation
<b>FDM</b>	Finite Differences Method
<b>FP</b>	Flat Plate
<b>HR</b>	Helmholtz Resonator
<b>KH</b>	Kelvin-Helmholtz
<b>NSE</b>	Navier-Stokes Equation
<b>PDE</b>	Partial Differential Equation
<b>SPL</b>	Sound Pressure Level
<b>TBL</b>	Turbulent Boundary Layer
<b>ZPG</b>	Zero Pressure-Gradient



# Symbols

$He_{cavity}$	Helmholtz number of the cavity depth mode $f L_{y-cavity}/c$	
$K_R$	Rayleigh conductivity (Eq. 4.29)	$\text{Pa s m}^{-3}$
$M_0$	free-stream Mach number $u_0/c$	
$Pr$	Prandtl number (Eq. 3.17)	
$R_s$	specific gas constant (Eq. A.2)	$\text{m}^2 \text{s}^{-2} \text{K}^{-1}$
$Re_\tau$	friction Reynolds number $u_\tau \delta_{99}/\nu = \delta_{99}/\delta_\nu$	
$St_{TBL}$	Strouhal number of the TBL $f \delta_{99,neck}/u_0$	
$St_{neck}$	Strouhal number of the neck $f L_{x-neck}/u_+$	
$S$	surface	$\text{m}^2$
$T$	temperature	K
$Y$	characteristic impedance $Y = \rho c/S$	$\text{Pa s m}^{-3}$
$Z$	acoustic impedance $Z = (r + ik\delta)Y$	$\text{Pa s m}^{-3}$
$\beta$	frequency dependent tuning of the opening impedance amplitude, redefined by Eq. 7.8	
$\delta_\nu$	viscous lengthscale $\nu/u_\tau$	m
$\delta_{99,neck}$	boundary layer thickness $\delta_{99}$ at the neck center (Fig. 2.1)	m
$\delta_{99}$	boundary layer thickness $u(y = \delta_{99}) = 0.99 u_0$	m
$\delta$	reactance, i.e., length correction (phase shift)	m
$\gamma$	adiabatic exponent (Eq. A.11)	
$\lambda$	wavelength $\lambda = c/f$	m
$\mu$	dynamic viscosity of molecular shear forces $\mu = \rho \nu$	$\text{kg}/(\text{m s})$
$\nu$	kinematic viscosity of molecular shear forces	$\text{m}^2/\text{s}$
$\omega$	angular frequency $\omega = 2\pi f$	$\text{rad/s}$

## Symbols

---

$\rho$	density	kg/m <sup>3</sup>
$\tau_w$	wall shear stress $\rho_w \nu d/dy < u_x >  _{y=y_w}$	Pa
$\mathbf{u}$	velocity	m/s
$c$	speed of sound (Eq. 4.4)	m/s
$f$	frequency $f = c/\lambda$	1/s
$k_q$	heat conductivity	m kg s <sup>-3</sup> K <sup>-1</sup>
$k_x$	streamwise component of the wave vector	rad/m
$k$	angular wavenumber $k = 2\pi/\lambda$	rad/m
$p$	absolute pressure	Pa
$r$	resistance, i.e., excitation or damping	
$u_+$	mean vortex sheet velocity driving KH waves, redefined by Eq. 7.6 or specifically in the present case by Eq. 7.7	m/s
$u_0$	free stream velocity	m/s
$u_\tau$	wall friction velocity $\sqrt{\tau_w/\rho_w}$	m/s
$v'$	acoustic volume flux	m <sup>-1</sup> s <sup>-1</sup>

“In every sound, the hidden silence sleeps.”

Dejan Stojanovic



# Introduction

# 1

This chapter first demonstrates the practical significance of flow-excited cavity oscillations. Then the current state of research is outlined, and the need for a numerical database (methodological groundwork) and a more general model (final goal of this work) is explained. Finally, this chapter gives an overview of the structure of this thesis, i.e., the further strategy to reach the final goal.

## 1.1 Motivation

Typically, when gases (compressible fluids) stream along a cavity-like space, acoustical resonances arise, which often couple with the detached vortices of the upstream cavity edge. Many examples can be listed in which this coupling of the turbulent flow and the acoustics is of greatest importance:

Noise silencers consisting of cavity arrays (so-called Liners) are flush-mounted in most duct systems, in which tonal noise due to a constant operating frequency needs to be reduced, among others: air conditioning systems, ventilation plants, and various combustion engines ranging from ship diesel engines to jet engines.

Beside silencing properties, cavities or gaps may give rise to desirable tones of wind instruments like transverse flutes and organs or undesired cavity noise of moving objects: contact gap noise of doors or hatches in general, aircraft noise caused by open wheel bays during take-off and landing, wheelhouse noise, window buffeting or sunroof buffeting of moving vehicles, and noise of gaps between train coaches. Acoustic

## 1. Introduction

---

cavity resonances may even cause material damage for instance in pipeline intersections (Dequand et al., 2003a; Radavich et al., 2001).

In all these examples, usually, the gas grazes fully turbulently over the surface of the respective objects.

## 1.2 State of the Art

The sound generation and sound absorption of a cavity under grazing turbulent flow can be classified by three mechanisms. This section explains these three mechanisms, depicted in Fig. 1.1. The characteristic system scales are the incoming sound wave  $\lambda_{in}$ , the acoustic eigenmodes of the cavity  $\lambda_{n_x n_y n_z}$  and the shear-layer feedback length scale  $\lambda_{KH}$  of the vorticity generation and the vorticity decay at the cavity opening. The left column of Fig. 1.1 shows the energy sources of the system: the (turbulent) base flow or the acoustical perturbation, or both. The left middle column of Fig. 1.1 sketches the three mechanisms itself. The right middle column of Fig. 1.1 states the Eq. to predict the resonance frequency (expressed as Strouhal number or Helmholtz number), corresponding to each mechanism. The right column of Fig. 1.1 describes the resulting damping (green arrows) or excitation (red arrows). This classification is based on Elder (1978); Howe (1997a); Rockwell and Naudascher (1979) and Ma et al. (2009).

**I The fluid-dynamical mechanism** (at the top of Fig. 1.1) describes the horizontal feedback of whirls inside the shear layer in between the upstream separation edge and the downstream edge of the neck (neglecting the cavity). It is also known as **Rossiter** mechanism. The impinging vortex at the downstream edge triggers an acoustic wave, which propagates upstream, phase and frequency locks the upstream vortex separation and thus synchronizes the Kelvin-Helmholtz (KH)

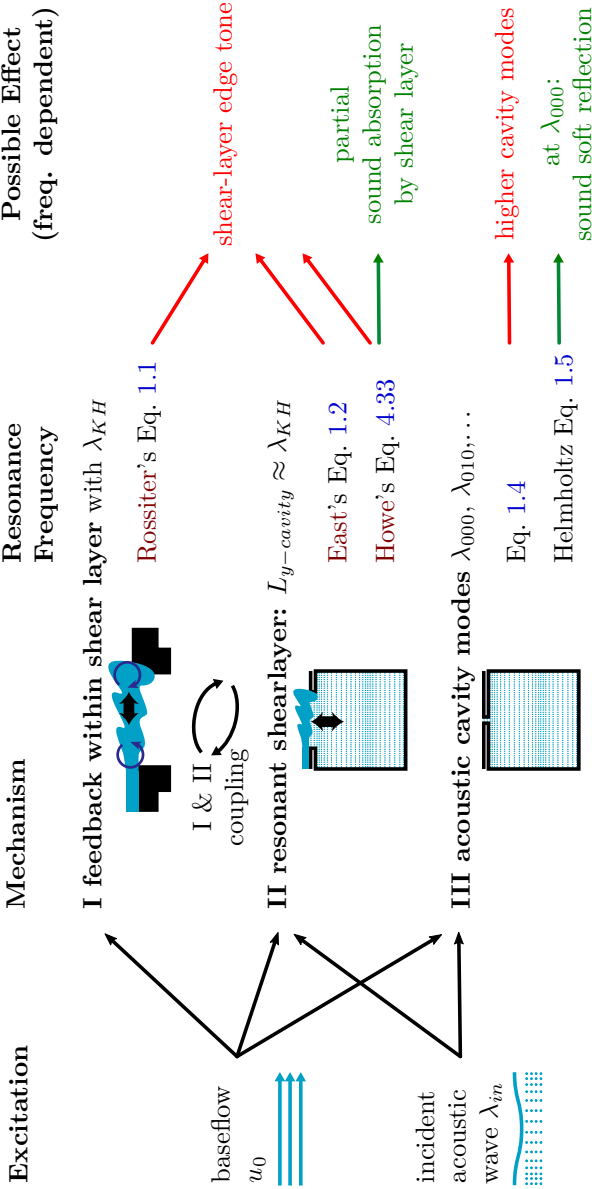


**Figure 1.1:** Overview of classical models which describe the acoustical response of a cavity or orifice. Red arrows denote sound generation. Green arrows imply sound absorption. The orientation of bold black left-right-arrows within the sketches of the mechanisms indicates whether a horizontal coupling within the shear layer or a vertical coupling between the shear layer and the cavity eigenmodes dominates.

## 1. Introduction

---

waves of the shear layer. The Strouhal number of the KH waves (edge tone) for an opening of the streamwise length  $L_{x-neck}$ , overflown by a free stream velocity  $u_0$  according to [Rossiter \(1964\)](#) is

$$\frac{f_{KH} L_{x-neck}}{u_0} = \frac{n - \gamma_{KH}}{M_0 + u_0/u_c}, \quad (1.1)$$

being  $M_0$  the free-stream Mach number,  $n$  the KH mode number,  $u_c$  the average, convective velocity of the whirls and  $\gamma_{KH}$  the delay between the impinging of the vortex and the generation of the edge tone. [Rossiter](#) fitted  $\gamma_{KH} = 0.25$  and  $u_c = 0.57u_0$ . Traditionally, the best match of Eq. 1.1 with experiments is shown for  $M_0 > 0.2$  ([Ahuja and Mendoza, 1995](#)). Low Mach number experiments often contain more scattering ([Rowley et al., 2002](#)). More recently, [Yamouni et al. \(2013\)](#) demonstrated, that the Rossiter mechanism is also valid for  $M_0 = 0$  with instantaneous pressure feedback. They show, that the smaller the Mach number, the higher the numbers of the dominant Rossiter modes.

**II The fluid-resonant mechanism** (in the middle of Fig. 1.1) represents the vertical coupling of the shear layer waves  $\lambda_{KH}$  with the modes of the cavity  $\lambda_0$ . Thereby, the horizontal feedback within the shear layer itself (Rossiter mechanism I) is not considered. This fluid-resonant mechanism II is studied among others by [Koch \(2005\)](#); [Rockwell \(1977\)](#) and [Brès and Colonius \(2008\)](#). Here the cavity has a similar dimension as the KH wavelength of the shear layer:  $\lambda_0 \sim \lambda_{KH}$ . Higher cavity modes may interact with higher KH modes, too. The first mode of a rectangular, open cavity (without a cavity cover or bottleneck) is estimated by [East \(1966\)](#) as a function of the cavity

length-depth ratio  $L_{x-cavity}/L_{y-cavity}$ :

$$\frac{f_{east} L_{x-cavity}}{u_0} = \frac{\gamma_{east}}{M_0 (1 + A(L_{x-cavity}/L_{y-cavity})^B)}. \quad (1.2)$$

Again  $\gamma_{east} = 0.25$  stands for a delay of sound generation after a vorticity decay.  $A = 0.65$  and  $B = 0.75$  are fitted constants.

**Coupling of the fluid-dynamical and the fluid-resonant mechanism (I & II)** occurs if the KH wavelength of the shear layer coincides with acoustic cavity resonances. This can lead to an extreme non-linear amplification of the participating modes as experimentally investigated by [Elder et al. \(1982\)](#); [Gloerfelt and Lafon \(2008\)](#) and [Ma et al. \(2009\)](#). Overview articles of the fluid-dynamical, acoustic-resonant coupling regime are written by [Howe \(1998\)](#) and [Gloerfelt \(2009\)](#). [Tam and Block \(1978\)](#) predict the common coupling frequency of both mechanisms with

$$\frac{f_{block} L_{x-neck}}{u_0} = \frac{n}{M_0 (1 + A(L_{y-cavity}/L_{x-cavity})) + u_0/u_c}, \quad (1.3)$$

being  $n$  the cavity mode,  $u_c$  the average, convective velocity and  $A = 0.514$  an empirical parameter.

Eq. 1.1, Eq. 1.2 and the combined Eq. 1.3 only predict the possible occurrence of tones driven by the base flow. Moreover, the fluid-dynamical and the fluid-resonant mechanism may include the alteration of external sound waves, which are passing through the shear layer of the cavity opening. Due to the possible coupling of incoming sound waves and shear layer structures (KH waves) acoustic energy and kinetic energy of whirls may be interchanged. For example, in the case of a grazing turbulent boundary layer, broadband noise is always present, which penetrates the shear layer and enters the cavity. This

## 1. Introduction

---

is measured, among others, by [Golliard \(2002\)](#); [Kook and Mongeau \(2002\)](#) and [Hémon et al. \(2004\)](#). A more general theory of plane acoustic waves transversing the shear layer is developed by [Howe \(1997a, 1981a,b, 1997b\)](#) and [Grace et al. \(1997\)](#). They predict the damping or excitation of transmitted acoustic waves in the framework of linear theory, assuming an infinitely thin shear layer with a constant eddy convection velocity  $u_c$ . If the incoming boundary profile thickness becomes smaller compared to the streamwise dimension of the cavity opening, larger momentum components can penetrate in the cavity opening. Hence, it remains to clarify to which extend the assumption of an infinitely thin shear layer is valid. Sect. 4.4 continues this discussion in more detail.

**III The acoustical mechanism** (at the bottom of Fig. 1.1) deals with pure acoustic waves in an almost closed cavity except for a small neck opening (without mean flow). In three dimensions higher cavity eigenmodes are expected at the frequencies ([Ehrenfried, 2004](#))

$$\frac{f_{n_x n_y n_z}}{c} = \frac{1}{2} \sqrt{\left(\frac{n_x}{L_{x\text{-cavity}}}\right)^2 + \left(\frac{n_y}{L_{y\text{-cavity}}}\right)^2 + \left(\frac{n_z}{L_{z\text{-cavity}}}\right)^2}, \quad (1.4)$$

being  $n_x$ ,  $n_y$  and,  $n_z$  the mode numbers. Below the cutoff frequency of these higher modes, the only mode, which is capable of propagating always, is the so-called Helmholtz base frequency  $f_{000}$  (pipe tone). In contrast to Eq. 1.4, the Helmholtz wavelength  $\lambda_{000}$  is larger than all cavity dimensions. The analogous mechanical model of a cavity resonating at its base frequency is a frictionless mass-spring system. The compressible gas inside the cavity acts as a spring; while the gas in the cavity opening corresponds to a mass. The resonance is given by

(Ehrenfried, 2004)

$$\frac{f_{000}L_{y-neck}}{c} = \frac{1}{2\pi} \sqrt{\frac{A_{neck}L_{y-neck}}{V_{cavity}}}. \quad (1.5)$$

$V_{cavity}$  is the cavity volume.  $A_{neck} = L_{x-neck}L_{z-neck}$  is the cross-section of the neck and  $L_{y-neck}$  is the height of the neck. In practice, to match more realistic conditions with this idealized system a length correction of  $L_{y-neck}$  is introduced. Tang (2005) investigated the influence of the particular design of the neck geometry. Nonlinear extension of Eq. 1.5 are provided by Hersh et al. (2003); Hirschberg and Rienstra (2017).

If an acoustically resonant cavity is mounted in the wall of a duct system, incoming sound waves with the wavelength  $\lambda_{in}$  are superimposed with anti-phase waves radiated by the cavity. Such the cavity acts as a sound-soft element (Iqbal and Selamet, 2010). Perfect phase inversion takes place precisely at the (Helmholtz) resonance frequency  $\lambda_{in} = f_{000}$ . Downstream in the duct, destructive interference leads to sound extinction, all the acoustic energy is reflected upstream.

Commonly, the damping or excitation is a superposition of all these mechanisms, because their scales (i.e., wavelengths) overlap. Especially the possible nonlinear interplay of multiple mechanisms is theoretically little studied and is analyzed in this work.

### 1.3 Objective

Cavities under grazing turbulent flow are commonly surveyed, mostly for industrial applications. In practice, numerous series of many different cavity configurations are experimentally tested for a particular design goal, e.g., noise canceling in [Dequand et al. \(2003b\)](#). An understanding of the underlying physical processes, especially of the complex acoustic turbulence interaction is missing. Hence, there is a lack of easy applicable but realistic models, which are not dependent on expensive parameter studies. Mostly, the resonance frequencies but not the amplitudes are predicted. Models which can predict the sound pressure level (SPL), too, usually are either based on theoretical simplifications ([Howe, 1981a,b](#)) or rely on empirical fits ([Golliard, 2002](#)). So far studies of cavities driven by turbulent flow are predominantly based on experiments. Other researchers conducted some numerical simulations, but with limitations. Often, only open cavities without a neck or ceiling are studied ([Gloerfelt et al., 2002](#)). In case a cavity with a neck is considered the inflowing Turbulent Boundary Layer (TBL) is often missing ([Roche et al., 2009](#); [Tam et al., 2005, 2010](#)) or not all system scales are resolved, but some form of turbulence model is assumed ([Eldredge et al., 2007](#)).

#### **Methodological Groundwork: Numerical Database Creation**

The first step of this work is to conduct for the first time a Direct Numerical Simulation (DNS) of a detailed three-dimensional geometry of a Helmholtz resonator excited by a grazing, turbulent boundary layer flow. “Helmholtz resonator” means a partially closed cavity except for a neck opening (see Sect. 2.2). Because of the expected non-linear coupling of the fully turbulent shearing flow and the sound field in

the neck region, no turbulence model nor acoustic solver (Lighthill’s analogy) with source terms given by incompressible fluid flow is applied but the full compressible Navier-Stokes equations are solved in real space. In contrast to an experiment, a DNS provides a more comprehensive set of data, which is beneficial to set up a model.

### **Final Goal: Acoustic Model**

The final goal of this work is to derive a new substitute model of a Helmholtz resonator under grazing turbulent flow, which simplifies the design process and which is widely applicable due to a modular principle (Lumped-Element Method). In the case to be examined here, the thickness of the incoming TBL is smaller than the streamwise extension of the neck:  $\delta_{99,neck} < L_{x-neck}$ . As a consequence, a more unstable shear layer arises, and thus a strong turbulence-acoustic interaction at the neck area is expected (Sect. 8.3). Notably, the new model is specialized in this turbulence-acoustic interaction at the neck (see Sect. 4.4), in contrast to ordinary, purely acoustical descriptions.

Its refined parameters characterize the novelty of the model. The parameters are no longer meaningless fit parameters but replaced by clearly defined quantities with physical meaning. Thereby, the focus lies especially on the mean convection velocity, which is the key factor to model the acoustic impedance of a neck with a shear layer (Sect. 7.4).

The model is optimized for a low Mach number flow and low-frequency acoustics (i.e., around the base frequency of the Helmholtz resonator), which are typical operating conditions of duct systems. Chap. 4 explains these assumptions. The low-frequency range corresponds to the terminology “Helmholtz resonator”, which implies that the considered acoustic wavelengths are larger than the cavity dimensions (see mechanism III of Sect. 1.2).

### 1.4 Outline

This work is organized as follows:

**Chap. 2** specifies the principal research object, i.e., the Helmholtz resonator mounted in a flat plate with incoming turbulent flow. As a reference, a secondary case of a simple flat plate with turbulent flow is stated, too.

**Chap. 3** presents the compressible Navier-Stokes equations, which are the heart of the conducted simulations. For the mean velocity profile of a turbulent boundary layer, a semi-analytic solution is shown.

**Chap. 4** newly formulates an adaptable, model of a Helmholtz resonator. This model is based on the Lumped-Element Method (acoustical description) and Howe's conductivity model of an opening under grazing flow (significant fluid-acoustic interaction).

**Chap. 5** deals with the setup of the Direct Numerical Simulation. Resolution issues, initial and boundary conditions are treated. Particular attention is given to turbulence generation.

**Chap. 6** shows how to spectrally analyze and decompose a snapshot series of a dynamical system by a Dynamic Mode Decomposition and a Resolvent Analysis.

**Chap. 7** evaluates and discusses the numerical database from a fluid dynamical point of view. As validation, the mean velocity profile and the spectral pressure fluctuations are contrasted with theoretical solutions. The modifications of the fluid structures through the presence of the Helmholtz resonator are novelly revealed. Unique features of the shear layer at the opening of the Helmholtz resonator are found and utilized to replace model constants with more universal, innovative parameters.

**Chap. 8** evaluates and discusses the Helmholtz resonator model with its new parameters. Beside the present numerical results, other

experimental measurements are also consulted to demonstrate the model validity range depending on non-dimensional frequencies, Mach numbers, and boundary layer thicknesses. Characteristic system modes and resonances identified via the Helmholtz resonator model are confirmed by an independent Dynamic Mode Decomposition and a Resolvent Analysis.

**Chap. 9** summarizes the impact of both numerical groundwork and the acoustic model (final goal). The advantages of the new model above previous ones are shown. The significance and usability of the new model are discussed, concerning different acoustical and fluid-dynamical effects.

**Appx. A** outlines basic, thermodynamical principles of gas dynamics.

**Appx. B** introduces an entirely conservative Finite Differences Method and critically discusses its practical implementation.

**Appx. C** covers the numerical implementation of the boundary conditions.

**Appx. D** explains the newly programmed parallelization method for complex geometries. Scaling tests demonstrate the greater efficiency in contrast to the previous parallelization.



# Object of Research

# 2

The object of research, the Helmholtz resonator mounted in a flat plate with turbulent grazing flow is precisely specified in this chapter. In the following, this principal object of research is called in short HR. To separate effects, besides the main case of the Helmholtz resonator a second auxiliary case of a flat plate is set up, which the same incoming turbulent flow as the HR case. The auxiliary case will serve as a reference and is abbreviated as FP throughout this work. First, the FP case is introduced, followed by the HR case.

## 2.1 Auxiliary Case: Turbulent Flow over a Flat Plate

All physically systems in this work are excited by the incoming flat plate flow with the TBL, specified next. The mean flow streams unaccelerated in the positive  $x$ -direction with a zero-pressure-gradient (ZPG). The plane  $xz$ -plate is located at a constant height of  $y = 0$ . In the spanwise  $z$ -direction, the plate is infinite, i.e., continued periodically by the simulation. The bottom wall permits no heat flux (adiabatic), and all velocity components are zero (no-slip condition). Standard conditions of an ideal gas are selected (see also Eqs. 3.16, 3.17): the adiabatic exponent  $\gamma = 1.4$ , the specific gas constant  $R_s = 287 \text{ m}^2\text{K}^{-1}\text{s}^{-2}$ , the Prandtl number  $Pr = 0.71$ , the absolute pressure  $p_0 = 100 \text{ kPa}$ , and the temperature  $T_0 = 293 \text{ K}$ , which implies a speed of sound of  $c_0 = 343 \text{ m/s}$  (Eq. 4.5). The compressible, boundary layer streams with a low Mach

## 2. Object of Research

---

number of  $M_0 = 0.112$  ( $u_0=38,5$  m/s). A lower zero index defines all free stream properties. The TBL possesses fully developed turbulence, with a Reynolds number of  $Re_{\delta_{inlet}} = 2163$  concerning the boundary layer thickness at the inlet of  $\delta_{99,inlet} \cong 6$  mm. This corresponds to a friction Reynolds number of  $Re_{\tau} = 120$  for the wall friction velocity  $u_{\tau}$  (Eq. 3.19). Details how to numerically generate realistic turbulent inflow follow in Sect. 5.3.

## 2.2 Main Case: Helmholtz Resonator under a Grazing TBL

Fig. 2.1 provides a sketch of the main setup including the coordinate origin. The main HR case is driven by exactly the same TBL flat plate flow as the reference case of the last Sect. 2.1. In contrast to the FP case, now a partially closed Helmholtz resonator is flush-mounted inside the bottom wall at the spanwise center of the plate. A flat rectangular neck opening is connecting the upper TBL flow with the rectangular cavity below. The cavity is confined by adiabatic, no-slip walls, too. In the spanwise  $z$ -direction, both the neck and the cavity have the same extent:  $L_{z-neck} = L_{z-cavity} = 10.8\delta_{99,neck}$ . Whereas the spanwise extent of the upper flat plate is larger:  $L_{z-plate} = 1.17L_{z-neck} = 12.6\delta_{99,neck}$ . In the streamwise  $x$ -direction the opening  $L_{x-neck}$  is seven times smaller than the cavity length  $L_{x-cavity}$ , but one and a half times larger than the boundary layer thickness  $\delta_{99,neck} = 9,28$  mm =  $181\delta_{\nu}$  (measured in Sect. 7.1 at the center of the neck). The wall thickness between the TBL flow and the cavity is  $L_{y-neck} = 0.11\delta_{99,neck} = 19.5\delta_{\nu}$ . Since the boundary layer thickness at the neck center  $\delta_{99,neck}$  has grown

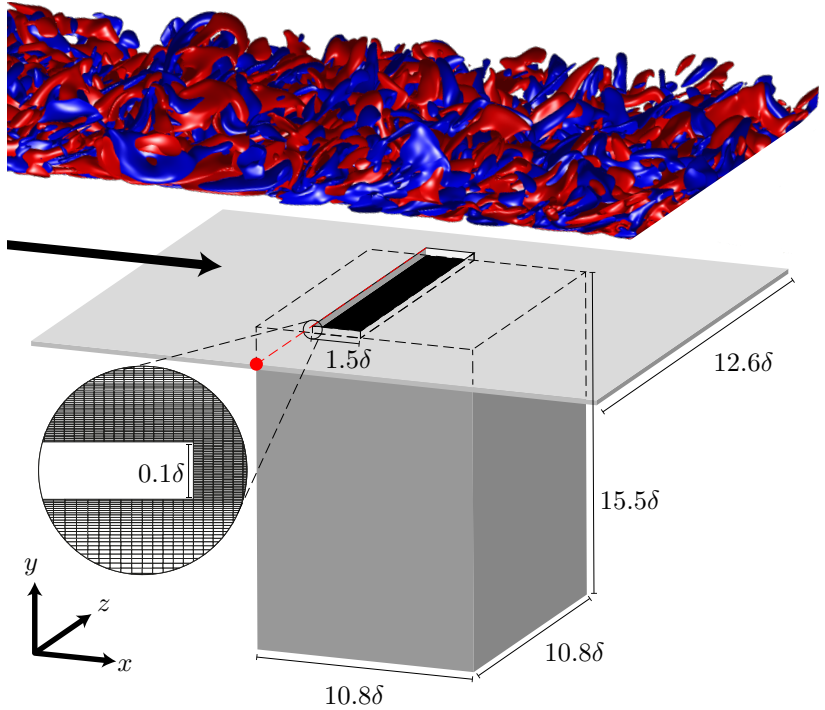


**Figure 2.1:** The main object of research, the Helmholtz resonator under grazing turbulent flow. At the top, vorticity isosurfaces ( $St_{neck} = \pm 2.80$  colored blue and red) of the turbulent boundary layer are visible. Below the flat plate flow, the rectangular cavity of the resonator is centrally mounted, connected by a flat rectangular neck opening. All units are given in terms of the boundary layer thickness, defined at the neck center  $\delta_{99,neck} = 9,28 \text{ mm} = 181\delta_\nu$ . Around the neck, the grid is further refined as indicated by the zoom window. The origin of the left-handed Cartesian coordinate system, used throughout the present work, is marked as a red dot. Its  $x$ - and  $y$ -position coincide with the upper leading edge of the neck, which is denoted by the dashed red line. Its  $z$ -position is located at the side edge of the flat plate, which is facing the observer (points forward in negative  $z$ -direction).

## 2. Object of Research

---

compared to the thickness  $\delta_{99,inlet}$  at the FP inlet, the neck Reynolds numbers are also increased by  $Re_{\delta_{99,neck}} = 3573$  and  $Re_{\tau} = 185$ .

As the reference FP case before, the main HR case is studied numerically for one single Mach number ( $M_0 = 0.11$ ). To conduct a DNS of 42 ms of physical time with a grid composed of  $1.2 \times 10^9$  gridpoints,  $7 \times 10^6$  CPU-hours were invested, and approximately 20 terabytes of data were stored. Due to the computational cost, a parameter study is only experimentally feasible. Sect. 5.3 provides details about the setup of the DNS and the needed resolution.

The HR setup is motivated by Golliard (2002) (cavity C1). Golliard experimentally investigated a Mach number range from 0.01 to 0.14 and  $\delta_{99,neck}/L_{x-neck}$  ratios from 0.7 to 5.5. In Sect. 8.2, this allows comparisons over a whole parameter range of the present HR DNS and of the newly developed HR model.

# Fluid Dynamical Theory

# 3

The following section introduces the most widespread model of continuous fluid motion: The Navier-Stokes equations, in the following abbreviated as NSEs. The second section of this chapter presents a semi-analytical, particular solution of the NSEs for a compressible TBL.

## 3.1 Compressible Navier-Stokes Equations

Computational capacities limit the full description of individual fluid molecules. In the case of particle motion with a short mean free path, the continuum approximation suggests itself. The NSEs are such a statistically averaged model of many-body interactions. This macroscopic point of view is the foundation of this work.

According to [L.D. Landau and E.M. Lifshitz \(2011\)](#) two scalar quantities, e.g., the density  $\rho$  and the pressure  $p$  and the vectorial velocity  $\mathbf{u}$  fully describe a fluid state (single phase and single substance).

First, the three conservation laws are outlined, which lead to the final form of the NSEs. In a second step, the obtained expressions are closed using an equation of state, i.e. a pressure-density relation. Every operator is considered to act on all multiplicative terms to his right side, irrespective of brackets<sup>1</sup>. Einsteins sum convention is used.

---

<sup>1</sup>For example,  $\nabla \mathbf{u}(a+b) = \partial_x u_x a + \partial_x u_x b + \partial_y u_y a + \partial_y u_y b + \partial_z u_z a + \partial_z u_z b$  is valid.

### 3. Fluid Dynamical Theory

---

#### Mass Conservation

The continuity equation represents the conservation of mass in a moving fluid. It has the differential form of

$$\partial_t \rho + \nabla \rho \mathbf{u} = 0. \quad (3.1)$$

The first term is the change of density  $\rho$  (mass per volume) in time. The second term states that this change of density depends only on incoming or outgoing mass flux.

#### Momentum Conservation

The compressible NSE describes the momentum conservation of a viscous fluid. It can be written in divergence form or equivalently in convective form, respectively:

$$\partial_t \rho u_i + \nabla \rho u_i \mathbf{u} + \partial_{x_i} p = \partial_{x_j} \tau_{ji}, \quad (3.2)$$

$$\rho \partial_t u_i + \rho \mathbf{u} \bullet \nabla u_i + \partial_{x_i} p = \partial_{x_j} \tau_{ji}, \quad (3.3)$$

for  $i = 1, 2, 3$  in three dimensions. In both forms, the first term describes the change of momentum  $\rho u_i$  in time (per volume), which is affected either by a momentum flux, a pressure gradient or friction forces (second term, third term, and fourth term, respectively). The dot product notation  $\mathbf{u} \bullet \nabla$  implies  $u_x \partial_x + u_y \partial_y + u_z \partial_z$ . Averaging Eq. 3.2 and Eq. 3.3 leads to

$$\frac{1}{2} (\rho \partial_t + \partial_t \rho) u_i + \frac{1}{2} (\rho \mathbf{u} \bullet \nabla + \nabla \rho \mathbf{u}) u_i + \partial_{x_i} p = \partial_{x_j} \tau_{ji}. \quad (3.4)$$

This form is of great importance for the later discretization. Multiplication by  $u_i$  and summation of all space dimensions reveals the kinetic energy  $\rho |\mathbf{u}|^2$  per volume element with  $|\mathbf{u}|^2 = \sum_i u_i^2$ .

### 3.1 Compressible Navier-Stokes Equations

---

Under the assumption of an isotropic Newtonian fluid, the friction term on the right side has the following properties: Translational and rotational forces are irrelevant, and the stress tensor  $\tau_{ji}$  is given only by a symmetric deformation tensor  $S$  (Anderson, 1991, Sect. 15.3). Thus only the cross gradient of velocities is taken into account. Using the dynamic viscosity  $\mu(p, \rho)$  and the pressure-viscosity  $\mu_p(p, \rho)$  (often referred to as bulk or dilatational viscosity) the stress tensor equation appears as

$$\tau_{ij} = 2\mu S_{ij} + \left( \mu_p - \frac{2}{3}\mu \right) S_{kk} \delta_{ij}, \quad (3.5)$$

with the symmetric deformation tensor:

$$S_{ij} = \frac{\partial_{x_j} u_i + \partial_{x_i} u_j}{2}. \quad (3.6)$$

The side diagonal terms of stress tensor  $S_{ij}$  are shear stresses. The diagonal terms of stress tensor  $S_{kk}$  stand for a compression or an expansion. In the case of shock waves and nonlinear sound waves, the pressure-viscosity  $\mu_p(p, \rho)$  represents dilatational effects for  $S_{kk}$ . In the present case of subsonic flow and linear sound propagation, this dilatation is neglected, i.e.,  $\mu_p(p, \rho) = 0$  (Stoke's hypothesis).

Friction leads to a conversion of macroscopic fluid structures governed by inertial forces to microscopic fluid structures governed by viscous forces (energy cascade of decreasing eddy sizes). The energy contained in the smallest scale (Kolmogorov scale), which is resolved by the NSEs, is finally released into heat (such as molecular vibrations). The ratio between the inertial forces acting at large scales and the viscous forces of the small scales is defined as Reynolds number

$$Re_{\mathcal{L}} = \frac{u_0 \mathcal{L}}{\nu}, \quad (3.7)$$

### 3. Fluid Dynamical Theory

---

being  $\mathcal{L}$  the largest, characteristic system scale.

#### Total Energy Conservation

The total energy of an isolated system can be neither created nor destroyed; it can only change in form:

$$\partial_t E + \nabla \mathbf{u} \cdot (E + p) = \partial_{x_i} u_j \tau_{ij} + \nabla k_q \nabla T. \quad (3.8)$$

The change of energy  $E$  in time (per volume) is given by the energy flux  $\nabla \mathbf{u} E$ , work of pressure forces  $\nabla \mathbf{u} p$  or the terms on the right side of the equation. These are friction, and heat diffusion. The parameter  $k_q$  defines the heat conductivity (also known as thermal diffusion). The total energy  $E$  consists of an internal and kinetic contribution:

$$\frac{E}{\rho} = e + \frac{|\mathbf{u}|^2}{2}. \quad (3.9)$$

Insertion of Eq. 3.9 into Eq. 3.8 separately yields the conservation laws of internal and kinetic energy

$$\partial_t \rho e + \nabla \mathbf{u} \cdot (\rho e + p) - \mathbf{u} \cdot \nabla p = (\partial_{x_i} u_j - u_j \partial_{x_i}) \tau_{ij} + \nabla k_q \nabla T, \quad (3.10)$$

$$\partial_t \rho \frac{|\mathbf{u}|^2}{2} + \nabla \mathbf{u} \rho \frac{|\mathbf{u}|^2}{2} + \mathbf{u} \cdot \nabla p = u_i \partial_{x_j} \tau_{ji}, \quad (3.11)$$

respectively. This separation does not add new information, since the conservation of the kinetic energy (Eq. 3.11) can be deduced from the momentum equation, too (Eq. 3.2). The change of internal energy is similar to the kinetic one expressed by a flux, a pressure-work, and a friction term. Only the heat diffusion adds a fifth term. Comparison of the pressure and friction terms reveals identical terms with opposite

### 3.1 Compressible Navier-Stokes Equations

---

sign. This coupling is the conversion from kinetic to internal energy and vice versa. The internal energy can be considered to be chaotic, thermal energy, while the kinetic contribution is a macroscopic ordered motion of particles moving in the same direction.

These energy equations are incomplete: additional material equations for the internal energy  $e(\rho, \mathbf{u}, p)$  and temperature  $T(\rho, \mathbf{u}, p)$  are needed. One possibility to specify their explicit variable dependence is the assumption of an ideal gas (Sect. A.1). Insertion of the internal energy Eq. A.3 and the equation of state (Eq. A.1) into the internal energy Eq. 3.10 gives

$$\frac{1}{\gamma - 1} \partial_t p + \frac{\gamma}{\gamma - 1} \nabla \mathbf{u} p - \mathbf{u} \bullet \nabla p = (\partial_{x_i} u_j - u_j \partial_{x_i}) \tau_{ij} + \nabla k_{q0} \nabla \frac{p}{\rho} \quad (3.12)$$

with  $k_{q0} \equiv k_q/R_s$ , being  $R_s$  the specific gas constant (Eq. A.2).

#### General Navier-Stokes Equations

Strictly speaking, only the conservation of momentum is called Navier-Stokes equation (NSE). Nevertheless, in literature, this singular form is often utilized if the continuity and energy conservation are included as well. These are necessary to build a closed set of Navier-Stokes equations (NSEs):

$$\begin{aligned} \partial_t \rho + \nabla \rho \mathbf{u} &= 0, & (3.13) \\ \partial_t \rho u_i + \nabla \rho u_i \mathbf{u} + \partial_{x_i} p &= \partial_{x_j} \tau_{ji}, \\ \frac{1}{\gamma - 1} \partial_t p + \frac{\gamma}{\gamma - 1} \nabla \mathbf{u} p - \mathbf{u} \bullet \nabla p &= (\partial_{x_i} u_j - u_j \partial_{x_i}) \tau_{ij} + \nabla k_{q0} \nabla \frac{p}{\rho}. \end{aligned}$$

This form is also known as the Euler representation given in the absolute laboratory system. In contrast, the co-moving Lagrange representation

### 3. Fluid Dynamical Theory

---

is compactly written with the definition of the derivative

$$D_t = \partial_t + \mathbf{u} \bullet \nabla, \quad (3.14)$$

which leads to the alternative form:

$$\begin{aligned} D_t \rho + \rho \nabla \mathbf{u} &= 0, \\ D_t \mathbf{u} + \frac{1}{\rho} \nabla p &= \frac{1}{\rho} \partial_{x_j} \tau_{ji}, \\ D_t p + \gamma p \nabla \mathbf{u} &= (\gamma - 1)(\partial_{x_i} u_j - u_j \partial_{x_i}) \tau_{ij} + (\gamma - 1) \nabla k_{q0} \nabla \frac{p}{\rho}. \end{aligned} \quad (3.15)$$

#### Viscosity and Thermal Conduction

The transport coefficients (viscosity  $\nu$ , thermal conduction  $k_q$ ) are temperature sensitive: In this work, they are modeled by Sutherland's law

$$\frac{\mu}{\mu_{ref}} = \frac{T_{ref} + S}{T + S} \left( \frac{T}{T_{ref}} \right)^{3/2}, \quad (3.16)$$

being  $S = 110.4K$  Sutherland's temperature.

The ratio of the viscosity (momentum diffusivity) to the heat conduction (thermal diffusivity) is defined as the Prandtl number

$$Pr \equiv \frac{\mu C_p}{k_q}. \quad (3.17)$$

By assuming a constant Prandtl number  $Pr = 0.71$  and a constant heat capacity  $C_p = \frac{\gamma}{\gamma-1} R_s$  (Eq. A.12) of an ideal gas,  $k_q$  is given.

To simulate air near standard conditions ( $T_{ref} = 273K$ ,  $p_{ref} = 100kPa$ ) this work uses a specific gas constant of  $R_s = 287m^2K^{-1}s^{-2}$  and an adiabatic exponent  $\gamma = 1.4$  of a diatomic gas. Only for very high

temperatures regimes ( $T_{ref} > 1000\text{ K}$ ), the temperature dependence of  $R_s$  and  $\gamma$  need to be considered.

## 3.2 Turbulent Boundary Layer

Analytic solutions of the NSEs are rare. In case of a compressible TBL flow, Van **Driest** can derive a generally valid solution, which is introduced below. Later this solution is applied to validate the FP DNS (see Fig. 7.1) and to set proper inflow conditions in Sect. 5.3.

Typically, a boundary layer is subdivided into a lower inner layer at the wall, where viscous molecular shear dominates and an upper outer layer, where turbulent eddy shear dominates.

For a universal representation, the inner variables are rescaled by their viscous lengthscale

$$\delta_\nu \equiv \frac{\nu}{u_\tau} \tag{3.18}$$

and by their wall friction velocity

$$u_\tau \equiv \sqrt{\frac{\tau_w}{\rho_w}}, \tag{3.19}$$

where  $\tau_w$  is the wall shear stress (cf. Eq. 3.5)

$$\tau_w \equiv \rho_w \nu \frac{\partial}{\partial y} \langle u_x \rangle |_{y=y_w} = \rho_w u_\tau^2. \tag{3.20}$$

Often the wall shear stress is nondimensionalized as a so-called skin friction coefficient

$$C_f \equiv \frac{\tau_w}{\rho_w u_0^2 / 2}. \tag{3.21}$$

### 3. Fluid Dynamical Theory

---

Directly at the wall, the undermost velocity of the inner sub-layer scales like

$$\langle u \rangle^+ \equiv \frac{\langle u \rangle}{u_\tau} = y^+ \equiv \frac{y}{\delta_\nu}. \quad (3.22)$$

The outer variables are rescaled by the boundary layer thickness  $\delta_{99}$  and by the free stream velocity  $u_0$ . The boundary layer thickness  $\delta_{99}$  is defined by

$$u(y = \delta_{99}) = 0.99 u_0. \quad (3.23)$$

From most turbulence models it is known that an overlap region exists, where the small turbulent eddies smoothly merge into the viscous regime. The existence of this universal transition regime can be exploited to introduce an artificially increased viscosity  $\mu_{tot} = \mu_t + \mu$ , which incorporates not only molecular  $\mu$  forces but turbulent viscosity  $\mu_t$ , too (Boussinesq approximation). In this way, the smallest eddies do not need to be resolved numerically anymore but directly decay into heat.

An essential concept by Prandtl is to model the turbulent viscosity  $\mu_t$  of boundary layers by a characteristic **Mixing-Length**  $l$  and a velocity gradient (White, 2006):

$$\nu_t = l^2 \left| \frac{\partial \langle u_x \rangle}{\partial y} \right|. \quad (3.24)$$

In the overlap layer between the inner and outer boundary layer, the universal Mixing-Length is estimated by Prandtl as  $l = \kappa y$ . Combination of Eq. 3.20 and Eq. 3.24 with this mixing length and  $\nu \rightarrow \nu_t$  gives  $\kappa y d \langle u \rangle = u_\tau dy$ . Integration in terms of the inner variables  $y^+ = y/\delta_\nu$  results in the well-established **Log-Law** of the

incompressible overlap layer:

$$\langle u \rangle_{inc}^+ = \frac{\langle u \rangle}{u_\tau} = \frac{1}{\kappa_{inc}} \ln y^+ + B_{inc}. \quad (3.25)$$

The experimentally fitted constants for an incompressible TBL flow are  $\kappa_{inc} = 0.41$  and  $B_{inc} = 5.1$  (White, 2006). A generalized version of the incompressible Log-Law which describes the inner, overlap and outer layer all together can be combined (Guarini et al., 2000) with Reichardt's (1951) inner layer and Coles's (1956) outer layer wake:

$$\begin{aligned} \langle u \rangle_{inc}^+ &= \left( B_{inc} - \frac{\ln(\kappa_{inc})}{\kappa_{inc}} \right) \left( 1 - e^{-y^+/\eta_1} - \frac{y^+}{\eta_1} e^{-by^+} \right) \\ &+ \frac{1}{\kappa_{inc}} \ln(1 + \kappa_{inc} y^+) \\ &+ \frac{2\Pi}{\kappa_{inc}} \sin\left(\frac{\pi}{2} \frac{y}{\delta_{99}}\right)^2, \end{aligned} \quad (3.26)$$

being  $\eta_1 = 11$  and  $b = 0.33$ . Cole's wake parameter  $\Pi$  must be set such that  $\langle u \rangle_{inc}^+(y = \delta_{99}) = u_0/u_\tau$ .

Van Driest states a variable transformation, to relate the incompressible solution  $\langle u \rangle_{inc}$  with the compressible solution  $\langle u \rangle$  (White, 2006, Sect. 7-7.1):

$$\begin{aligned} \langle u \rangle_{inc} &= \frac{u_0}{a} (\arcsin A(u) + \arcsin B), \text{ being} \\ A(u) &= \frac{2a^2 \langle u \rangle}{Q u_0} - B, \quad B = \frac{b}{Q}, \quad Q = \sqrt{4a^2 + b^2}, \\ a &= \sqrt{\frac{\gamma - 1}{2} M_0^2 \frac{T_0}{T_w}}, \quad b = \frac{T_{aw}}{T_w} - 1. \end{aligned} \quad (3.27)$$

The required compressible velocity profile results by equating Eq. 3.26 and Eq. 3.27 and solving for  $\langle u \rangle$ . All free stream properties are defined

### 3. Fluid Dynamical Theory

---

with a “0” index, again. In the present case of a wall without heat flux, the temperature at the wall  $T_w$  is equal to the adiabatic wall temperature  $T_{aw}$ . Such  $B$  and  $b$  are zero.

To calculate the compressible density corresponding to the compressible velocity  $\langle u \rangle$  Van **Driest** adopts the turbulent Crocco-Busemann-relation (White, 2006, Sect. 7-6.2):

$$\frac{\rho_w}{\langle \rho \rangle} = \frac{\langle T \rangle}{T_w} = 1 + \left( \frac{T_{aw}}{T_w} - 1 \right) \frac{\langle u \rangle}{u_0} - r_{ec} \frac{\gamma - 1}{2} M_0^2 \frac{T_0}{T_w} \left( \frac{\langle u \rangle}{u_0} \right)^2, \quad (3.28)$$

being  $r_{ec} = Pr^{1/3}$  the recovery factor. Solving Eq. 3.28 at  $y = \delta_{99}$  for  $\langle T \rangle = T_0$  and  $\langle u \rangle = u_0$  reveals the ratio between the adiabatic wall temperature and the free stream temperature

$$\frac{T_{aw}}{T_0} = 1 + r_{ec} \frac{\gamma - 1}{2} M_0^2, \quad (3.29)$$

which is needed to calculate  $a$  of Eq. 3.27.

Besides the Van **Driest** transformation between the compressible and incompressible boundary layer profiles, Van **Driest** specifies a second transformation, which relates the compressible and incompressible skin friction coefficient (White, 2006, Sect. 7-8.1):

$$C_f = C_{f_{inc}} \frac{(\arcsin A(\langle u \rangle = u_0) + \arcsin B)^2}{T_{aw}/T_0 - 1}. \quad (3.30)$$

Eq. 3.27 gives  $A$  and  $B$ , already. The incompressible skin friction coefficient is exhaustively investigated in the literature. For Reynolds numbers  $Re_\theta \in [10^2, 10^5]$  Hopkins and Inouye (1971) state the universal fit

$$C_{f_{inc}}^{-1} = 17.08 \log^2 Re_\theta + 25.11 \log Re_\theta + 6.012. \quad (3.31)$$

Here, the Reynolds number  $Re_\theta = u_0\theta/\nu$  is related to the momentum thickness

$$\theta = \int_0^\infty \frac{\rho(y)}{\rho_0} \frac{u(y)}{u_0} \left(1 - \frac{u(y)}{u_0}\right) dy. \quad (3.32)$$

By now all equations can be connected in a closed form to calculate the compressible turbulent boundary layer solution. A solution is given by the iterative pseudocode [3.1](#).

### 3. Fluid Dynamical Theory

---

**Pseudocode 3.1:** Van Driest Solution of a compressible TBL.

**Input**  $Re_{\delta_{99}}$ ,  $M_0$ ,  $T_0$ ,  $T_{aw}/T_w$ ,  $Pr$  and  $\gamma$   
 $\delta_{99}$ ,  $u_0$ , and  $\rho_0$  can be formally set as one and dimensionalized later.

Calculate  $\nu = u_0 \delta_{99} / Re_{\delta_{99}}$ .

Guess the turbulent skin friction coefficient  $C_f$ .

**Repeat**

1. Determination of the wall friction velocity  $u_\tau$  based on the compressible skin friction  $C_f$  with Eq. 3.21.
2. Calculation of the viscous length scale  $\delta_\nu(u_\tau)$  with Eq. 3.18.
3. The solution of the incompressible velocity profile  $\langle u \rangle_{inc}$  provided by Eq. 3.26.
4. Application of Eq. 3.27 to transform the incompressible velocity profile  $\langle u \rangle_{inc}(y)$  to the compressible velocity profile  $\langle u \rangle(y)$ .
5. Derivation of the density profile  $\langle \rho \rangle(y)$  corresponding to the compressible  $\langle u \rangle(y)$  using Eq. 3.28.
6. Integration of the momentum thickness  $\theta$  according to Eq. 3.32.
7. Evaluation of the incompressible skin friction coefficient  $C_{f_{inc}}(\theta)$  (Eq. 3.31).
8. Second Van Driest transformation (Eq. 3.30) to convert the incompressible skin friction coefficient to the compressible  $C_f$ .

**Until** convergence of  $C_f$

**Output**  $\rho(y)$ ,  $u(y)$ ,  $u_\tau$  and  $C_f$

# Acoustical Theory and Modeling

# 4

This chapter generally formulates a model of a Helmholtz resonator, comprising the following steps: First, Sect. 4.1 presents the underlying linear acoustic theory. Second, Sect. 4.2 introduces all the single acoustic elements, which connected yield the entire model. The underlying basic theory of these elements is critical since the assumptions and simplifications made explain the validity range of the final model (such as linear one-dimensional wave propagation, frequencies below transverse cavity modes, a low Mach number and a thin vortex sheet). For a better understanding and flexible use of the model, flow related and purely acoustical effects are separated from each other by different acoustic elements. Purely acoustical elements (no-flow) are adapted from Golliard (2002). Third, Sects. 4.2.1 and 4.2.2 state a generic model of a Helmholtz resonator and its application possibilities, respectively. Fourth, Sect. 4.3 finally describes the new Helmholtz Resonator model, which is studied in detail in this work. Fifth, Sect. 4.4 specifies in more detail the flow related element, which is newly derived from Howe's conductivity model of an opening with a shear layer. Here, the significant parameters appear, which are analyzed and redefined throughout this work.

### 4.1 Acoustic Wave Equation

This section introduces the linear theory of sound waves.

Sound properties are:

1. a longitudinal wave propagation,
2. a characteristic propagation speed,
3. small density and pressure fluctuations around a relatively large steady component,
4. negligible friction and thermal dispersion (valid for dry, ideal gases at standard conditions),
5. quasi-isentropic (reversible and adiabatic, orders of magnitude faster than heat conduction).

In the following, these definitions are exploited to derive the linear acoustic wave equation starting from the NSEs Eq. 3.12. First, the viscosity  $\nu$  and the conductivity  $k_{q0}$  is set to zero (Euler equations). Second, the remaining terms are linearized by separating the steady component and the fluctuation:

$$\begin{aligned}\rho &= \rho_0 + \rho', \\ \mathbf{u} &= \mathbf{u}_0 + \mathbf{u}', \\ p &= p_0 + p'.\end{aligned}\tag{4.1}$$

Following [Ehrenfried \(2004\)](#), assuming  $\mathbf{u}_0 = 0$  (stationary frame) and  $\rho_0 \gg \rho'$ ,  $p_0 \gg p'$  this leads to the mass and momentum equations

$$\begin{aligned} \frac{\partial \rho'}{\partial t} + \rho_0 \nabla \cdot \mathbf{u}' &= 0, \\ \rho_0 \frac{\partial v'}{\partial t} + \nabla p' &= 0. \end{aligned} \quad (4.2)$$

Any pressure-density relation  $p(\rho)$  can be used to close this set of equations. A Taylor expansion of an arbitrary pressure-density relation up to linear order is

$$p(\rho) = p_0 + (\rho - \rho_0) \left. \frac{\partial p}{\partial \rho} \right|_{\rho_0}, \quad \Rightarrow \quad \frac{p'}{\rho'} = \left. \frac{\partial p}{\partial \rho} \right|_{\rho_0}. \quad (4.3)$$

Thereby, the derivation term  $\partial p / \partial \rho$  at constant entropy  $S$  is defined as the **speed of sound**:

$$c^2 \equiv \left. \frac{\partial p}{\partial \rho} \right|_S. \quad (4.4)$$

In case of an ideal gas, the isentropic density pressure relation is known (Eq. [A.19](#)). This implies

$$c_0^2 = \gamma \frac{p_0}{\rho_0} = \gamma R_s T_0 = (\gamma - 1) C_p T_0. \quad (4.5)$$

Now the wave equation of the sound pressure follows by a combination of Eq. [4.2](#) and Eq. [4.5](#) ([Ehrenfried, 2004](#)):

$$c_0^{-2} \frac{\partial^2 p'}{\partial t^2} - \Delta p' = 0. \quad (4.6)$$

## 4. Acoustical Theory and Modeling

---

A fundamental, harmonic solution of Eq. 4.6 in one dimension is

$$p' = \mathbb{R} \left[ A e^{i(k_x x - \omega t)} + B e^{i(k_x x + \omega t)} \right]. \quad (4.7)$$

One sinusoidal wave is moving in the positive  $x$ -direction with the scalar amplitude  $A$ ; another wave is propagating in the opposite direction with the amplitude  $B$ . Fig. 4.1 illustrates individual fluid particles in case of a single wave ( $B = 0$ ).



Figure 4.1: Fluid particle representation of a plane sound wave.

## 4.2 Lumped-Element Method

Stein and Sesterhenn (2019a) partially published this section.

In the following, the basic model structure of a duct system with a TBL flow and a flush-mounted cavity is derived. To this end, the Lumped-Element Method (Munjaj, 1987) is elaborated (also known as Transfer Matrix Method or Four-Pole Method). One-dimensional propagation of acoustic waves, in the present case in the  $y$ -direction, is described in the frequency domain. The idea is to decompose the propagation of waves in a duct system into single acoustic elements. Doing so, independent parts of the model separately describe the purely acoustical wave propagation inside the Helmholtz resonator, the shear layer of the neck opening, and the incoming TBL.

This method brings the advantage of differentiating and investigating physical effects independently. An individual element can be easily

adapted to the specific application. The disadvantage is the one-dimensionality and the neglect of nonlinearities. The conditions, where nonlinear resonances arise, are specified later (see Sect. 8.2). For silencing purposes, the Helmholtz base frequency, which lies below the cutoff frequency of higher transverse modes, is of most interest. Hence, linear, plane waves with a wavevector  $k W_{\max} \ll 1$  (compactness) are assumed, where  $W_{\max}$  is the maximal duct width. This means that in the model transverse cavity modes are not contained, but longitudinal cavity modes.

In general, the transfer matrix  $M \in \mathbb{C}^{2 \times 2}$  of a single acoustic element, which relates the acoustic pressure  $p'$  and the acoustic volume flux

$$v' = S u' \tag{4.8}$$

with the cross-section surface  $S$  of a low  $y$ -position denoted by the subscript “ $-$ ” with a high  $y$ -position “ $+$ ” is

$$\begin{pmatrix} p'_- \\ v'_- \end{pmatrix} = M \begin{pmatrix} p'_+ \\ v'_+ \end{pmatrix}. \tag{4.9}$$

Below, the acoustic elements needed for the acoustic model are introduced one by one.

**The transfer matrix of a duct** with the length  $l = y_+ - y_-$  is

$$M_{duct} = \begin{pmatrix} \cos(kl) & i Y \sin(kl) \\ \frac{i}{Y} \sin(kl) & \cos(kl) \end{pmatrix}, \tag{4.10}$$

being  $Y = \rho c / S$  the characteristic impedance.

#### 4. Acoustical Theory and Modeling

---

The transfer matrix of a cross-section jump typically is given by a change in pressure only:

$$M_{jump} = \begin{pmatrix} 1 & Z_{jump} \\ 0 & 1 \end{pmatrix}. \quad (4.11)$$

Always, the complex-valued impedance  $Z = (r + ik\delta)Y$  can be decomposed into resistance  $r$  (sign dependent excitation or damping) and a reactance  $\delta$  (length correction). In the simplest case of a two-dimensional duct with the widths  $W_- > W_+$ , the resistance, and reactance are given by Morse and Feshbach (1953)

$$r_{jump} = 0, \quad \delta_{jump} = W_+ \ln \frac{2W_-}{\pi W_+}. \quad (4.12)$$

The transfer matrix  $M_{rad}$  of an infinite flange, i.e., an open pipe end radiating into a free half space ( $S_+ = \infty$ ), can be expressed analogously to Eq. 4.11 (Morse and Ingard, 1968):

$$M_{rad} = \begin{pmatrix} 1 & Z_{rad} \\ 0 & 1 \end{pmatrix}. \quad (4.13)$$

This time both resistance and reactance of the decomposed impedance  $Z_{rad}$  are non zero because the damping effect of the rapidly decaying near field is included:

$$r_{rad} = \frac{S_{pipe} k^2}{2\pi}, \quad \delta_{rad} = \frac{8r_{pipe}}{3\pi}, \quad (4.14)$$

where  $r_{pipe}$  and  $S_{pipe}$  are the radius and the surface area of the pipe, respectively. Morse and Ingard (1968) claim that Eq. 4.14 is valid for a rectangular duct, too.

The transfer matrix of acoustic waves tunneling perpendicular through a vortex sheet of a neck opening is defined by Howe (1998) as  $i\omega\rho/K_R = (p'_+ - p'_-)/v'$ , which according to the author again can be rewritten together with  $v' = v'_+ = v'_-$  as an in-line element

$$M_R = \begin{pmatrix} 1 & Z_R \\ 0 & 1 \end{pmatrix}, \text{ with } Z_R = -ikY_{neck} \frac{S_{neck}}{K_R} = (r_R + ik\delta_R) Y_{neck},$$

$$\text{being } \delta_R = -\Re \left[ \frac{S_{neck}}{K_R} \right] \text{ and } r_R = k \Im \left[ \frac{S_{neck}}{K_R} \right]. \quad (4.15)$$

$K_R$  is the complex-valued Rayleigh conductivity of an opening inside an infinitely extended, thin wall. Sect. 4.4 elaborates details concerning  $K_R$ . (Such as, the vortex sheet is assumed to be infinitely thin and to be localized in the neck opening only. The vortices of the surrounding TBL are neglected.) Positive reactance  $r_R > 0$  implies acoustic damping, which is equivalent to  $\Im[K_R] < 0$ . Howe's  $K_R$  definition contains both the flow related effects of the vortex sheet as well as geometric effects of acoustic waves propagating through an opening.

Next, both effects are formally separated to maintain the adaptable modular design of the model. Later, in Sect. 4.4, the geometric no-flow subparts (originating from Howe's  $K_R$ ) are replaced to fit the present HR geometry better.

The transfer matrix  $M_{flow}$  of acoustical vortex sheet tunneling alone is isolated by subtraction of all zero-flow processes. Separation of  $Z_{flow} = Z_R - Z_{R_0}$  and  $1/K_{flow} = 1/K_R - 1/K_{R_0}$  inside

#### 4. Acoustical Theory and Modeling

---

Eq. 4.15 leads to

$$M_{flow} = \begin{pmatrix} 1 & Z_{flow} \\ 0 & 1 \end{pmatrix}, \text{ being } Y_{neck} = \rho c / S_{neck},$$

$$\delta_{flow} = \Re \left[ \frac{S_{neck}}{K_{R_0}} - \frac{S_{neck}}{K_R} \right], \quad r_{flow} = k \Im \left[ \frac{S_{neck}}{K_R} - \frac{S_{neck}}{K_{R_0}} \right]. \quad (4.16)$$

The geometry related, zero-flow impedance  $Z_{R_0}$  and conductivity  $K_{R_0}$  are denoted by a “0” index. This work focuses in particular on the interaction between acoustical and fluid-related effects contained in  $Z_{flow}$ . In Sect. 4.4, a more detailed discussion follows, in which  $K_R$  and  $K_{R_0}$  are derived, too.

**The transfer matrix of a generic neck opening in a thin wall** is set up by combining (“lumping”) multiple elements  $M_1 M_2 \dots$  as

$$M_{neck} = M_{jump} M_{flow} M_{rad} = \begin{pmatrix} 1 & Z_{neck} \\ 0 & 1 \end{pmatrix}, \quad (4.17)$$

being  $Z_{neck} = Z_1 + Z_1 + \dots$ . In this way, instead of an opening inside an infinitely extended wall ( $Z_{neck} = Z_R$ ), one can deal with more general cases. In the present case, the neck opening inside a wall between a finite duct below and an infinite space above (including radiation decay) is modeled by

$$Z_{neck} = Z_{jump} + Z_{flow} + Z_{rad}. \quad (4.18)$$

All these utilized impedances were introduced before (Eqs. 4.12, 4.16 and 4.14). The complex-valued neck impedance  $Z_{neck} = (r_{neck} +$

$ik\delta_{neck})Y_{neck}$  consists of the reactance  $\delta_{neck} = \delta_{jump} + \delta_{flow} + \delta_{rad}$  and the resistance  $r_{neck} = r_{jump} + r_{flow} + r_{rad}$ .

### 4.2.1 Generic Helmholtz Resonator Model

The generic model of a Helmholtz resonator (see Fig. 4.2) is set-up by Howe (1998, Sec. 6.1.3) as well as Golliard (2002, Sec. 2.1.2) by one boundary condition and two lumped elements (from bottom to top): a closed end<sup>1</sup> (acoustically hard wall,  $v'_{bot} = 0$ ), a cavity duct element  $M_{duct}$  and a neck opening element  $M_{neck}$  accounting in particular for the vortex sheet tunneling of acoustic waves:

$$\begin{pmatrix} p'_{bot} \\ 0 \end{pmatrix} = M_{duct}M_{neck} \begin{pmatrix} p'_{top} \\ v'_{top} \end{pmatrix}. \quad (4.19)$$

$M_{duct}$  is given by Eq. 4.10.  $M_{neck}$  is defined according to Eq. 4.17 and Eq. 4.18. For a better overview, Fig. 4.2 depicts all model elements. Explicit multiplication of Eq. 4.19 from the left by  $M_{duct}^{-1}$  gives:

$$\begin{pmatrix} \cos(kl)p'_{bot} \\ -i \sin(kl)p'_{bot}/Y_{cavity} \end{pmatrix} = \begin{pmatrix} Z_{neck}v'_{top} + p'_{top} \\ v'_{top} \end{pmatrix}. \quad (4.20)$$

Due to the present case, the characteristic impedance of the duct is called in the following  $Y_{cavity} = \rho c/S_{cavity}$  with a constant cross-section  $S_{cavity} = L_{x-cavity}L_{z-cavity}$ . The length  $l$  of the duct becomes the cavity height  $L_{y-cavity}$ . In this model  $y$  is the only direction of acoustic wave propagation. Eq. 4.20 represents the generic model of a Helmholtz

---

<sup>1</sup>In some applications, foam instead of a hard wall terminates cavities to damp high frequencies. Here instead of  $v'_{bot} = 0$  also a foam specific wall impedance could be used. Acoustically hard walls are common for sensitive environments of high pressure or temperature.

## 4. Acoustical Theory and Modeling

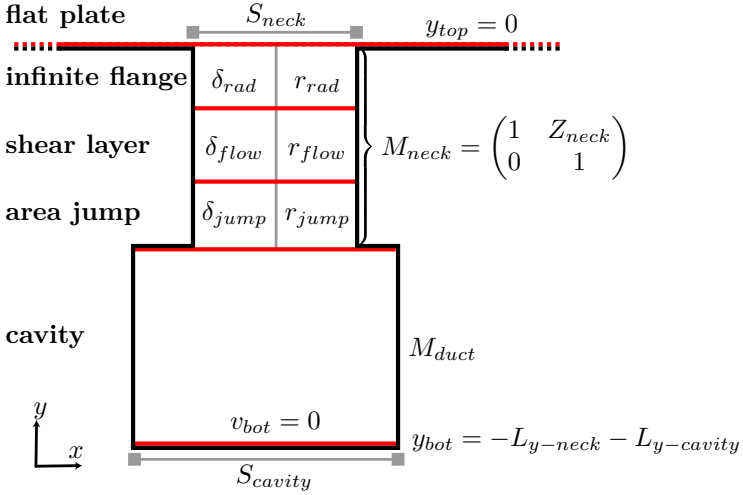


**Figure 4.2:** Generic structure of a Helmholtz resonator using the Lumped-Element Method. The red horizontal lines mark the start and end surfaces of the elements. All neck elements can be combined as  $M_{neck} = M_{jump}M_{flow}M_{rad}$ . The complex-valued neck impedance  $Z_{neck} = (r_{neck} + ik\delta_{neck})Y_{neck}$  is decomposed into its real part, the reactance  $\delta_{neck} = \delta_{jump} + \delta_{flow} + \delta_{rad}$  (length corrections) and its imaginary part, the resistance  $r_{neck} = r_{jump} + r_{flow} + r_{rad}$  (sign dependent excitation or damping).

resonator, used as the underlying framework to derive more specific models, after this.

### 4.2.2 Generic Helmholtz Resonator Model Applications

To illustrate the universality of the Helmholtz resonator model (Eq. 4.20) in the following a diverse set of applications is addressed, all starting from Eq. 4.20.

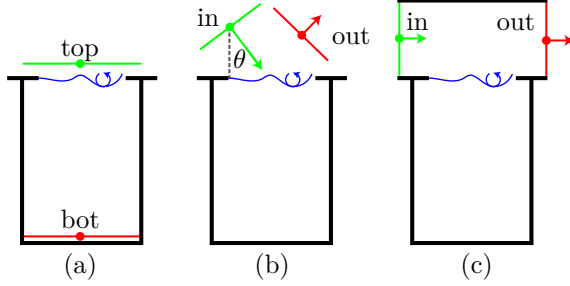


**Figure 4.3:** Possible applications of the generic model: (a) entering of acoustic waves inside a cavity, (b) reflection loss of a cavity-backed perforated screen, (c) transmission loss in a duct system with a cavity. All hard walls are colored black. The vortex sheet of the neck is blue. Input or source wave isolines are green, while output or resulting wave isolines are red. Arrows denote the part of a wave which is moving only in one direction. This work focuses mainly on example (a).

**Application example (a): The transmission of outer acoustic waves into the Helmholtz resonator** (see Fig. 4.3 (a)) results from solving Eq. 4.20 for  $p'_{top}/p'_{bot}$  and thereby eliminating  $v'_{top}$ :

$$\frac{p'_{top}}{p'_{bot}} = \cos(kl) + i \sin(kl) \frac{Z_{neck}}{Y_{cavity}}. \quad (4.21)$$

Taking the absolute value of each side of the Eq. 4.21 leads to the transmission coefficient  $T = |p'_{bot}/p'_{top}|^2$  (Golliard, 2002):

$$T^{-1} = \sin^2(kl) (\Lambda_\delta^2 + \Delta_r^2) \text{ being} \quad (4.22)$$

$$\Lambda_\delta = \cot(kl) - S_{ratio}(\delta_{jump} + \delta_{flow} + \delta_{rad})k \quad (4.23)$$

the effective length,

$$\Delta_r = S_{ratio}(r_{flow} + r_{rad}) \text{ the energy transfer,} \quad (4.24)$$

#### 4. Acoustical Theory and Modeling

---

$S_{ratio} = S_{cavity}/S_{neck}$  the cross-section surface ratio and  $l$  the cavity height.  $r_{jump}$  is set to zero according to Eq. 4.12.  $\Lambda_\delta$  can be related to the total effective length of the cavity including all length corrections (also known as phase shifts). Its zeros are the longitudinal angular  $y$ -wavenumbers  $k$  of the cavity: The first zero corresponds to the Helmholtz base frequency ( $\omega = ck$ ). The second zero is the largest  $y$ -wavelength fitting into the cavity and so on.  $\Delta_r$  can be interpreted as amplitude modulation of acoustic waves (resistance). Depending on the sign of  $r_{flow} + r_{rad}$ , either acoustic energy is converted into flow vorticity at the neck or vice versa.

The modulation of outer acoustic waves (example (b) and (c)) due to a Helmholtz resonator is imposed by the impedance  $Z_{top} = p'_{top}/v'_{top}$  which is derived by eliminating  $p'_{bot}$  of Eq. 4.20:

$$Z_{top} = \frac{-i\omega\rho}{K_{top}} = iY_{cavity} \cot(kl) - Z_{neck}. \quad (4.25)$$

**Application example (b): In case a Helmholtz resonator is mounted in a perforated screen** (see Fig. 4.3 (b)) the reflection loss depending on the angle  $\theta$  of incident sound is according to Howe (1998, Sec. 5.3.2)

$$L_R = 20 \log_{10} \frac{|p'_{in}|}{|p'_{out}|} \quad \text{with} \quad \frac{p'_{out}}{p'_{in}} = -\frac{k \cos(\theta)}{k \cos(\theta) + i2K_{top}}, \quad (4.26)$$

being  $K_{top}$  defined by Eq. 4.25.

**Application example (c): If a resonator is mounted inside a duct system** (see Fig. 4.3 (c)) with a constant surface size  $S_{cavity}$

the resulting transmission loss is (Ehrenfried, 2004, Sec. 12.3)

$$L_T = 20 \log_{10} \frac{|p'_{in}|}{|p'_{out}|} = -20 \log_{10} |1 + R| \quad (4.27)$$

with the complex-valued reflection coefficient

$$R = \frac{-Y_{cavity}}{2Z_{top} + Y_{cavity}},$$

being  $Z_{top}$  also defined by Eq. 4.25.

In all these example applications, the crucial task lies in the determination of the neck impedance  $Z_{neck} = Z_{jump} + Z_{flow} + Z_{rad}$ . Eq. 4.12 ( $Z_{jump}$ ) and Eq. 4.14 ( $Z_{rad}$ ) fully describe purely geometry related effects of the acoustic wave propagation (with zero-flow). In contrast, the description of the fluid-acoustic interaction is missing. Eq. 4.16 only formally rewrites  $Z_{flow}$  in terms of the unknown Rayleigh conductivity  $K_R$ . The key point of this thesis is to derive  $Z_{flow}$ , resolving all missing dependencies.

## 4.3 The New Helmholtz Resonator Model

As a proof of concept, this work focuses on the application example (a), see Fig. 4.3 (a): The transmission of external acoustic waves into the Helmholtz resonator. The generic transmission function  $T$  is composed of Eqs. 4.22 - 4.24. In case (a), a numerical and experimental reference database is available (Sect. 2.2). No extra acoustic source is necessary since the turbulent boundary layer (TBL) of the grazing flat plate flow causes a broadband excitation already. Hence, the power spectral density of the pressure fluctuations at the top (green line of Fig. 4.3 or green arrow of Fig. 4.4) is  $\Phi_{top} = \Phi_{TBL}$ . The combination

## 4. Acoustical Theory and Modeling

---

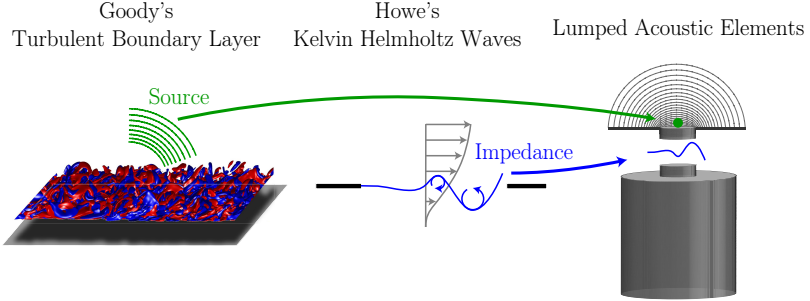


**Figure 4.4:** Overview of the new HR model (Eq. 4.28). Utilizing the Lumped-Element Method (Sect. 4.2), the main components are: Goody’s spectra model of wall-pressure fluctuations  $\Phi_{TBL}$  (Sect. 7.3.2), which serve as input (green arrow), and Howe’s impedance model  $Z_{neck}$  (Sect. 4.4) to describe acoustic waves passing through a shear layer (colored blue).

(multiplication) of the generic transmission function  $T$  and the source term  $\Phi_{TBL}$  represents the new Helmholtz resonator model (HR model)

$$\Phi_{bot}(\omega) = T(Z_{neck}, \omega) \Phi_{TBL}(\omega). \quad (4.28)$$

Thereby, the power spectral density  $\Phi$  is directly related to the SPL (Eq. 7.3).  $\omega$  is the angular frequency of a linear acoustic wave. The transmission function  $T(Z_{neck})$  includes effects of the neck shear layer. The source term  $\Phi_{TBL}$  independently describes the incoming TBL. Howe reasons that this separate treatment of a localized neck shear layer and an overlying TBL is allowed for low Mach number flows ( $M_0 < 0.2$ ).

In the further course, Howe’s complex-valued neck impedance  $Z_{neck}$  is discussed (see Sect. 4.4); as well as Goody’s model of the pressure fluctuations  $\Phi_{TBL}$  (see Sect. 7.3.2). Fig. 4.4 sketches an overview of all these HR model components. The major novelty of the following

model derivation lies in the treatment of the parameters, which are governing  $Z_{neck}$ . In the next Sect. 4.4 these parameters are introduced. After a thorough analysis of the characteristic flow features, Sect. 7.4 then proposes a new method to determine the parameters in case of a realistic turbulent flow (three-dimensionally distributed).

### 4.4 Howe's Conductivity Model of an Opening under Grazing Flow

**Stein and Sesterhenn (2018)** partially published the theory presented in this section.

This section elaborates on the central impedance element  $Z_{neck}$  of the new Helmholtz resonator model (Eq. 4.28): the incorporation of the interaction between the shearing flow around the cavity opening and the acoustic waves resonating inside the cavity.

In the present HR case, the incoming boundary layer thickness is smaller than the streamwise neck length. This implies the existence of a KH instability. The coupling of the resulting KH waves at the neck zone and the acoustic waves resonating inside the cavity is the crucial part of the model. To incorporate this complex coupling into the model, **Howe's** Rayleigh conductivity of an aperture in grazing flow is utilized.

In **Howe (1998, Sec. 5.3.1)**, the tunneling of acoustic waves perpendicular through an opening with a vortex sheet caused by a grazing, low Mach number flow is described. In contrast to the present DNS case with an incoming TBL, **Howe** assumes a steady, irrotational mean background flow. All viscous or rotational effects are restricted to an infinitely thin vortex sheet covering the opening inside an infinite extended and infinite thin wall without a cavity below. **Howe** models

#### 4. Acoustical Theory and Modeling

---

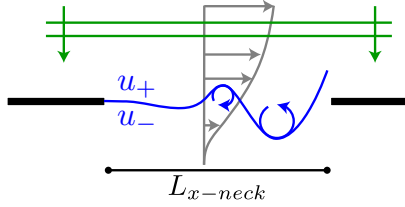


**Figure 4.5:** Exemplary sketch of the displacement of a vortex sheet modeled by Howe (Eq. 4.33) for an opening in grazing, two-sided low Mach number flow. The oscillating vortex sheet of the opening shear layer (between the black walls) is painted blue, and the underlying mean velocity profile is gray. From above, plane acoustic waves are penetrating (colored green). Most delicate,  $u_{\pm}$  denote the characteristic mean flow parameters above and below the vortex sheet, which are governing the KH waves.

the  $y$ -displacement (perturbation) of this vortex sheet in the framework of linear perturbation theory. Here the motion of the vortex sheet is only dependent on: the  $xz$ -shape of the neck (not dependent on  $y$ ), the acoustic volume flux  $v = v'_+ = v'_-$  through the neck, the acoustic pressures  $p_{\pm}$ , and two characteristic mean velocities  $u_{\pm}$  above and below the thin vortex sheet. Fig. 4.5 shows a qualitative sketch of a displaced shear layer.

Starting from the definition of the Rayleigh conductivity  $K_R$  (inverse impedance) of an opening, Howe rewrites the integral flux  $v = \int u_y(x, z) dx dz$  as local  $y$ -displacement  $\zeta(x, z)$  of the vortex sheet as follows:

$$\frac{K_R}{i\omega\rho} \equiv \frac{v}{p'_+ - p'_-} = \frac{\pi L_{x-neck}}{2} \int_S \zeta(x, z) dx dz. \quad (4.29)$$

The vortex sheet displacement  $\zeta(x, z)$  can be numerically determined (as realized in Sect. 8.4.3) for arbitrary neck shapes by solving the

conditional equation

$$\int_S \frac{\zeta(\mathbf{x}, \tilde{\mathbf{x}})}{\mathbf{x} - \tilde{\mathbf{x}}} d\tilde{\mathbf{x}} + \lambda_1(z)e^{i\sigma_1 x} + \lambda_2(z)e^{i\sigma_2 x} = 1 \quad (4.30)$$

for all locations  $\mathbf{x} = (x, z)^T \in S_{neck}$  of the opening surface by centroid collocation (Grace et al., 1998).  $\sigma_{1,2}$  are non-dimensional KH wavenumbers dependent on the Strouhal number  $St_{neck}$  of the vortex sheet:

$$\sigma_{1,2} = \pi St_{neck} \frac{1 \pm i}{1 \pm i\beta}, \quad St_{neck} = \frac{fL_{x-neck}}{u_+}, \quad \beta = \frac{u_-}{u_+}. \quad (4.31)$$

The classical phase velocity of a shear layer can be obtained with Howe's KH wavenumber definition

$$u_{ph1,2} = \frac{\omega}{\sigma_{1,2}} \frac{L_{x-neck}}{2} = \frac{u_+ + u_-}{2} \mp i \frac{u_+ - u_-}{2}, \quad (4.32)$$

too. The amplitudes  $\lambda_{1,2}$  of the KH waves  $e^{i\sigma_{1,2}x}$  in Eq. 4.30 are defined by imposing the Kutta condition  $\zeta = 0$  at the leading edge of the neck. In case of simple geometries like a square neck with  $L_{z-neck} \gg L_{x-neck}$  like in the present case (cf. Fig. 2.1), Eq. 4.30 can be analytically solved (Howe, 1981a):

$$\begin{aligned} K_R &= \frac{\pi}{2} L_{z-neck} / \{\mathcal{F}(\sigma_1, \sigma_2) + \Psi\}, \text{ being} & (4.33) \\ \mathcal{F}(\sigma_1, \sigma_2) &= \frac{J_0(\sigma_1)f_1(\sigma_2) - J_0(\sigma_2)f_1(\sigma_1)}{f_0(\sigma_2)f_1(\sigma_1) - f_0(\sigma_1)f_1(\sigma_2)}, \\ \Psi &= \ln(2) - \frac{\pi}{2}(a_- + a_+) \end{aligned}$$

with the shorthands  $f_1(\sigma) = \sigma\{J_0(\sigma) - 2f_0(\sigma)\}$  and  $f_0(\sigma) = i\sigma\{J_0(\sigma) - iJ_1(\sigma)\}$ , where  $J_{0,1}$  are Bessel functions.  $a_{\pm} = \ln(eL_{x-neck}/4L_{z-neck})/\pi$  are upper and lower cross-sectional jump

#### 4. Acoustical Theory and Modeling

---

corrections from an opening inside an infinitely extended wall comparable to  $\delta_{jump}$  and  $\delta_{rad}$  (Eq. 4.12 and Eq. 4.14). The choice of the characteristic mean velocity  $u_{\pm}$  is crucial, but unclear defined so far. Therefore, Sect. 7.4 proposes a new method.

At this point, note that  $u_{\pm}$  are mean flow values. KH instability waves exist on this mean flow, from which they extract their energy. In case of a balanced two-sided flow with  $\beta = u_-/u_+ = 1$  a real-valued KH wavenumber scaling with  $St_{neck}(u_+)$  results. The corresponding phase speed (Eq. 4.32) of the instability waves is the mean of  $u_+$  and  $u_-$  (also real-valued). Only in case  $\beta \neq 1$  the wavenumber becomes complex-valued, i.e., the amplitudes of the KH waves  $e^{i\sigma x}$  are modified.

With  $K_R$  of Eq. 4.33 the neck impedance  $Z_R$  of Eq. 4.15 is exactly specified. To deal with geometric and fluid-related effects independently (see Eq. 4.16),  $K_R$  is separated now into  $K_{R_0}$  and  $K_{flow}$ , respectively, such that a more general neck impedance  $Z_{neck}$  can be set up following Eq. 4.18.

In the limit of zero-flow, the Strouhal number converges to infinity and the function  $\mathcal{F}$  of Eq. 4.33 converges to:  $\mathcal{F}_0 = -2$ . The no-flow impedance related to Eq. 4.16 is  $Z_{R_0} = -ikY_{neck}S_{neck}/K_{R_0}$ . The no-flow conductivity follows from Eq. 4.33 as  $K_{R_0} = 0.5\pi L_{z-neck}/\{\mathcal{F}_0 + \Psi\}$ . Since  $\mathcal{F}_0$  and  $K_{R_0}$  are real-valued, the no-flow impedance holds only the length correction

$$\begin{aligned} \delta_0 &= \Re \left[ \frac{S}{K_{R_0}} \right] \\ &= \frac{L_{z-neck}}{\pi} \left\{ 2\mathcal{F}_0 + \ln \left( \frac{8L_{z-neck}}{eL_{x-neck}} \right) + \ln \left( \frac{8L_{z-neck}}{eL_{x-neck}} \right) \right\}. \end{aligned} \quad (4.34)$$

Without flow, there is no energy exchange of the acoustics with the vortex sheet:  $r_0 = k \mathbb{I}[S/K_{R_0}] = 0$ . Since in the present case (cf. Sect. 2.2) the lower side of the neck is flanged to a finite cavity (instead

#### 4.4 Howe's Conductivity Model of an Opening

---

of Howe's infinitely extended wall),  $\delta_{jump}$  of Eq. 4.12 replaces the first two terms inside the curly brackets of Eq. 4.34:

$$\begin{aligned}\delta_0 &= \delta_{jump} + \delta_{rad} \\ &= L_{x-neck} \ln \frac{2L_{x-cavity}}{\pi L_{x-neck}} + \frac{L_{x-neck}}{\pi} \ln \left( \frac{8L_{z-neck}}{eL_{x-neck}} \right).\end{aligned}\quad (4.35)$$

This imaginary-valued, no-flow impedance ( $\delta$ -terms only), still differs from the complex valued and wavevector dependent impedance  $Z_{rad}$  of an open pipe termination Eq. 4.14, mainly because radiation effects are not included (besides geometric reasons). To include radiation effects  $\delta_{rad}$  of Eq. 4.35 is combined with  $r_{rad}$  of Eq. 4.14. Morse and Ingard (1968) show the similarity of the rectangular and circular radiation resistance, hence in Eq. 4.14  $S_{pipe} = S_{neck}$  is inserted. This combination of no-flow impedance terms originates from Golliard (2002). Employing an experimental Kundt's tube-like setup, Golliard (2002, Sect. 4.3.3) shows a qualitative agreement of the measured no-flow impedance with  $\delta_0 = \delta_{jump} + \delta_{rad}$  of Eq. 4.35 and  $r_0 = r_{rad}$  of Eq. 4.14.

Subtraction of all zero-flow processes isolates the impedance of the vortex sheet tunneling process itself. Separation of  $Z_{flow} = Z_R - Z_{R_0}$  cancels out  $\Psi$  of Eq. 4.33 and leads to an updated, specific form of Eq. 4.16:

$$\begin{aligned}r_{flow} &= k \mathbb{I} \left[ \frac{S_{neck}}{K_R} \right] = \frac{2}{\pi} St_{neck} \frac{u_+}{c_0} \mathbb{I} [\mathcal{F}(\sigma_1, \sigma_2)], \\ \delta_{flow} &= \mathbb{R} \left[ \frac{S_{neck}}{K_{R_0}} - \frac{S_{neck}}{K_R} \right] = \frac{2}{\pi} L_{x-neck} \mathbb{R} [\mathcal{F}_0 - \mathcal{F}(\sigma_1, \sigma_2)],\end{aligned}\quad (4.36)$$

with  $\mathcal{F}_0 = -2$  (see above) and the Mach number  $u_+/c_0 = ku_+/\omega$ .

#### 4. Acoustical Theory and Modeling

---

By now all lumped impedance terms ( $r$ 's and  $\delta$ 's) of the Helmholtz resonator model (Eq. 4.28, more specifically Eqs. 4.22 - 4.24) are specified.

# Computational Fluid Dynamics

# 5

This chapter introduces the numerical method used to simulate the FP and the HR case. Here, the focus lies on the correct representation of the physical conservation laws (acoustics is a non-dissipative phenomenon, see Sect. 5.2) and on the numerical generation of realistic turbulence (Sect. 5.3).

## 5.1 Direct Numerical Simulation Method

Direct Numerical Simulation (DNS) means that all system scales are resolved by the mesh and time step of the simulation. No approximations of the spatial or temporal dynamics of a system are used (Large Eddy Simulation or Reynolds-Averaged NSEs), but the fundamental equations of motion are solved. In the case of fluid dynamics, these equations are the NSEs (see Sect. 3.1) The computational efforts needed to conduct a DNS of the NSEs is thereby related to the Reynolds number (Eq. 3.7), which is proportional to the quotient of the biggest  $\mathcal{L}$ , and smallest  $\eta$  system scales as discovered by Kolmogorov:  $\eta/\mathcal{L} = Re^{-\frac{3}{4}}$ . Such the DNS is the most exact representation but limited to low Reynolds numbers due to computational costs.

To represent the state variables of the NSEs on a discrete mesh and to calculate their temporal evolution the Finite Differences Method (FDM) is employed. Appx. B gives a brief introduction of the FDM.

## 5. Computational Fluid Dynamics

---

All simulations performed in this work were conducted with the solver “Navier-Stokes Fortran” of the CFD group<sup>1</sup> (not licensed). Since 2000 this Navier-Stokes solver is continuously developed and validated (Brouwer et al., 2014; Reiss, 2015; Sesterhenn, 2001).

Most recently, as part of this work (see Appx. D), the Navier-Stokes solver is extended for more complex geometries as in the present case (see the setup in Fig. 2.1), consisting of multiple, different sized blocks. Previously, the solver could only handle fluids moving in a single, box-like domain.

The three-dimensional compressible NSEs (Eq. 3.13) are solved in real space  $\boldsymbol{x}$  and time  $t$  using the FDM on a structured grid. To guarantee additional conservation properties, the NSEs are discretized in a skew-symmetric form, developed by Reiss (2015). This is needed to deal with shocks, or as in this case, with frictionless phenomena like acoustics. As discussed at the beginning of Sect. 4.1, sound can be defined by far-ranging, nearly undamped waves without any dispersion. Small artificial damping would already distort their characteristics.

The Finite Differences are calculated with explicit, central derivation schemes of 4<sup>th</sup> order (Lele, 1992). For time integration a classical low-storage Runge-Kutta Method of 4<sup>th</sup> order is applied.

---

<sup>1</sup>Numerical Fluid Dynamics group, Institute of Fluid Dynamics and Technical Acoustics, Technische Universität Berlin

## 5.2 Skew-Symmetric Compressible Navier-Stokes Equations

Commonly, Finite Volume Schemes are applied to inbuilt conservative features. The drawback of this approach is that only explicit quantities like mass, momentum and total energy are conserved naturally. Implicit quantities like the kinetic energy still suffer from artificial damping [Gordner \(2005\)](#). As a solution, [Bijl \(1999\)](#) and [Subbareddy and Candler \(2009\)](#) suggest adding a correction step after the evaluation of every time step. Only with this additional correction step Finite Volume Schemes indeed exhibit full conservation.

In this thesis, the NSEs are solved in a skew-symmetric form, which ensures full conservation properties (using a FDM discretization). Precisely speaking, not only the three classical variables mass, momentum and total energy need to be conserved, but also artificial, numerical damping of the kinetic energy and the internal energy must be prevented, individually.

To set up the skew-symmetric form, the momentum equation of the classical NSEs in divergence form (Eq. 3.13) is replaced with the momentum equation in kinetic energy form (Eq. 3.4):

$$\partial_t \rho + \nabla \rho \mathbf{u} = 0, \quad (5.1)$$

$$\frac{\rho \partial_t + \partial_t \rho}{2} u_i + \frac{\rho \mathbf{u} \bullet \nabla + \nabla \rho \mathbf{u}}{2} u_i = -\partial_{x_i} p + \partial_{x_j} \tau_{ji}, \quad (5.2)$$

$$\begin{aligned} \frac{1}{\gamma - 1} \partial_t p + \frac{\gamma}{\gamma - 1} \nabla \mathbf{u} p = \mathbf{u} \bullet \nabla p + (\partial_{x_i} u_j - u_j \partial_{x_i}) \tau_{ij} \\ + \nabla k_{q0} \nabla \frac{p}{\rho}. \end{aligned} \quad (5.3)$$

Again, every operator is considered to act on all multiplicative terms on his right side. The temporal differentiation and the convection term

## 5. Computational Fluid Dynamics

---

(both exhibit the mirrored form  $(\phi\partial + \partial\phi)$  of an operator  $\partial$  and a variable  $\phi$ ) express the skew-symmetric form of Eq. 5.2. For the sake of brevity and numerical efficiency, a further simplification of the time integration is introduced according to [Morinishi \(2010\)](#). Rewriting all  $\rho$  terms as  $\sqrt{\rho}$  reduces the computationally expensive doubled time integration of the momentum equation (5.2) to a single derivation. Inserting the relations

$$\partial_t \rho = 2\sqrt{\rho}\partial_t\sqrt{\rho} \quad \text{and} \quad \frac{\rho\partial_t + \partial_t\rho}{2}u_i = \sqrt{\rho}\partial_t\sqrt{\rho}u_i$$

into the skew-symmetric NSEs (Eq. 5.1 et seq.) leads to the more compact mass and momentum equation:

$$\sqrt{\rho}\partial_t\sqrt{\rho} + \frac{1}{2}\nabla(\sqrt{\rho})^2\mathbf{u} = 0, \quad (5.4)$$

$$\sqrt{\rho}\partial_t\sqrt{\rho}u_i + \frac{(\sqrt{\rho})^2\mathbf{u}\bullet\nabla + \nabla(\sqrt{\rho})^2\mathbf{u}}{2}u_i + \partial_{x_i}p = \partial_{x_j}\tau_{ji}. \quad (5.5)$$

In all the following simulations Eqs. 5.3 - 5.5 are solved using the FDM with a central symmetric differentiation scheme. Sect. B.2 sketches how to proof full conservation properties of the FDM discretization of Eqs. 5.3 - 5.5. Strictly speaking, conservation of the discretized NSEs requires using a central temporal differentiation scheme (implicit time integration). Having said this, there are still several advantages (see Sect. B.3) of the skew-symmetric NSEs, if explicit time integration schemes are applied in practice (like Runge-Kutta in the present work).

## 5.3 Direct Numerical Simulation Setup

This section explains the computational setup of the two cases studied. As introduced in Chap. 2, the auxiliary FP case deals with a turbulent flat plate flow, while the main HR case covers a turbulent flat plate flow with a rectangular cavity mounted underneath as depicted in Fig. 2.1.

To compare the FP case without a resonating cavity with the modified flow of the HR case, both of them are fed with identical turbulent inflow conditions. Utilizing the new multi-block feature developed in this work (see Appx. D), both cases are simulated in parallel. This parallel execution allows saving computational resources, as explained below.

First the implementation of the boundary and initial conditions is described; second, the mesh resolution is discussed.

### Boundary and Initial Conditions

Fig. 5.1 pictures the boundary conditions. In the following subsections they are explained, one by one:

#### Open Boundaries

The upper side of the TBL is unbounded both in the FP and in the HR case. In this potential-flow region, non-reflective boundary conditions using characteristics (see Sect. C.2) are very effective. As a reference for the incoming Riemann invariants, the values of the inner neighboring gridpoints are set (zero gradient).

#### Inlet

A well-established turbulence generation procedure for a flat plate inflow is the **Recycling-Rescaling method** (Pirozzoli and Bernardini,

## 5. Computational Fluid Dynamics

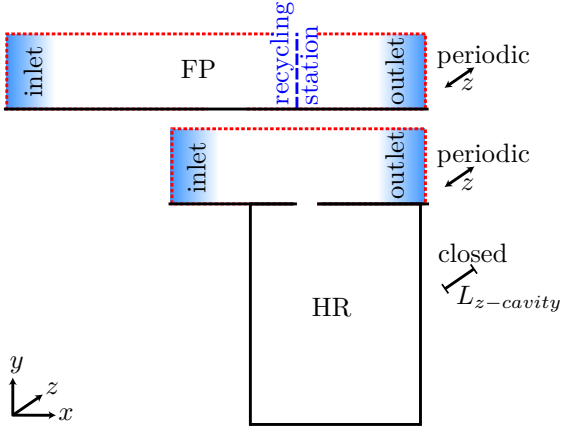


**Figure 5.1:** Side view of the two parallel executed simulations FP and HR. The figure represents non-reflecting boundary conditions as dashed red lines. Adiabatic no-slip walls are painted black. A blue gradient illustrates sponge layer regions. While the upper flat plate flow in both cases is periodically continued in the spanwise direction, the flush mounted cavity, and its neck opening is closed in spanwise direction by adiabatic no-slip walls.

2011). Starting from an already existing TBL, fluctuations are recorded at a wall-normal  $yz$ -plane of a downstream recycling station (see Fig. 5.1), rescaled according to self-similarity laws (Brouwer, 2016) and superimposed on the averaged mean inflow conditions of the  $yz$ -plane at the plate beginning. Hence, the turbulence information is recycled within the TBL. As averaged mean inflow condition the Van Driest Solution is applied, solved with pseudocode 3.1.

A truly turbulent inlet condition relies on a memory-less inflow of fluctuations. To assure statistically independence between the inlet and the recycling station, special care has to be taken. In the present DNS, a streamwise distance between the inlet and the recycling station of  $36\delta_{99FP-inlet}$  (200 mm) is used. Additionally, the  $yz$ -plane ( $z$ -periodic)

### 5.3 Direct Numerical Simulation Setup

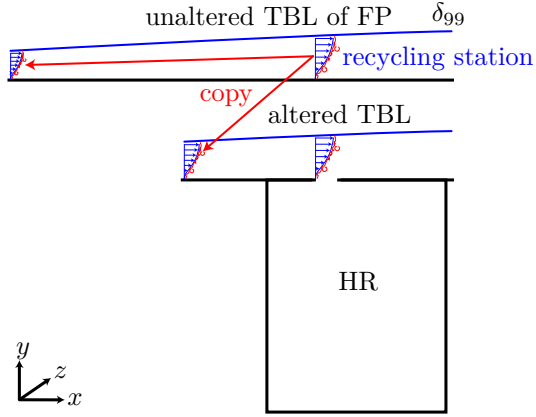


**Figure 5.2:** Side view of the FP and the HR simulation, executed in parallel. A blue line illustrates the growth of the TBL thickness  $\delta_{99}$ . MPI copied information within and between the simulations is denoted by red arrows.

is  $z$ -shifted by half the spanwise gridpoints, to double the effective distance of the inlet and the recycling station to  $72\delta_{99FP-inlet}$ .

To avoid a feedback loop, due to the presence of the HR, the Recycling-Rescaling method is only applied in the FP case. By executing both simulations in parallel, the recorded fluctuations of the FP recycling station also serve as HR inflow conditions (as sketched in Fig. 5.2). Consequently, all operations take place within the fast RAM only. This saves many resources compared to the process of storing the  $yz$ -planes of all time steps on the hard disk and reloading them for a subsequent simulation. Additionally, the auxiliary flat plate simulation serves as a perfect comparable reference case with identical inflow conditions. The large streamwise grid dimension  $L_{x-FP}$ , as needed for the Recycling-Rescaling method of the FP case, can be reduced in the HR case:  $L_{x-HR} < L_{x-FP}$ .

## 5. Computational Fluid Dynamics

---

When using the Recycling-Rescaling method, especially upstream traveling pressure waves are highly sensitive to an artificial feedback loop. As a solution to this problem, only density and velocity fluctuations but no pressure fluctuations are recycled. Furthermore, a sponge layer is applied as described in Sect. C.3 acting on the pressure only (see the blue gradient in Fig. 5.2). Within a short distance of the inlet, the TBL quickly recovers all pressure fluctuations as prescribed by the continuous solution of the NSE's. Especially, in the present case of  $M_0 = 0.112$ , this quick pressure recovery is supported by Morkovin's hypothesis (Morkovin, 1962).

### Outlet

The outlet is numerically prescribed by non-reflective boundary conditions (see Sect. C.2), too. Near the wall, in the lower viscous TBL region, the assumptions of the characteristic decomposition are not valid. To overcome this problem the characteristic boundary conditions are combined with a sponge layer (Sect. C.3). In contrast to the inflow, now the sponge layer is acting on all variables. The sponge region is marked again in Fig. 5.2 by a blue gradient.

In contrast to the upper open boundary the reference values of the non-reflecting outlet, cannot all be set just according to their inner neighbors. A correct subsonic outlet treatment should set the reference pressure in physical accordance with  $p_\infty$  far downstream from the calculational domain. If the reference values at the boundary are set directly to be  $p_\infty$ , the boundary conditions are well-posed but create acoustic wave reflections. A well-posed, but acoustically soft pressure reference value is stated by Poinsot and Lele (1992) and Rudy and Strikwerda (1980) as

$$p_{ref} = p - \beta (1 - M_0^2) c / \mathcal{L} (p - p_\infty), \quad (5.6)$$

being  $p$  the original pressure of the NSE's solver before the boundary treatment. [Selle et al. \(2004\)](#) suggest setting the relaxation parameter as  $0.1 < \beta < \pi$ , which is a compromise between mean pressure drifts and reflections, respectively. Here  $\beta$  is  $(0.1 + \pi)/2$ .  $\mathcal{L}$  is the characteristic domain size (here  $L_{x-plate}$ ). In the present case of a ZPG, TBL  $p_\infty$  is equal to  $p_0$ .  $\rho_{ref}$  and  $\mathbf{u}_{ref}$  are set according to a zero gradient along the mean flow direction.

#### Wall

All walls marked black in Fig. 5.1, are adiabatic and have a no-slip condition. Symmetric boundary conditions numerically prescribe them (see Sect. C.4).

#### Initial Condition

Before the main DNS is conducted, a precursor run, with the same physical conditions but a reduced number of gridpoints (underresolved) is simulated. As an initial condition, the analytic solution of a Van-Driest profile (derived in Sect. 3.2) is disturbed by synthetic perturbations following the article of [Pirozzoli et al. \(2008\)](#). These synthetic perturbations mimic inner and outer layer streaks, in order to quickly converge to a fully turbulent flow. In doing so, the initial conditions inside the neck and cavity of the HR case have zero velocity and constant density  $\rho_0$  and pressure  $p_0$ .

Based on the final state of the precursor run, the initial conditions of the main DNS are interpolated.

#### Production Procedure

Three steps are carried out to conduct the final DNS of the FP and the HR case.

## 5. Computational Fluid Dynamics

---

First, the unresolved precursor run of both FP and HR case is simulated for a non-dimensional time  $\mathcal{T} \equiv \Delta_T u_0 / \delta_{99FP-inlet} = 200$ , being  $\Delta_T$  the total physical running time.

Second, a fully resolved DNS of the FP case (for spatial resolution see Tab. 5.1) is conducted for  $\mathcal{T} = 62$  time units, to populate the whole domain with physical turbulence at all scales.

Third, the DNSs of the FP and the HR case (resolution listed in Tab. 5.1) are executed at the same time for another  $\mathcal{T} = 227$  time units. In doing so, after the first  $\mathcal{T} = 90$  time units, the mean flow profiles no longer change, and the initial transient is completed. This is in agreement with [Brouwer \(2016\)](#). Hence, to avoid any distortion of the results by initial transients, only the last  $\mathcal{T} = 137$  time units are used for statistical evaluation (Chap. 7 and Chap. 8). With  $\delta_{99FP-inlet} = 5,62$  mm and  $u_0 = 38,5$  m/s, 137 time units correspond to a total evaluable physical duration of approximate 20 ms.

### Mesh Resolution

The mesh of a DNS needs to be refined in such a way, that the smallest system scale  $\eta$  (also known as Kolmogorov scale) is resolved locally. To calculate a priori the needed grid spacing in case of a TBL, the relation

$$\eta \approx 2\delta_\nu \tag{5.7}$$

of [Stanislas et al. \(2008\)](#) between the smallest scale  $\eta$  and the viscous length scale  $\delta_\nu$  can be applied. To calculate the viscous length scale  $\delta_\nu$  just the mean Van-Driest velocity profile as stated in pseudocode 3.1 needs to be known. Tab. 5.1 lists the resulting dimensions of the final DNS for the FP and the HR case. At this, the resolution is similar to other recent TBL DNS studies ([Pirozzoli et al., 2008](#)). Grid stretching is applied to reduce the cost of the computation (see the mesh in Fig. 2.1).

### 5.3 Direct Numerical Simulation Setup

The maximal variation of cell spacing between two neighboring cells is less than 0.5%.

To validate the DNS, the kinetic energy spectrum of an  $xz$ -area in the TBL is calculated. The dissipation range is fully resolved, as almost no energy is contained in wavelengths smaller than  $\eta$  (see Fig. 5.3). Nearly the same energy spectrum applies to the HR case (not shown here). Therefore, the a priori estimation of Eq. 5.7 is confirmed.

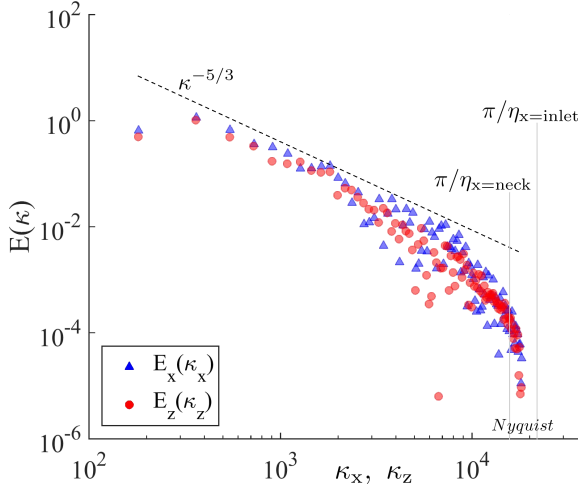


**Figure 5.3:** Log-log TBL energy spectrum of an  $xz$ -area at a constant height of  $y = 24\delta_\nu$  (FP). The energy distributions of the streamwise  $|u'_x|^2$  (blue triangles) and the spanwise  $|u'_z|^2$  (red bullets) velocity fluctuations are almost the same.

This figure has been taken from [Stein et al. \(2018\)](#).

## 5. Computational Fluid Dynamics

---

**Table 5.1:** The spatial resolution of the DNS. Since there is no mean flow in the spanwise direction the  $\Delta z^+$  can be bigger than  $\Delta x^+$ ,  $\Delta y^+$  (Pirozzoli et al., 2008). The grid spacing is normalized with the viscous length scale  $\delta_\nu$  (Eq. 3.18) of the TBL (wall units).

Block	Range of grid spacing			Grid lengths in mm		
	$\Delta x^+$	$\Delta y^+$	$\Delta z^+$	$L_x$	$L_y$	$L_z$
Channel	1.7-2.4	1.6-5.9	3.7	135	44	117
Neck	1.7	1.6	3.7	14	1	100
Cavity	1.7-2.4	1.6-6.0	3.7	100	144	100
Flat plate	1.7-2.4	1.6-5.9	3.7	260	44	117

Block	Gridpoints			CPUs per dimension		
	$n_x$	$n_y$	$n_z$	$c_x$	$c_y$	$c_z$
Channel	1440	288	672	32	9	32
Neck	180	24	582	6	2	6
Cavity	912	912	576	48	19	16
Flat plate	2304	288	672	48	6	48

This chapter deals with the “break down” of complex dynamical systems, for instance, to post-process DNS data. By “break down”, a modal decomposition into manageable sub-systems is meant. If a suitable decomposition is found, the individual sub-systems are understood and controlled better. There are many decompositions, each of them dividing the dynamics according to a particular rule: The Proper Orthogonal Decomposition (POD) sorts by energy content; the Spectral Decomposition sorts by frequency. The Dynamic Mode Decomposition (DMD) decomposes a system into frequency components and their corresponding growth or decay rates. Since this work focuses on the frequency dependent acoustic damping or excitation, the DMD is applied as a post-processing tool.

## 6.1 Dynamic Mode Decomposition

In the following, the DMD is presented as originally published by [Schmid and Sesterhenn \(2008\)](#). If any temporal series of system states (experimental or numerical) is given, the DMD can reconstruct the underlying evolution operator, which is generating the snapshot dynamics. The reconstructed operator can even serve for a substitute stability analysis of the original (possibly unknown) system operator. In the present case, it is costly to analyze the full discretized Navier-Stokes operator directly. The non-linear NSEs can be approximated by the linear time step operator  $A \in \mathbb{R}^{M \times M}$ :

$$\frac{d}{dt} \mathbf{q}(t) = A \mathbf{q}(t). \quad (6.1)$$

## 6. Modal Analysis

---

$\mathbf{q}$  is the three-dimensional flowfield reshaped into a one-dimensional vector of the spatial dimension  $M$ . In this linear case, the generic solution of this ordinary matrix differential equation is known:

$$\mathbf{q}(\mathbf{x}, t) = \sum_i c_i \mathbf{a}_i(\mathbf{x}) e^{\sigma_i t}, \quad (6.2)$$

being  $\mathbf{a}_i$  the eigenvectors and  $\sigma_i$  the eigenvalues of  $A$ . The initial conditions determine the scalar constants  $c_i$ . If  $\text{Re}[\sigma_i] < 0$ , the linear stability of a system component  $i$  follows. The imaginary part of the eigenvalue  $\sigma_i$  determines the frequency of the corresponding eigenbasis vector. In most practical problems (present DNS) the eigendecomposition of the evolution operator  $A$  is too expensive (already for a single time step).

The idea of the DMD is to eigendecompose not  $A$  directly but a reduced companion matrix  $A_C$ , which holds the most energetic parts of  $A$ . Furthermore, the DMD assumes that a constant  $A$  exists, which can linearly map not only a single time step to the next but a whole sequence of  $N$  flowfield snapshots  $\mathbf{q}_i$  (each  $\mathbf{q}$  has  $M$  elements), which are ordered and equally spaced<sup>1</sup> in time:

$$A \underbrace{\{\mathbf{1}\mathbf{q}, \mathbf{2}\mathbf{q}, \dots, \mathbf{N-1}\mathbf{q}\}} = \underbrace{\{\mathbf{2}\mathbf{q}, \mathbf{3}\mathbf{q}, \dots, \mathbf{N}\mathbf{q}\}},$$

$$A \quad Q_1 \quad = \quad Q_2, \quad (6.3)$$

$$A^m \quad n\mathbf{q} \quad = \quad \mathbf{n+m}\mathbf{q}. \quad (6.4)$$

The lower prescript “ $n\bullet$ ” denotes the time step. If the operator  $A$  is applied  $m$  times, the flowfield  $\mathbf{q}$  advances  $m$  steps in time. A

---

<sup>1</sup>By now Guéniat et al. (2015) developed a DMD extension for arbitrarily spaced snapshots.

## 6.1 Dynamic Mode Decomposition

---

transformation from  $A$  to a representative companion matrix

$$A_C = U^{-1} A U \quad (6.5)$$

is given by the left-singular vectors ( $U$  columns) of the Singular Value Decomposition (SVD)

$$Q_1 = U \Sigma V^H \quad (6.6)$$

of  $Q_1$ .  $\Sigma$  is a diagonal matrix.  $U^{-1} = U^H$  and  $V^{-1} = V^H$  are unitary matrices.  $V^H$  is the conjugate transpose of  $V$ . A QR decomposition can be used as an alternative to the SVD, too (Schmid, 2010). If  $Q_1$  has a rank deficiency, SVD algorithms are typically more robust. A tunable reduction of  $A_C$  is achieved by truncation of the SVD, i.e., by approximating

$$\begin{aligned} Q_1 &\approx \underbrace{U(:, 1:r)} \quad \underbrace{\Sigma(1:r, 1:r)} \quad \underbrace{V(:, 1:r)^H}, \\ Q_1 &\approx \quad U_r \quad \quad \Sigma_r \quad \quad V_r^H. \end{aligned} \quad (6.7)$$

A falling singular value orders the diagonal entries of  $\Sigma$ , which can be typically related to the energy content (like a POD). Therefore, the arbitrary reduction index  $r$  ( $r < M$ ) corresponds to the least energetic basis vector spend to map  $A \in \mathbb{R}^{M \times M}$  to  $A_C \in \mathbb{R}^{r \times r}$ . Using Eq. 6.3 and Eq. 6.7 the companion matrix  $A_C$  can be calculated from  $Q_2$  and the truncated SVD of  $Q_1$ :

$$A_C = U_r^{-1} A U_r = U_r^H Q_2 V_r \Sigma_r^{-1}. \quad (6.8)$$

The eigenvalues  $\lambda_i$  and eigenvectors  $\varphi_i$  of the reduced companion matrix  $A_C$  can be computed  $A_C \varphi_i = \lambda_i \varphi_i$  at lower costs, compared to the

## 6. Modal Analysis

---

eigendecomposition of  $A$ . Analog to Eq. 6.4 the time evolution of the  $i^{\text{th}}$  eigenvector of  $A_C$  is

$${}_{n+m}\boldsymbol{\varphi}_i = \lambda_i^m {}_n\boldsymbol{\varphi}_i, \quad (6.9)$$

being  $n$  the start time step, and  $m$  the number of proceeded time steps. The dynamic mode decomposition is now given by the back-transformation of  $\boldsymbol{\varphi}$  to the full-dimensional system

$$\boldsymbol{\phi}_i = U_r \boldsymbol{\varphi}_i. \quad (6.10)$$

$\boldsymbol{\phi}_i \in \mathbb{R}^{M \times 1}$  are called the unscaled dynamic modes. Like the eigenvectors  $\boldsymbol{\varphi}_i$  before, the dynamic modes  $\boldsymbol{\phi}_i$  determined via the SVD are sorted by their energy level. An easy way of scaling is to determine the normalization coefficients  $\mathbf{c}$  based on the initial snapshot  ${}_1\mathbf{q}$  by solving the linear system

$$\{\boldsymbol{\phi}_1, \boldsymbol{\phi}_1, \dots, \boldsymbol{\phi}_r\} \mathbf{c} = {}_1\mathbf{q}. \quad (6.11)$$

For an optimal reconstruction of all snapshots, Tissot et al. (2014) propose a temporally weighted norm. As an alternative, in the present work, the normalization coefficients based on all snapshots (as in 6.11) are determined first and then temporally averaged.

The evolution of the system is provided by

$${}_n\mathbf{q} = \sum_{i=1}^r \mathbf{c}_i \boldsymbol{\phi}_i \lambda_i^n. \quad (6.12)$$

By comparison with Eq. 6.2 the eigenvalues of the DMD can be related to the standard eigenvalues of the linear stability analysis by

$$\sigma_i = \frac{\ln(\lambda_i)}{\Delta t}, \quad (6.13)$$

being  $\Delta t$  the equal spacing of the snapshots  $\mathbf{q}_i$ . Rowley et al. (2009) even show that these eigenvalues  $\sigma_i$  are approximations to the nonlinear stability analysis (Koopman eigenvalues). The angular frequency determination  $\omega_i = \mathbb{I}[\sigma_i]$  of the DMD is resistant to deficient input data. Though, unlike the Fourier transform, it should be noted that the DMD frequency spectrum is not equidistant.

In contrast to the frequency determination of the DMD, there is much discussion about the growth or decay rate  $Re[\sigma_i]$ . To achieve the most similarity to a nonlinear stability analysis Chen et al. (2012) recommend to subtract an equilibrium point (base flow) of the snapshot sequence first. This guarantees that the reconstruction of the dynamic modes (Eq. 6.10) meets the boundary conditions. In another case of centered snapshots as DMD input (mean subtraction), Chen et al. (2012) claim that the DMD is equivalent to a harmonic averaged temporal discrete Fourier transform. This implies that the growth rate is always zero. However Cammilleri et al. (2013) show that this is only true if the temporal dimension  $N$  of the snapshot basis is much smaller than the spatial dimension  $M$ . The correct detection of growth rates, also for mean subtracted snapshots, is also confirmed by Bistrian and Navon (2014). In any case, a growth rate analysis is only possible if enough snapshots are provided. The local temporal evolution may deviate significantly from the global dynamics.

A summarized DMD algorithm is listed in the pseudocode 6.1 and is executed in Sect. 8.4.1.

## 6. Modal Analysis

---

**Pseudocode 6.1:** Dynamic Mode Decomposition via SVD.

1. Order  $N$  snapshots according to Eq. 6.3

$$Q_1 = \{\mathbf{1}\mathbf{q}, \mathbf{2}\mathbf{q}, \dots, \mathbf{N-1}\mathbf{q}\},$$
$$Q_2 = \{\mathbf{2}\mathbf{q}, \mathbf{3}\mathbf{q}, \dots, \mathbf{N}\mathbf{q}\}.$$

2. Compute the reduced SVD of  $Q_1$  (Eq. 6.7)

$$Q_1 \approx U_r \Sigma_r V_r^H.$$

3. Construct the reduced companion matrix  $A_C$  of  $A$  (Eq. 6.8)

$$A_C = U_r^H Q_2 V_r \Sigma_r^{-1}.$$

4. Decompose the eigenvalues  $\lambda_i$  and eigenvectors  $\boldsymbol{\varphi}_i$  of  $A_C$ .
5. Project the eigenvectors (modes)  $\boldsymbol{\varphi}_i$  of  $A_C$  back onto the full-dimensional space (Eq. 6.10)

$$\boldsymbol{\phi}_i = U_r \boldsymbol{\varphi}_i.$$

6. Approximate the eigenvalues of the global stability analysis

$$\sigma_i = \ln(\lambda_i)/\Delta t.$$

7. Optionally (not carried out here), reconstruct the time evolution by (Eq. 6.12)

$$\mathbf{q}(\Delta t n) = \sum_{i=1}^r \mathbf{c}_i \boldsymbol{\phi}_i \lambda_i^n.$$

## 6.2 Resolvent Analysis

The resolvent analysis is suitable to study the sensitivity of eigenvalues regarding small perturbations and to measure the non-normality of a given system matrix, such as to identify the linear dependency (coupling) of eigenvectors (Trefethen, 1999, Sect.1.2).

In this work, certain characteristic frequencies which correspond to KH waves or acoustic cavity modes and their interactions are of special interest. As discussed in the previous Sect. 6.1, these frequencies correspond to eigenvalues of the system evolution matrix. To study all eigenvalues, the resolvent analysis is too expensive. In the present case, a selected set of interesting eigenvalues are identified a priori. Using the reduced companion matrix  $A_C$ , provided by the DMD (Sect. 6.1) instead of the full system matrix  $A$ , further reduces the efforts of the resolvent analysis.

The idea of the resolvent analysis is not to calculate the spectral decomposition, i.e., the eigendecomposition of a system matrix  $A_C$ , but a so-called  $\epsilon$ -pseudospectrum:

$$|(z\mathbf{1} - A_C)^{-1}| > 1/\epsilon. \quad (6.14)$$

The  $\epsilon$ -pseudospectrum is the norm (here the euclidean  $L^2$ -norm is used) of the resolvent  $(z\mathbf{1} - A_C)^{-1}$  of  $A_C$  at the complex scalar value  $z \in \mathbb{C}$ .  $\mathbf{1}$  is the identity matrix. In practice, the norm of the resolvent can be more easily calculated by determining the smallest singular value  $s_{min}$  of a SVD of  $z\mathbf{1} - A_C$ :

$$|(z\mathbf{1} - A_C)^{-1}| = \frac{1}{s_{min}(z\mathbf{1} - A_C)}. \quad (6.15)$$

## 6. Modal Analysis

---

If  $z$  is an eigenvalue of  $A_C$ , the resolvent becomes infinity and  $\epsilon = 0$ . The evaluation of the resolvent ( $z \in \mathbb{C}$ , i.e., entire complex plane) is restricted to the surrounding of preselected eigenvalues to save computational cost. For different values of  $\epsilon$  (Eq. 6.14), contourlines of the pseudospectrum are calculated (level sets of  $|(z\mathbf{1} - A_C)^{-1}|$ ). If eigenvalues are separable by many different contourlines belonging to a large range of  $\epsilon$  values they are less sensitive to perturbations. Furthermore, their corresponding eigenvectors are normal, i.e., linearly independent. The smaller the  $\epsilon$  range becomes to distinguish two eigenvalues, the greater is their non-normality.

Sect. 8.4.4 applies the resolvent analysis.

# Fluid Dynamical Results and Discussion

# 7

This chapter is partially based on [Stein and Sesterhenn \(2019a\)](#).

One by one, this chapter presents and discusses the fluid dynamical results of the conducted DNS. The evaluation first focuses on averaged quantities (Sect. 7.1), second on instantaneous variables (Sect. 7.2) and third on the  $k_x - \omega$ -spectral space (Sect. 7.3), which is better suited for acoustics.

In particular, the modifications of the characteristic fluid structures due to the presence of the Helmholtz resonator are revealed by comparison with the case of the flat plate flow without any resonant cavity but with identical inflow conditions (cf. FP and HR case in Sects. 2.1 and 5.3).

At last, most significantly, unique features of the shear layer (constancy of inflection points) at the neck opening of the HR case are found and utilized to define universal parameters for the Helmholtz resonator model (Sect. 7.4).

### 7.1 Mean Velocity Profiles

#### FP Velocity Profile

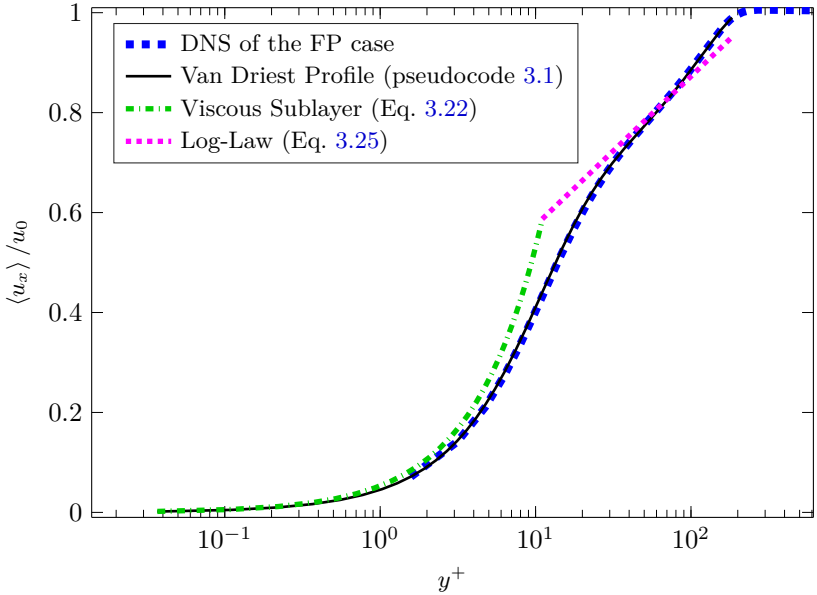
To validate the DNS, first, the compressible TBL is compared with the analytical solution of Van Driest (pseudocode 3.1). The Van Driest’s solution itself is generally conceded as valid (Guarini et al., 2000; Pirozzoli et al., 2010; White, 2006).

Fig. 7.1 illustrates the agreement between the analytical Van Driest profile and the temporarily and spanwise averaged DNS of a turbulent FP flow. The streamwise  $x$ -position of the FP TBL is chosen such that the boundary layer thickness  $\delta_{99}$  is equal to  $\delta_{99,neck}$  (see discussion of Fig. 7.4) of the case with mounted HR. As a reference, the law of the viscous sublayer (Eq. 3.22) and the Log-Law (Eq. 3.25) is shown. The higher the Reynolds number, the longer the Log-Law region of the TBL profile. In the present case,  $Re_{\delta_{99,neck}}$  is “just” 3573. Hence the Log-Law region is hardly visible.

Schlichting (1979) estimates that the laminar-turbulent transition of a flat plate (ZPG) begins at  $u_0\delta^*/\nu = 520$  and completes at  $u_0\delta^*/\nu = 950$ . In terms of  $Re_{\delta_{99,neck}}$  with the ratio of  $\delta_{99,neck}/\delta_{neck}^* = 5.4$ , this leads to a critical transition range of  $Re_{\delta_{99,neck}} \in [2800, 5100]$ . Thus the present Reynolds number of “just”  $Re_{\delta_{99,neck}} = 3573$  belongs in fact to a “young” TBL.

#### HR Velocity Profile

In case of the flush-mounted HR the original TBL profile (Van Driest like) continuously changes to a shear layer and retransforms to the original TBL profile. In Fig. 7.2 such a set of velocity profiles originating



**Figure 7.1:** Normalized mean spanwise flow of a FP TBL over the logarithmic height in terms of wall units  $\delta_\nu$ . Sect. 2.1 introduces the FP case. The thick dashed blue line depicts time and spanwise averaged DNS results. The thin black line behind the blue dashes is the analytical solution of the Van-Driest profile as stated in pseudocode 3.1.

from the DNS with HR is evaluated for different streamwise positions around the neck.

To analyze this TBL shear layer transition in more detail in Fig. 7.3 the velocity profiles are reshaped (compared to Fig. 7.2 the  $x$ - and  $y$ -axis are swapped), normalized and put on top of each other. With increasing streamwise  $x$ -position the colormap varies from black to yellow. To visualize the evolution of profiles, their two lower inflection points are highlighted: Black and blue bullets, respectively mark the first and

## 7. Fluid Dynamical Results and Discussion

---

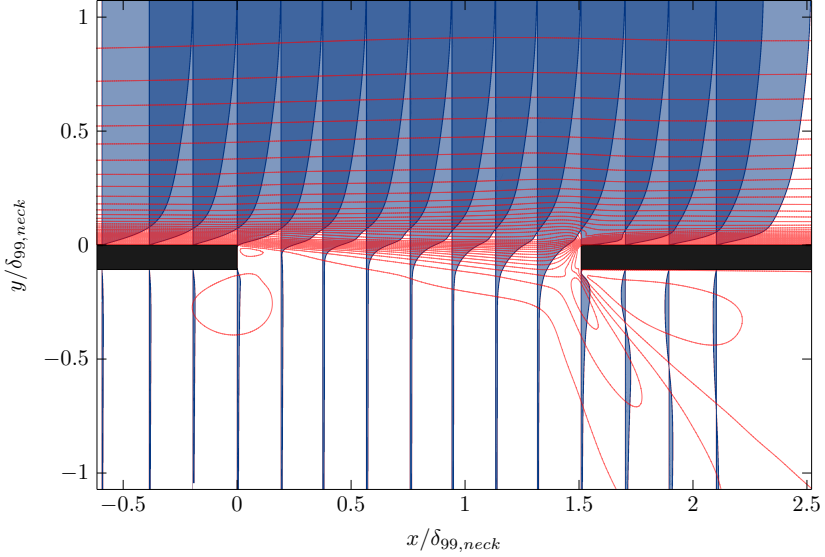


**Figure 7.2:** Streamwise transition from a TBL profile to a shear layer profile and back to a TBL of a flat plate flow with a flush-mounted HR beneath. The adiabatic, no-slip walls are colored black. The streamwise velocity component  $u_x$  is time and spanwise averaged and represented by overlapping blue profile areas. Red lines indicate isolines of the absolute velocity  $|u|_{iso}$ . Due to the small opening compared to the cavity size (see Fig. 2.1) there is nearly no flow inside the cavity below the wall. Only a small fraction of the mean stream is roughly deflected  $45^\circ$  down into the cavity (see red isolines in the lower right), creating a secondary recirculation bubble at the downstream ceiling of the cavity.

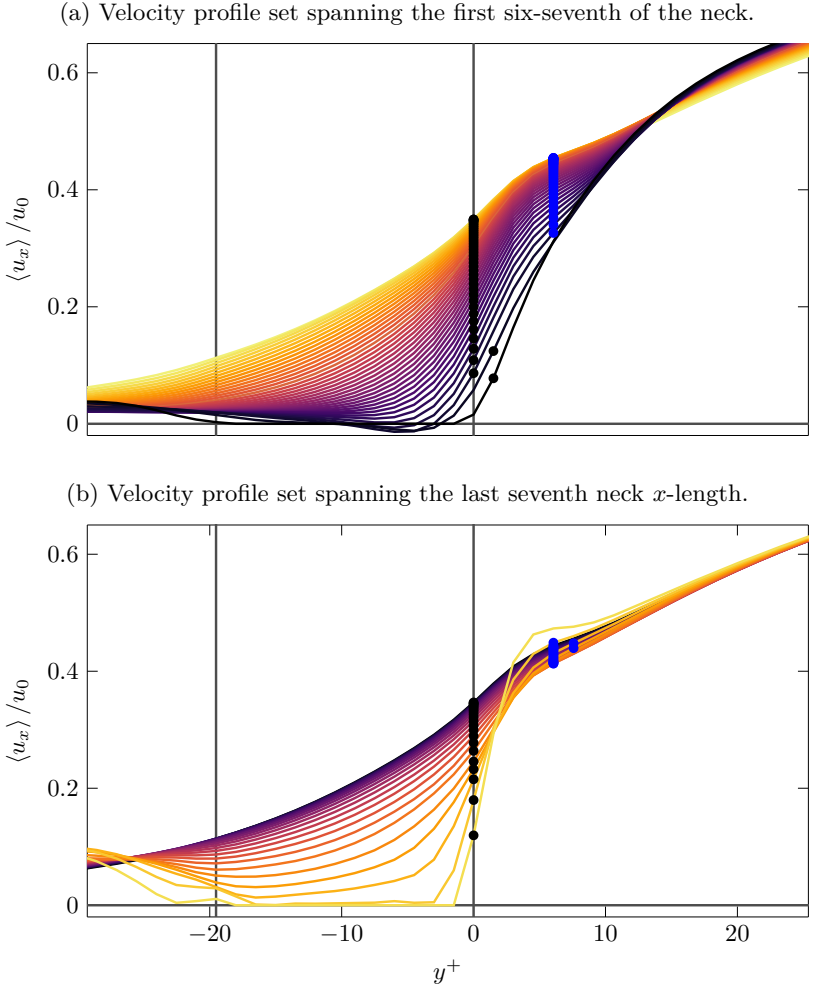


**Figure 7.3:** Non-dimensional velocity profiles of the HR DNS (Sect. 2.2). (a) Profiles for different streamwise positions, starting with the leading edge of the neck at  $x = 0$  (black line) up to  $x = 6/7 L_{x-neck}$  (yellow line). (b) Continuation of the subfigure (a) profiles, starting at  $x = 6/7 L_{x-neck}$  (black line) and ending at the trailing edge at  $x = L_{x-neck}$  (yellow line). Again, all profiles are time and spanwise averaged. The plate surface (at  $y^+ = 0$ ) and the cavity ceiling are indicated by the two vertical black lines, with a distance of  $L_{y-neck} = 19.5\delta_\nu$ .

## 7. Fluid Dynamical Results and Discussion

---

second inflection points. As it transpires beautifully, both inflections points have a constant height  $y$  for all streamwise  $x$ -positions within the accuracy of the DNS mesh (see grid spacing of  $\Delta y^+(y=0) = 1.6$  in Tab. 5.1). Sect. 7.4 utilizes this characteristic shear layer feature to define the model parameters. The first inflection point is located on the wall  $y^+ = 0$  (second vertical black line), while the second inflection point is located at  $y^+ \approx 6$  ( $y/\delta_{99,neck} \approx 0.03$ ). A third top inflection point scattering around  $y^+ \approx 13$  (without a constant height) is not marked to keep the Fig. 7.3 clear. The characteristic curvature change of the two outer inflection points (first and third) meets the Fjørtoft's criterion (Schmid, 2012) necessary for a shear layer instability in contrast to the second central inflection point. The constant height of the two lower inflections point is in agreement with the experimental study of Elder (1980). However, the spatial resolution of his measurements is not sufficient to detect all three inflection points.

### FP and HR Velocity Profile Growth

In Fig. 7.4 the streamwise growth of the boundary layer thickness  $\delta_{99}$  as defined by Eq. 3.23 is plotted, juxtaposing the FP and the HR case. Also, Prandtl's  $\delta_{99} \propto x^{4/5}$  power-law of a low Reynolds number TBL is displayed fitting the FP case. The present TBL with  $Re_{\delta_{99,neck}} = 3573$  is not yet growing as rapidly as a fully developed TBL with  $\delta_{99} \propto x^{6/7}$  (White, 2006, Sect. 6-6.1). The location of the neck is marked by the two gray vertical lines at  $x = 0$  and at  $x = 1.5\delta_{99,neck} = L_{x-neck}$ . Far upstream of neck opening the Helmholtz resonator has no effect on  $\delta_{99}$ , but already  $0.8\delta_{99,neck}$  ahead of the leading edge of the neck, extra velocity generation (related to the neck shear layer) gives rise to a thickening of the boundary thickness, which drops  $0.8\delta_{99,neck}$  behind the downstream edge even below the undisturbed FP boundary layer

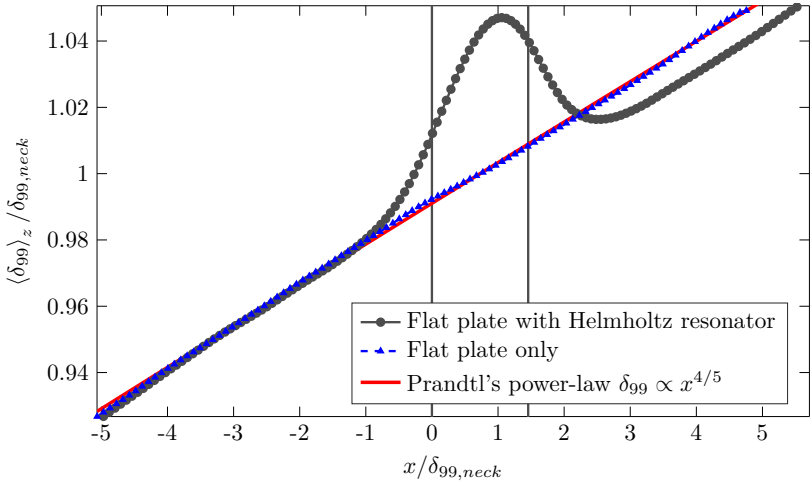


**Figure 7.4:** Time and spanwise averaged TBL thickness over the streamwise length  $x/\delta_{99,neck}$ .  $\delta_{99}$  is the interpolated height, where the streamwise velocity is  $u(y = \delta_{99}) = 0.99 u_0$ , being  $u_0$  the free stream velocity. The underlying thick red line is Prandtl's power-law of a low Reynolds number TBL serving as a reference.

thickness. An explanation for this drop could be a boundary layer bleed through the cavity.

At the center of the neck, the undisturbed thickness of the FP case is  $\delta_{99,neck} = 9.28$  mm. This is the reference boundary layer thickness used throughout this work (cp. Fig. 2.1). In contrast, the thickness in case of the HR is increased by 5% up to a local maximum of  $\delta_{99,max} = 1.05\delta_{99,neck}$  at  $x = \delta_{99,neck}$  (the neck center is located at  $x = 0.75\delta_{99,neck}$ ).

### 7.2 Instantaneous Velocity Fluctuations

Note that parts of this section are published in [Stein et al. \(2018\)](#).

Below the instantaneous velocity and vorticity structures of the FP case and the HR case are compared at the same settled system stage (after 40 ms). The influence of the mounted HR on the original undisturbed fluctuations of a FP TBL flow can be quantified. By identifying the characteristic HR velocity fluctuations first, a more realistic HR model can be developed later.

#### Differences between FP and HR Velocity

Fig. 7.5 shows a  $xy$ -slice subsection of a  $u_y$  velocity snapshot. Above the wall ( $y > 0$ ) the FP (see Subfig. 7.5(a)), and the HR case (see Subfig. 7.5(b)) appear very similar, even though the orifice of the resonator gives rise to a strong KH instability. The most visible vortex detachment is thereby directed downwards into the cavity (visible by the negative, i.e., black  $u_y$  component). If one takes the difference of the FP and the HR case (Subfig. 7.5(c)), modifications of the velocity fluctuations become mainly visible downstream of the trailing neck edge through more streaks. Upstream of the orifice, the velocity differences drop close to zero as expected by the same given inflow conditions.

At the same system time as before (after 40 ms), Fig. 7.6 shows a  $u_y$  velocity snapshot again. This time not a  $xy$ -area but a  $xz$ -area is cut out from the three-dimensional DNS data. To demonstrate the HR impact a constant height of  $y^+ \cong 12$  near the wall is selected. The white dots indicate the underlying neck edge of the cavity. By comparing FP and HR (Subfig. 7.6(a) and Subfig. 7.6(b), respectively), the similarity of all turbulent streaks outside the neck area is apparent

again also downstream. By taking the  $u_y$  velocity difference of FP and HR (Subfig. 7.6(c)), the neck edge is visible even without white markers. A streamwise increasing  $u_y$  velocity amplitude reflects the thickening of the boundary layer thickness in the neck area. This is consistent with the thickening of the boundary thickness in Fig. 7.4.

By comparing the FP and the HR case (Figs. 7.5, 7.6), it becomes visible, that both cases are excited by almost the same incoming turbulence fluctuations as intended by the DNS setup described in Sect. 5.3. This is not self-evident since  $L_{x-HR} < L_{x-FP}$  and  $\delta_{99FP-inlet} < \delta_{99HR-inlet}$ .

## 7. Fluid Dynamical Results and Discussion

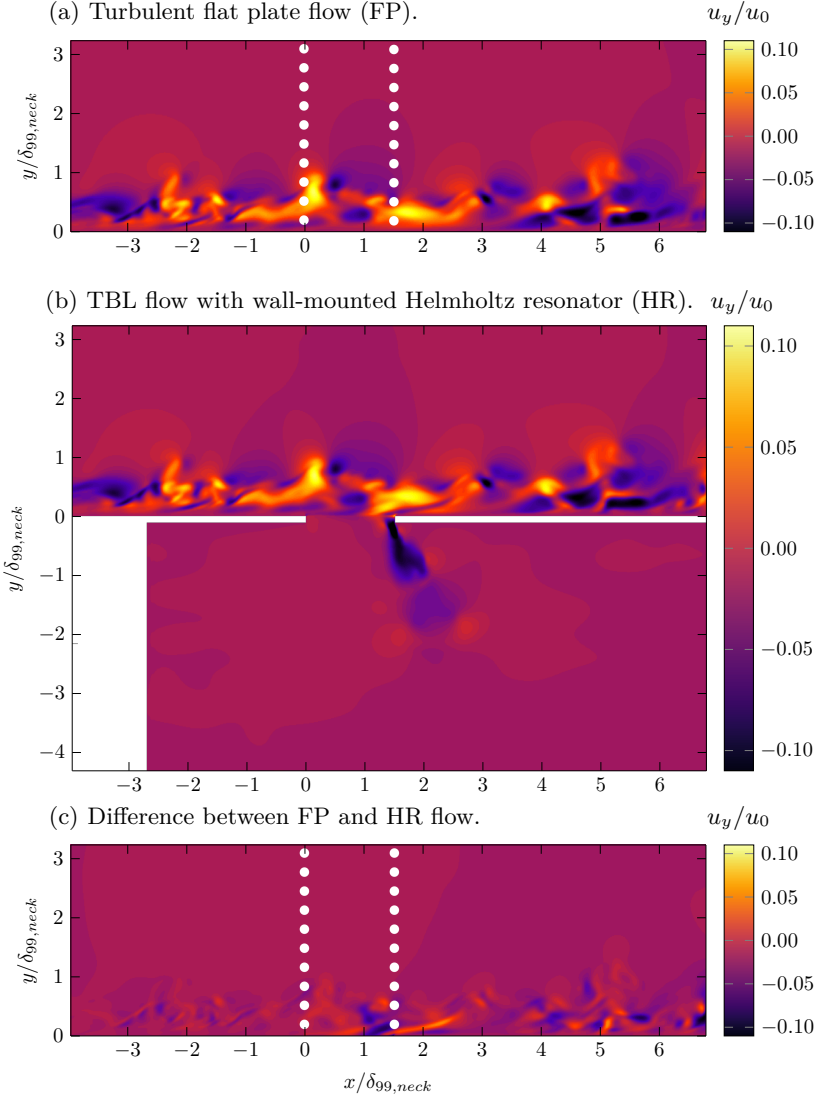
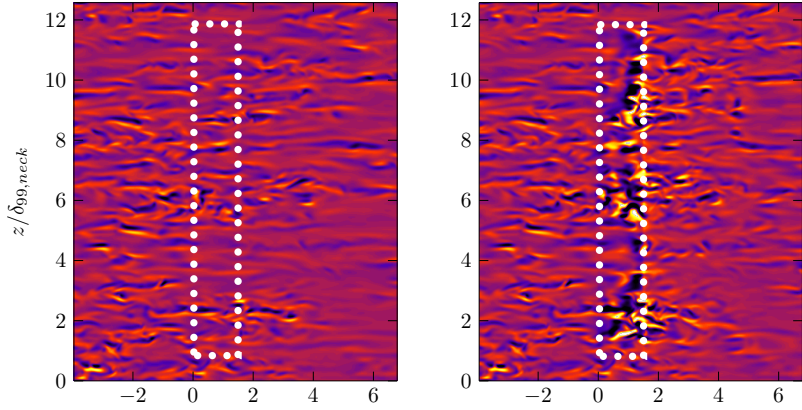


**Figure 7.5:** Snapshot of the non-dimensionalized vertical  $u_y/u_0$  velocity component. Only a section of the  $xy$ -area at the spanwise neck center  $z = 0.5L_{z-neck}$  is shown. The leading edge of the neck is located at  $x/\delta_{99,neck} = 0$ , whereas the plate beginning, i.e., the inlet of the DNS domain, is located at  $x/\delta_{99,neck} = -21.2$ .

## 7.2 Instantaneous Velocity Fluctuations

(a) Turbulent flat plate flow (FP).      (b) TBL with mounted cavity (HR).



(c) Difference between FP and HR.

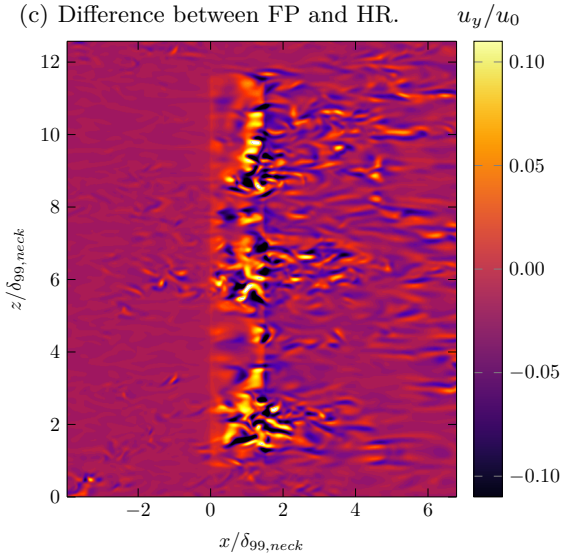


**Figure 7.6:** Snapshot of the vertical velocity component. The color bar shows the magnitude of  $u_y/u_0$ . An  $xz$ -area cut at a constant height of  $y^+ \cong 12$  close to the wall is shown. A rectangle of white dots highlights the underlying opening of the cavity.

### HR Vorticity Isosurfaces and the Identification of Howe's Vortex Sheet

To verify the existence of a thin vortex sheet covering the upper side of the neck as claimed by **Howe** (cf. Sect. 4.4), vorticity isosurfaces at  $St_{neck} = L_{x-neck}/u_+ (\nabla \times \mathbf{u}) = \pm 2.80$  are calculated, colored red and blue and displayed in Fig. 7.8. In contrast to the dominant vortices of the primary TBL, a secondary vortex sheet, detaching from the upstream edge of the neck and covering the neck opening at the height of  $y \sim 0$ , can be visually distinguished. For a better understanding, the secondary vortex sheet is colored red and blue in Fig. 7.8. During the previous discussion of the mean velocity profiles, three inflection points reflected the presence of this secondary vortex sheet already. A standard shear layer has a single inflection point. The secondary vortex sheet, revealed here, leads to an additional locally restricted bulging of the flow profile, which is accompanied by two additional inflection points (Fig. 7.3). In addition, the secondary vortex sheet leads to reattachment of the TBL on the wall for a small stretch downstream of the neck. In Fig. 7.8 for about one  $L_{x-neck}$  downstream of the neck no (white) spacing between the lowest TBL whirled and the plate is visible. This is consistent with the lowering of  $\delta_{99}$  downstream of the opening (see Fig. 7.4: HR case relative to the FP case).

Inside the cavity, whirled are only present near the opening. The size ratio of the small neck and the large cavity is apparent in Fig. 7.7. The same is true for a snapshot at another time or a different vorticity frequency than  $St_{neck} = 2.80$ . **Howe's** assumptions made in Sect. 4.4 seem to be fairly reasonable: Acoustic waves can propagate inside the cavity without any fluid-related effects. The first interaction of the acoustic waves (inside the cavity) with the turbulent flow (above the cavity) takes place at the vortex sheet of the opening.

**Figure 7.7:** Auxiliary figure to illustrate the trim area of Fig. 7.8 (blue dashed box) with respect to the entire calculation domain. Exact proportions are used. Walls are painted black. TBL inflow, outflow, and open boundary conditions are dashed in red. The green squares at the plate wall mark a section with a  $x$ -length of  $12.6\delta_{99,neck}$  ( $8.3L_{x-neck}$ ), which is spectrally evaluated in the following (cf. Figs. 7.9, 7.10 and 7.13).

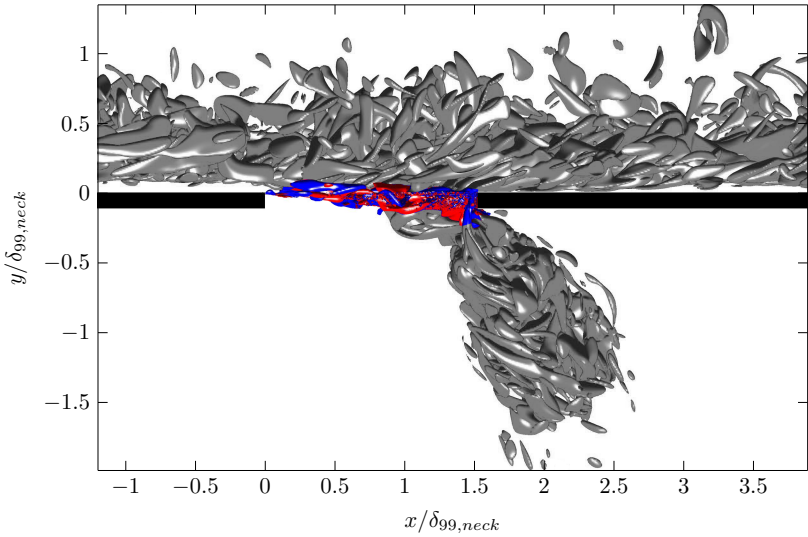
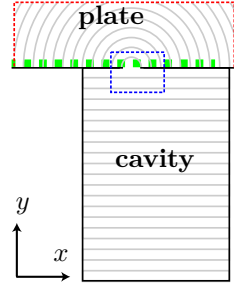


**Figure 7.8:** Snapshot of two vorticity isosurfaces with  $St_{neck} = \pm 2.80$  (colored blue and red) near the HR neck. To highlight Howe's secondary vortex sheet of the neck, everything else is grayed out, such as the primary TBL streaks and the vortices inside the cavity. The wall thickness is  $L_{y-neck} = 0.11\delta_{99,neck} = 19.5\delta_\nu$ .

## 7.3 Turbulent Boundary Layer Spectra

**Stein and Sesterhenn (2017b)** presented this section at the European Turbulence Conference 16.

As a first step, to derive the governing parameters and constants of the new spectral model, the following Sect. 7.3.1 evaluates the SPL  $k_x - \omega$ -spectrum of the FP and the HR case. Sect. 7.3.2 introduces a spectral model for the FP case. Later it serves as a source term for the final Helmholtz resonator model (see  $\Phi_{TBL}$  term of Eq. 4.28).

### 7.3.1 The $k_x - \omega$ -Spectrum

To convert the pressure fluctuations from the real  $x - t$ -space to the  $k_x - \omega$ -space (the streamwise component of the wavevector and angular frequency), a Fourier transformation is executed in time and space. More specifically, the power spectral density  $\Phi_{p'p'}$  is calculated, which is defined as a Fourier transformation of the time-averaged autocorrelation of the pressure fluctuations  $p'$ :

$$\Phi_{pp}(k_x, y, z, \omega) \equiv \frac{1}{8\pi^3} \iint_{-\infty}^{\infty} \langle p'(x, y, z, t)p'(x + \xi, y, z, t + \tau) \rangle e^{-i(k_x \xi - \omega \tau)} d\xi d\tau. \quad (7.1)$$

Utilizing the Wiener-Khinchin theorem and the Discrete Fourier Transformation (DFT), the power spectral density  $\Phi_{p'p'}$  of the discrete

### 7.3 Turbulent Boundary Layer Spectra

---

DNS data can be approximated by (Alessio, 2016; Salze et al., 2014)

$$\Phi_{pp}(k_x, y, z, \omega) \cong \frac{1}{NM f_{st} f_{sx}} \left| \sum_{m=1}^M \sum_{n=1}^N p'(x_m, y, z, t_n) e^{i\omega t_n} e^{ik_x x_m} \right|^2, \quad (7.2)$$

with the sampling rate  $f_{st} = N/T$  of the time period  $T$  with  $N$  time steps and the sampling rate  $f_{sx} = M/L$  of the length  $L$  with  $M$  gridpoints, respectively. From the power spectral density  $\Phi_{p'p'}$  the sound pressure level (SPL) spectrum follows directly:

$$\text{SPL}(k_x, y, z, \omega) = 10 \log_{10} \left[ f_{\text{bin}} k_{\text{bin}} \frac{\Phi_{p'p'}(k_x, y, z, \omega)}{p_{\text{ref}}^2} \right] \text{ dB}, \quad (7.3)$$

with the frequency bin  $f_{\text{bin}} = 1/T$ , the wavevector spacing  $k_{\text{bin}} = 1/L$  and the standard threshold of human hearing  $p_{\text{ref}} = 2 \cdot 10^{-5}$  Pa. The evaluable simulation period of  $T = 20$  ms (Sect. 5.3) results in a narrowband frequency bin of  $f_{\text{bin}} = 1/T = 50$  Hz.

As the spatial input of the Fourier transformation, a window of  $12.6 \delta_{99, \text{neck}}$  in the streamwise  $x$ -direction of the TBL is selected ( $k_{\text{bin}} \delta_{99, \text{neck}} = 0.08$ ), starting  $7.8 \delta_{99, \text{neck}}$  before the leading neck edge. In the auxiliary Fig. 7.7, this evaluation window is marked with green squares. The resulting SPL  $k_x - \omega$ -spectra are averaged over all spanwise  $z$ -locations at the wall ( $y = 0$ ), where  $k_x$  is the streamwise wavevector. In Figs. 7.9 and 7.10 the SPL is shown for a simple flat-plate flow and, in comparison, for a TBL with a flush-mounted cavity underneath, respectively. In both figures the inflow conditions are identical (cf. Sect. 5.3). All acoustic fluctuations are located near the Strouhal number axis between the phase velocities  $u_0 \pm c$ , while most fluid-related pressure fluctuations are centered at the convective ridge with a phase velocity below the free stream velocity  $\langle u_c \rangle_z < u_0$  (cf.

## 7. Fluid Dynamical Results and Discussion

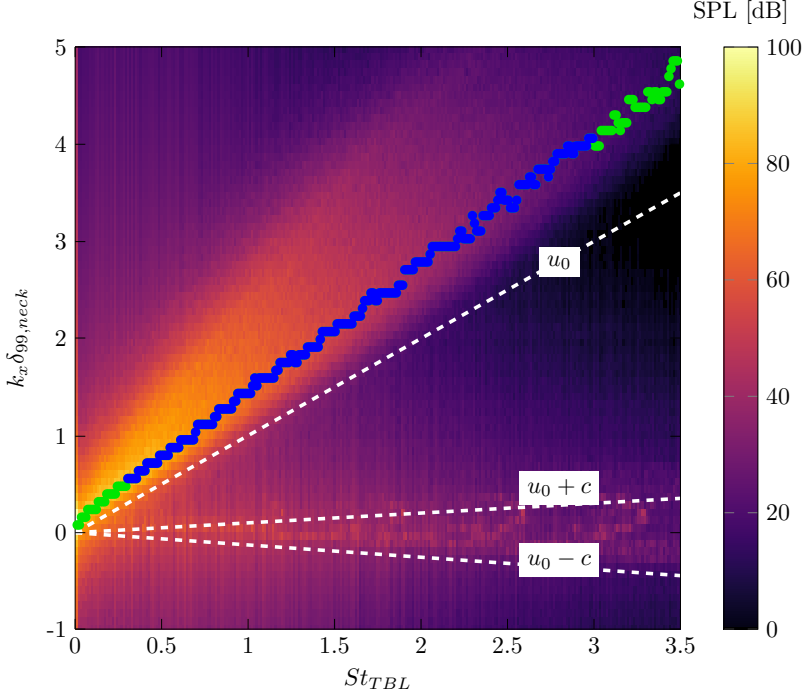


**Figure 7.9:** SPL  $k_x - \omega$ -spectrum (Eq. 7.3) of a turbulent flat plate flow at the wall  $y = 0$  ( $z$ -averaged, streamwise window of  $12.6\delta_{99,neck}$ ). The characteristic phase velocities  $u_0$  and  $u_0 \pm c$  are marked by dashed white lines. The green and blue markers denote the convective ridge. They are introduced later in Sect. 7.4.

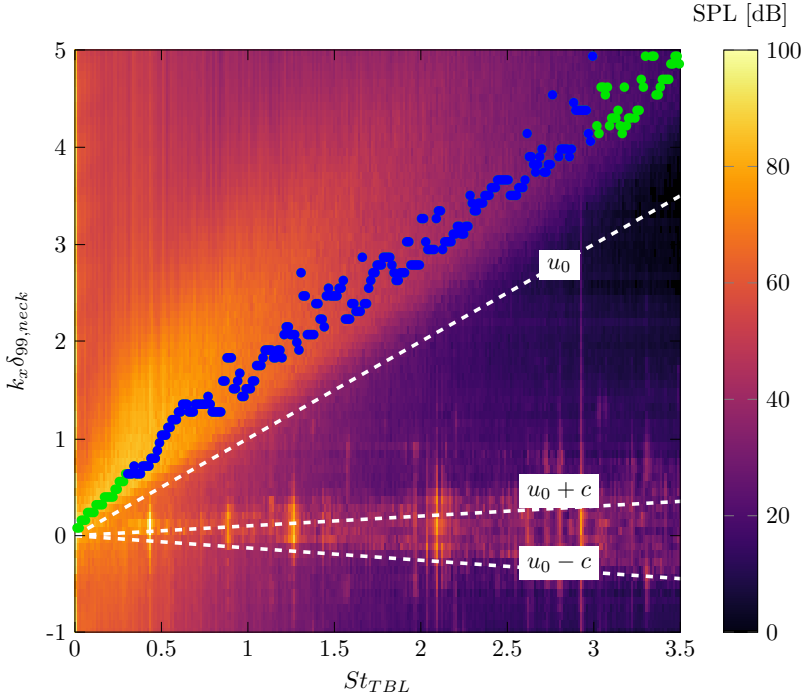


**Figure 7.10:** SPL  $k_x - \omega$ -spectrum (Eq. 7.3) of a turbulent plate flow with a cavity underneath at  $y = 0$  ( $z$ -averaged, streamwise window of  $12.6\delta_{99,neck}$ ). The characteristic phase velocities  $u_0$  and  $u_0 \pm c$  are marked by dashed white lines. The green and blue markers denote the convective ridge. They are introduced later in Sect. 7.4.

## 7. Fluid Dynamical Results and Discussion

---

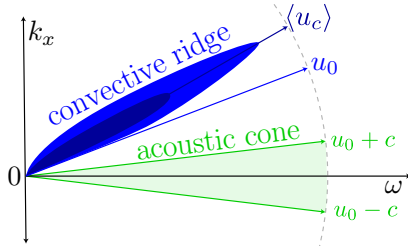


**Figure 7.11:** Characteristic  $k_x - \omega$  - wall pressure spectrum for a subsonic TBL with a convective ridge (in blue) and an acoustic cone (in green).  $\langle u_c \rangle$  is the mean convection velocity.  $u_0$  is the free stream velocity, and  $c$  is the speed of sound.

Eq. C.9). As a reference, the acoustic and the convective domain are exemplified in Fig. 7.11. Inside the convective ridge, most energy is stored, which is reflected by the highest sound pressure levels (see Figs. 7.9, 7.10). Sect. 7.4 discusses the convective ridge further.

The mounting of a cavity inside an initial undisturbed flat plate flow results in a secondary vortex sheet near the wall (cf. Fig. 7.8). This increases the SPL at larger  $k_x$  scales and results in a broader distribution of the convective ridge (greater variance in  $\pm k_x$ ). Beside the convective ridge, the most distinctive modifications induced by the cavity are the acoustic cavity modes, which are characterized by localized spots of maximal SPL near the Strouhal number axis.

### 7.3.2 Goody's Spectral Turbulent Boundary Layer Model of Pressure Fluctuations

In this section, the source term  $\Phi_{TBL}$  of the new model is selected, that most realistically models the natural broadband excitation generated by an undisturbed TBL.

The best fit of the pressure power spectral density at the wall (i.e.,  $y = 0$ ) for a large set of experiments is the model of [Goody \(2004\)](#) as stated in the review paper [Hwang et al. \(2009\)](#). It features the typical Strouhal number scaling  $St_{TBL} = f\delta_{99}/u_0$ , a prefactor  $\rho_w^2\tau_w^4\delta_{99}/u_0$  like the popular [Chase \(1987\)](#) model, exponential growth with  $f^2$  at low frequencies, exponential decay with  $f^{-5}$  at high frequencies, and a wall friction Reynolds number  $Re_\tau$  dependency:

$$\Phi_{TBL}(St_{TBL}) = \frac{\rho_w^2\tau_w^4\delta_{99}/u_0}{\{(2\pi St_{TBL})^{3/4} + 0.5\}^{3.7} + \left\{\frac{1.12\pi St_{TBL}}{(Re_\tau u_\tau/u_0)^{0.57}}\right\}^7} C (2\pi St_{TBL})^2. \quad (7.4)$$

The lower index “ $w$ ” denotes quantities defined at the wall. In [Fig. 7.12](#) a comparison of [Eq. 7.4](#) with the SPL spectrum of a flat plate flow is plotted. To calculate the SPL, [Eq. 7.2](#) is evaluated for two different streamwise top-hat window lengths (see legend of [Fig. 7.12](#)) and then averaged over all  $k_x$ . Goody's model agrees with the DNS (FP case) within an accuracy of  $\pm 2$  dB for Strouhal numbers  $St_{TBL}$  above 0.07. Only the offset constant  $C$  of [Eq. 7.4](#) is increased from 3 to 25 (+9 dB). This is comparable to the increase from 0.15 to 1.7 by [Golliard \(2002, Sec. 3.3.6\)](#) needed to match the Chase model. The first four Strouhal number bins are overestimated by the discrete Fourier transformation, due to the shortness of the time series available (20 ms, see [Sect. 5.3](#)).

## 7. Fluid Dynamical Results and Discussion

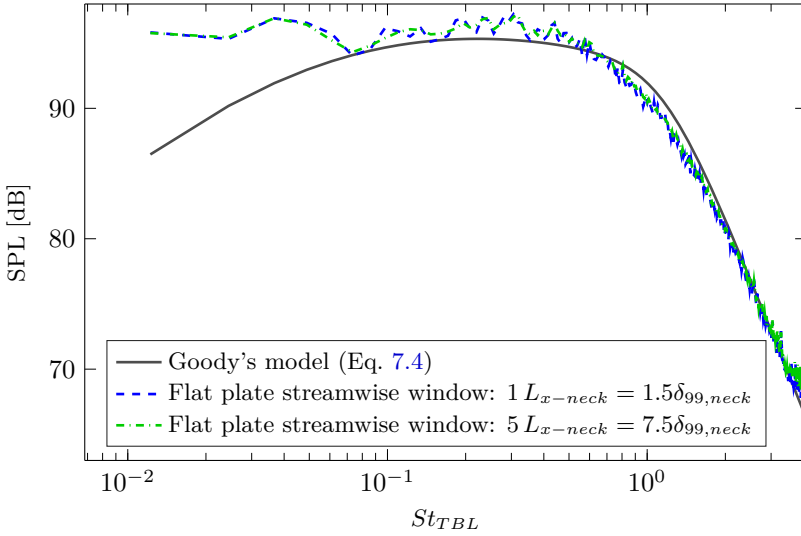


**Figure 7.12:** Broadband pressure fluctuations of a plane TBL at the wall ( $y = 0$ ,  $z$ -averaged). Goody's model is contrasted with the DNS results for different streamwise rectangular windows of the Fourier transformation (Eq. 7.2).

Ideally, to calculate a universal TBL spectrum, the streamwise input length of the Fourier transformation is as long as possible. However, by comparing the two input windows length in Fig. 7.9, no substantial differences occur. Therefore, the universal TBL spectrum by Goody's model can be utilized directly as a source term  $\Phi_{TBL}$  of the Helmholtz resonator model (Eq. 4.28), which acts on the localized surface of the neck only. The source term  $\Phi_{TBL}$  is a pure TBL source. The influence of the neck shear layer is incorporated by the transmission function  $T(Z_{neck})$ , i.e., by Howe's impedance  $Z_{flow}$  (Eq. 4.16).

## 7.4 New Method to set Howe's Mean Velocities

Though the theory of Howe is widely-used, so far,  $u_{\pm}$  of Eq. 4.31 are unclearly defined in a realistic case with a finite shear layer thickness or an incoming turbulent flow. The two parameters are governing Howe's idealized Rayleigh conductivity of an opening, i.e., the impedance  $r_{flow}$  and  $\delta_{flow}$  (Eq. 4.36). Fundamentally,  $u_{\pm}$  are mean flow velocities within Howe's linear perturbation theory (Sect. 4.4). Sometimes  $u_{\pm}$  are also interpreted as a turbulent convection velocity (Peat et al., 2003). Below, a unique method of how to set the values of  $u_+$  and  $\beta = u_-/u_+$  is derived.

This section begins with a definition of the general convection velocity  $u_c$  (Eq. 7.5).  $u_c$  varies depending on the spatial position and frequency. Then, the four-dimensional field  $u_c$  is spectrally and spatially averaged to deduce a scalar value of  $u_+$  (Eq. 7.6), which best represents the velocity of the neck vortex sheet, within Howe's theory.  $\beta$  is set as a constant (Eq. 7.8). In doing so,  $u_+$  and  $\beta$  become universally applicable quantities under realistic conditions.

### 7.4.1 General Turbulent Convection Velocity

The turbulent convection velocity is an ill-defined property, which describes the speed of vortices in general. Depending on the application, many definitions exist (Alamo and Jiménez, 2009; Blake, 1970), both in real and spectral space. The definitions range from broadband or group velocities to narrowband or phase velocities. Sometimes the definitions depend on spatial (wavelength) and temporal (frequency) length-scales, sometimes averages are taken into account.

## 7. Fluid Dynamical Results and Discussion

---

A common, robust definition of the narrowband convection velocity  $u_c$  is the convective ridge maximum of the SPL  $k_x - \omega$ -spectrum (Goldschmidt et al., 1981):

$$u_c(y, z, \omega) \equiv \omega/k_{max}(y, z, \omega) \quad \text{with} \\ 0 \equiv \frac{\partial}{\partial k_x} \text{SPL}(k_x, y, z, \omega) \Big|_{k_x=k_{max}}. \quad (7.5)$$

In Figs. 7.9 and 7.10 blue and green bullets mark the maxima of the convective ridge determined by Eq. 7.5. Thereby the determination of the maximum  $k_{max}$  excludes the acoustic range (defined by  $u_0 + c$  and  $u_0 - c$ ) because cavity resonances locally exceed the convective ridge (cf. Fig. 7.10). The calculation of a narrowband  $k_x - \omega$ -spectrum requires a resolution which fully resolves the location of the convective ridge in time and space (like the DNS of Stein et al. (2018) or the experiment by Arguillat et al. (2010)). Measurements which are based on only a few microphones are incorrect, due to the known frequency and scale dependencies (i.e., streamwise probe separation) of the convection velocity (Gloerfelt and Berland, 2013; Kim and Hussain, 1993). Integral definitions of the convection velocity like in Alamo and Jiménez (2009) are not recommended in the present HR case of a distorted TBL since the convective ridge does not decay rapidly at high  $|k_x|$  or  $\omega$ . This implies that the integral definition depends on the integration limits (of  $k_x$  or  $\omega$ ), which in turn depend on the data sampling rate.

In the interest of a clearer presentation, the maxima of Fig. 7.9 are replotted in Fig. 7.13. At around  $St_{TBL} \approx \omega\delta^*/u_0 \approx 0.3$  the convection velocity over the Strouhal number exhibits a typical maximal curvature in accordance with Gloerfelt and Berland (2013); Viazzo et al. (2001) and Hu et al. (2016), where  $\delta^*$  is the displacement thickness. Above this maximal curvature, the convection velocity

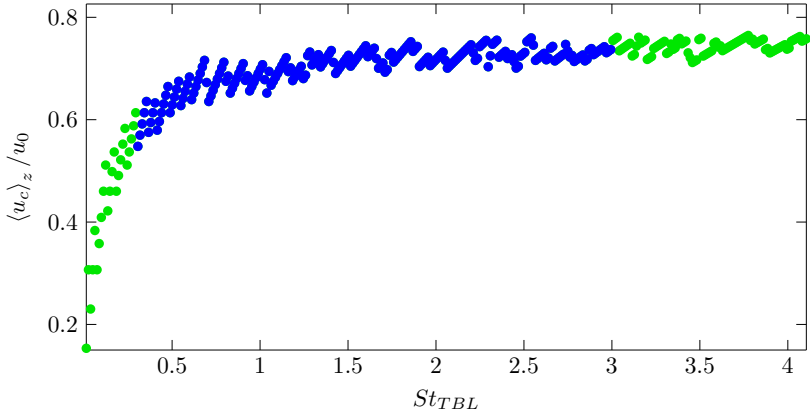


**Figure 7.13:** Convection velocity of a turbulent flat plate flow calculated by Eq. 7.5 ( $z$ -averaged, streamwise window of  $12.6\delta_{99,neck}$  (see Fig. 7.7),  $y = 0$ , same case as Fig. 7.9). Above the typical maximal curvature at  $\omega\delta^*/u_0 \approx 0.3$  the convection velocity is approximately constant. The mean convection velocity is defined as average from  $\omega\delta^*/u_0 = 0.3$  to  $\omega\delta^*/u_0 = 3$  (denoted by blue bullets).

remains approximately constant. Frequency averaging the convection velocity between  $\omega\delta^*/u_0 = 0.3$  and  $\omega\delta^*/u_0 = 3$  leads to a mean convection velocity of  $\langle u_c \rangle_{z,St} = 0.68$ . This value is valid on the wall ( $y = 0$ ).

#### 7.4.2 Specification of Howe's Mean Velocity $u_+$ using the Turbulent Convection Velocity

Based on the characteristic Strouhal number dependence of the general convection velocity, the frequency averaging of  $\langle u_c \rangle_{z,St}$  between  $\omega\delta^*/u_0 = 0.3$  and  $\omega\delta^*/u_0 = 3$  is the first step to define the value of  $u_+$  spectrally. Just the upper bound is arbitrary. At least a shift of the upper bound has a marginal influence on the convection velocity

## 7. Fluid Dynamical Results and Discussion

---

because  $\langle u_c \rangle_z$  is roughly constant around  $\omega\delta^*/u_0 = 3$  (see Fig. 7.13) and decays only slowly at high Strouhal numbers far beyond  $\omega\delta^*/u_0 = 3$ .

To spatially specify the mean velocity  $u_+$ , too, now the influence of the streamwise DFT input length (cf. Eq. 7.2) is analyzed. In Fig. 7.14 a whole set of frequency and  $z$ -averaged convection velocity profiles  $\langle u_c \rangle_{St,z}(y)$  with different streamwise DFT window lengths  $L_{x-DFT}$  is depicted for the FP case (centered around  $x = 0.75\delta_{99,neck} = 0.5L_{x-neck}$ , see Fig. 7.4). Outside the viscous wall region ( $y/\delta_{99,neck} > 0.1$ ), the convection velocity  $\langle u_c \rangle_{St,z}$  increases with the wall distance  $y$ . Remarkably,  $\langle u_c \rangle_{St,z}$  even exceeds  $\langle u_x \rangle_z$  near the wall in the viscous sublayer. Possible explanations are that  $u_c$  is a phase velocity (see Eq. 7.5) and not a group velocity or the fact that far out whirls leave a footprint of pressure near the wall. In a study of [Alamo and Jiménez \(2009\)](#), the same behavior appears.

Typically, larger TBL streaks occur further away from the no-slip wall, in faster moving fluid regions. Consequently, the convection velocity increases with  $L_{x-DFT}$  (cf. Eq. 7.2). An asymptotic value is reached as soon as the streamwise signal window envelopes the largest streaks of the TBL. In Fig. 7.14 an asymptotic value of the convection velocity  $\langle u_c \rangle_{St,z}/u_0$  between 0.68 (at  $y = 0$ ) and 0.78 (at  $y = 0.44\delta_{99,neck}$ ) is reached, approximately effective from  $L_{x-DFT} > 6.4L_{x-neck}$ . This is consistent with the results of a tripped TBL simulation by [Gloerfelt and Berland \(2013\)](#). In their spectral evaluation, they introduce a streamwise separation distance  $\xi_1$  corresponding to the distance between two virtual microphones, to determine the convection velocity. Their observation is quantitatively the same: The larger the separation  $\xi_1$ , the more high-speed pressure sources dominate. In their case an asymptotic value of  $u_c = 0.75$  (at  $y = 0$ ) is reached for a minimal separation distance of  $\xi_1 > 2\delta_{99}$ . Since [Gloerfelt and Berland \(2013\)](#) just consider one specific separation distance  $\xi_1$  in contrast to all

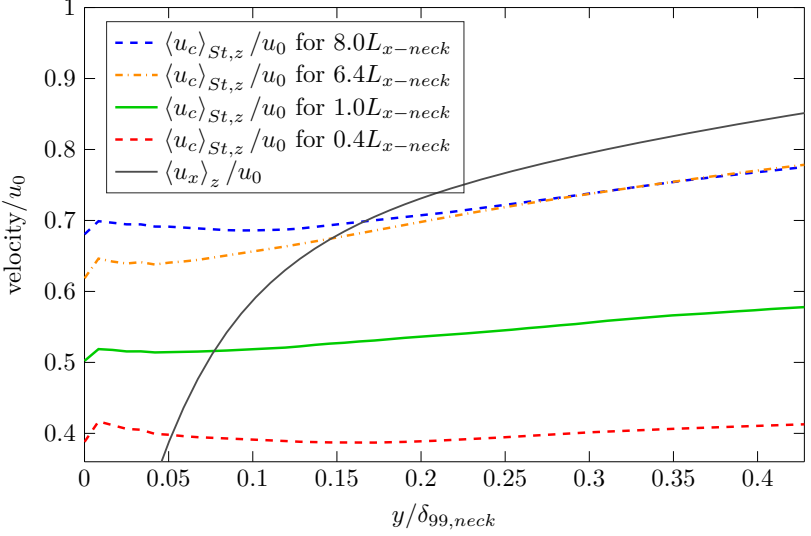


**Figure 7.14:**  $\langle u_c \rangle_{St,z}$  averaged over  $St = \omega \delta^* / u_0 \in [0.3, 3.0]$  as a function of the non-dimensional wall distance. A whole family of curves for different streamwise DFT windows is plotted in various colors for the FP case. All windows are centered around  $x = 0.5L_{x-neck}$  (cf. Fig. 7.4). As a reference, the mean velocity profile from Fig. 7.1 is depicted in black.

the separation distances implicitly included in the DFT window used here, a deviation of the asymptotic  $u_c$  value is expected.

For the definition of  $u_+$ , only the structures which fit into the neck are of interest. Hence, in the case of a TBL with a flush-mounted cavity, the natural window length to calculate the SPL  $k_x - \omega$ -spectrum is the neck dimension. Only inside the neck surface  $S_{neck}$  the vortex sheet is modeled by Howe (Eq. 4.30). Hence, the streamwise DFT window is set equal to the streamwise neck length:  $L_{x-DFT} = L_{x-neck}$ . In the following, the notation  $\langle u_c \rangle$  implies averaging over  $\omega \delta^* / u_0 \in [0.3, 3.0]$  and  $S_{neck}$ .

## 7. Fluid Dynamical Results and Discussion

---

So far, the convection velocity  $\langle u_c \rangle$ , which is averaged over  $x$ ,  $z$ , and  $\omega$ , still depends on  $y$ . In the following, this  $y$  dependency of  $\langle u_c \rangle$  is examined, before the characteristic height  $y_+$  is selected, which ultimately defines the value of  $u_+ = \langle u_c \rangle (y = y_+)$ .

Fig. 7.15 contrasts  $\langle u_c \rangle (y)$  of the FP and the HR case with the mean velocity  $\langle u_x \rangle (y)$ . The mean velocity  $\langle u_x \rangle$  of the shear layer at the opening (cf. Fig. 7.8) is greater than the plain TBL profile near the wall. Only for  $y > 0.1\delta_{99,neck}$  both cases, with and without mounted cavity, coincide (consistent with the analytical Van-Driest profile of Fig. 7.1). The green  $\langle u_c \rangle$  curve of the FP case is identical to the green curve of Fig. 7.14 ( $1.0L_{x-neck}$ ). By comparing the case with an opening (HR) to the undisturbed TBL (FP), an even lower  $\langle u_c \rangle$  is found, despite a higher  $\langle u_x \rangle$ . A possible explanation for this is that the newly formed eddies of the upstream edge have to be accelerated first so that the average (eddy) convection velocity drops.

The height of the second inflection point of the mean velocity profile is chosen (first identified in Fig. 7.3), to define the value of  $u_+ = \langle u_c \rangle (y = y_+)$  by a characteristic  $y_+$ . Thus, the value of  $u_+$  is now ultimately defined as

$$u_+ \equiv \langle u_c \rangle_{St, S_{neck}} (y = y_{\text{central inflection pt.}}). \quad (7.6)$$

$u_c$  is determined by Eq. 7.5 and averaged over  $S_{neck}$  and  $\omega\delta^*/u_0 \in [0.3, 3.0]$ .

The definition of  $y_+ = y_{\text{central inflection pt.}}$  (Eq. 7.6) as the characteristic location of the neck vortex sheet has the following reasons: Following the discussion of Fig. 7.8 the deviation (change of curvature) of Howe's vortex sheet from the underlying standard shear layer profile is flanked on both sides by the outer inflection points. Hence the middle inflection point (located between the two outer ones) represents the

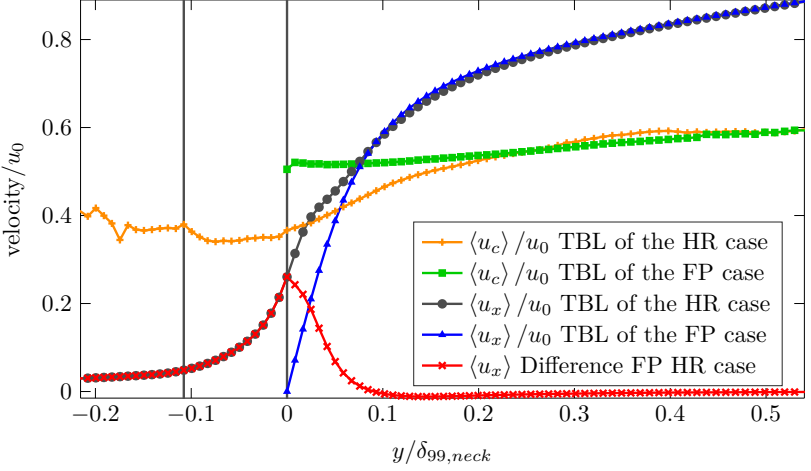


**Figure 7.15:** Velocity profiles plotted over  $y$  of the FP (plane TBL) and the HR case (TBL with a cavity underneath). The notation  $\langle \bullet \rangle$  denotes an average over  $\omega\delta^*/u_0 \in [0.3, 3.0]$  and  $x, z \in S_{neck}$ . The vertical black lines indicate the neck location between the cavity ceiling at  $y = -0.11\delta_{99,neck}$  and the flat plate surface at  $y = 0$ .

central position of the neck vortex sheet (cf. Fig. 7.3). Furthermore, this stable<sup>1</sup> inflection point has a constant height  $y$  above the whole neck opening.

In the present case, the point of inflection is  $y_+^\dagger = 6 \pm 1.5$ , which results according to Fig. 7.15 in

$$u_+/u_0 = 0.39 \pm 0.03. \quad (7.7)$$

Here,  $u_+$  directly scales with  $u_0$ . This value is in agreement with Golliard's experiments carried out at various Mach numbers  $M_0 \in$

<sup>1</sup>Its characteristic change of curvature does not meet Fjørtoft's instability criterion.

## 7. Fluid Dynamical Results and Discussion

---

[0.01, 0.14], (see the following Figs. 8.1, 8.3 and 8.4). A new method to set a  $u_+$  value for Howe's theory in general and in particular for Eq. 4.31 is set up.

It is worth noting that just because of matching values  $u_+$  and  $\langle u_c \rangle_{St, S_{neck}}$  cannot be considered physically equally. The reason is as follows:  $u_+$  is a mean value (background flow). In contrast,  $u_c$  describes the convection of dominant turbulent structures (convective ridge) as a phase velocity (Eq. 7.5). Within the framework of Howe's linear perturbation theory (Sect. 4.4),  $u_+$  should be physically considered as mean flow  $\langle u_x \rangle_{S_{neck}}$ .  $u_c$  often can<sup>2</sup> be related to the phase velocity  $u_{ph}$  (Eq. 4.32) of the KH waves (Towne et al., 2017). As a consequence, the alternative definition  $u_+ \equiv \langle u_x \rangle_{S_{neck}}$  ( $y = y_{\text{central inflection pt.}}$ ) instead of Eq. 7.6 suggest itself. The resulting  $u_+/u_0 = 0.42$  (see Fig. 7.15) is similar to the previous  $u_+/u_0$  value of 0.39 of the mean convection velocity  $\langle u_c \rangle_{St, S_{neck}}$  (Eq. 7.7).

However, because 0.39 leads to slightly better HR model predictions later, only the first definition of Eq. 7.6 is used to calculate a  $u_+$  value in the following. An advantage of the turbulent convection velocity definition (Eq. 7.6) is its frequency dependence (Fig. 7.13), allowing to directly extend the spectral HR model also with a frequency dependent  $u_+$  value.

---

<sup>2</sup>In principle the SPL of Eq. 7.5 contains possible nonlinear effects too. Thus,  $u_c$ , as defined here, takes into account not only linear perturbations.

### 7.4.3 Specification of Howe's Velocity Ratio

$$\beta = u_-/u_+$$

As the most obvious approach, corresponding to the original interpretation of  $u_{\pm}$  as mean flow properties,  $\beta = u_-/u_+$  is assumed to be proportional to the mean velocities  $\langle u_x \rangle$  above and below the opening. In the following, it is clarified, that this choice is incapable of describing a three-dimensional opening with an extended vortex sheet thickness. Subsequently, an alternative definition is suggested.

In the present case of one-sided flow, the obvious (but discarded) approach results in the hypothetical relation  $\beta = \langle u_x \rangle (y = \delta_-^*) / \langle u_x \rangle (y = \delta_+^*) \propto 1/u_0$ , where  $\delta_{\pm}^*$  represent a measure of the shear layer thickness above and below the opening. Since  $\delta_{\pm}^*$  typically grows linearly in streamwise  $x$ -direction Pope (2000, Sect. 5.4.2),  $\beta$  is roughly  $x$ -independent. Here  $\delta_+^*$  is approximated as the location, where the difference between the shear layer profile and the plane TBL profile falls below  $0.1u_0$ . Furthermore,  $\delta_-^* = \delta_+^*$  is set. In the HR case with  $M_0 = 0.11$  the ratio is  $\beta = 8\text{m/s}/u_0 = 0.21$ . However, experiments do not reflect this  $u_0$  dependency. The best fit of Howe's theory with Golliard's experiments is achieved with a constant

$$\beta \equiv 0.21 \tag{7.8}$$

relation, which is valid for different  $M_0 \in [0.01, 0.14]$  (see Figs. 8.3, 8.4, discussed later). Howe (1998, Sect. 5.3.6) gives a possible explanation for this: Due to the finite thickness  $L_{y-neck}$  of the opening (not infinitely thin as theoretically assumed before), the conductivity of an opening in two-sided flow actually is similar to one-sided flow (twice). Hence, an effectively smaller  $\beta$  can account for a finite neck thickness  $L_{y-neck}$ . In the present case of one-sided flow, this means: If  $u_0$  is decreased,

## 7. Fluid Dynamical Results and Discussion

---

the  $\beta$  ratio does not necessarily decrease but instead remains constant to account for a finite neck thickness  $L_{y-neck}$ .

The definition of a constant  $\beta$  for Eq. 4.31 remains to be further investigated, due to an unclear influence of the thickness  $L_{y-neck}$ .

In the next Chap. 8, the  $u_+$  and the  $\beta$  definition are inserted in the Helmholtz resonator model. The validity of the new definitions is then implicitly shown by demonstrating the Helmholtz resonator model validity range. Sect. 8.2 continues discussing the unclear dependency  $\beta(L_{y-neck})$ .

# Acoustical Results and Discussion

To validate the new convection velocity definitions, individually, the impedance element  $Z_{flow}$  (Eq. 4.36) of the flow-acoustic interaction, and following, the SPL predictions of the complete Helmholtz resonator model are compared to the DNS results and experimental findings by Elder et al. (1982); Golliard (2002) and Kooijman et al. (2008). A validity range for Mach numbers  $M_0 \in [0.01, 0.14]$  and for Helmholtz numbers  $He_{cavity} \in [0, 0.63]$  is demonstrated. The suitability of the model to incorporate additional effects as the boundary layer thickness is discussed, too. Finally, dominant cavity modes and KH modes of the neck opening are identified using the new Helmholtz resonator model. The predicted modes are reviewed through alternative models and by employing a DMD of a DNS time series.

## 8.1 Helmholtz Resonator Model with New Parameters

In this section, the newly defined parameters  $u_+$  and  $\beta$  (Eq. 7.6 and Eq. 7.8) are inserted into the Helmholtz resonator model. For the direct application by an industrial user, all elements, and parameters needed to use new model are summarized below.

## 8. Acoustical Results and Discussion

---

Starting with the top level Eq. 4.28 of the power spectral density, first the Helmholtz resonator transmission function Eq. 4.22 and the source term of broadband TBL noise (Goody's Eq. 7.4) are explicitly written. All previously unknown dependencies on various impedance functions are now expressed just in dependency of characteristic geometry dimensions of the neck and the cavity, the crucial mean velocities  $u_+$  and  $\beta$  (colored red in Eq. 8.2), the speed of sound  $c_0$ , the frequency  $\omega$  (implies the wavenumber  $k$ , too), and the TBL quantities  $\delta_{99,neck}$ ,  $u_0$ ,  $u_\tau$ ,  $\rho_w$  and,  $\nu$  (see Eq. 7.4):

$$\Phi_{bot} = T(Z_{neck}, S_{neck}, S_{cavity}, k L_{y-cavity}) \Phi_{TBL}(\omega, \delta_{99,neck}, u_0, u_\tau, \rho_w, \nu). \quad (8.1)$$

Thereby, the neck impedance (Eq. 4.18) is given in detail by

$$\begin{aligned} Z_{neck} = & Z_{jump}(S_{neck}, S_{cavity}) \\ & + Z_{flow}(L_{x-neck}, \frac{\omega L_{x-neck}}{u_+}, \frac{u_+}{c_0}, \beta) \\ & + Z_{rad}(L_{x-neck}, L_{z-neck}), \end{aligned} \quad (8.2)$$

where the individual resistance and length corrections originate as follows:  $r_{jump}$  and  $r_{rad}$  of Eq. 4.12 and Eq. 4.14, respectively,  $\delta_{jump}$  and  $\delta_{rad}$  of Eq. 4.35,  $r_{flow}$  and  $\delta_{flow}$  of Eq. 4.36.

Generally, the new  $u_+$  is determined as follows: First, the  $k_x - \omega$ -spectrum is calculated (Eq. 7.2) at the constant height of the central inflection point of the shear layer ( $y = y_{\text{central inflection pt.}}$ ). Second, the convection velocity  $u_c$  is derived as the phase velocity  $\omega/k_x$  of the pressure  $k_x - \omega$ -spectrum at the convective ridge maximum (Eq. 7.5). Third, averaging  $u_c$  over all  $S_{neck}$  and  $St_{TBL} \in [0.3, 3.0]$  provides  $u_+$  (Eq. 7.6).

Specifically, within the validity ranges stated in Sects. 8.2.4, 8.3 Eq. 7.7 directly provides an  $u_+$  value, depending on the free stream velocity  $u_0$ .

$\beta$  is defined as a constant value of 0.21 (Eq. 7.8).

## 8.2 Model Interpretation, Validation, and Validity Range

Parts of this section have been published in **Stein and Sesterhenn (2018)**, others in **Stein and Sesterhenn (2019a)**.

In this section, the Helmholtz resonator model with its new parameters is validated by comparison with an experiment and the DNS: First, the comparison is started with the most crucial element  $Z_{flow}(u_+, \beta)$ , separately (Sect. 8.2.1). Second, the physical meaning of the governing model parameters  $u_+$  and  $\beta$  is newly specified (Sect. 8.2.2). Third, the complete Helmholtz resonator model is compared with the DNS results (Sect. 8.2.3). Fourth, the validity range of the new model is demonstrated (Sect. 8.2.4).

### 8.2.1 Validation of the Flow-Acoustic Interaction Impedance

Fig. 8.1 shows the impedance  $Z_{flow}/Y_{neck} = r_{flow} + ik\delta_{flow}$  modeled by Eq. 4.36 (with  $u_+$  and  $\beta$ ) and measured by **Golliard (2002)**. Thereby the experimental curves are averaged over different conditions such as  $M_0 \in [0.11, 0.12]$  and ratios of  $\delta_{99,neck}/L_{x-neck} \in [0.7, 5]$ . Even though **Howe's** theoretical model assumes an infinite thin vortex sheet, the experimental results are in accordance with the model predictions:

## 8. Acoustical Results and Discussion

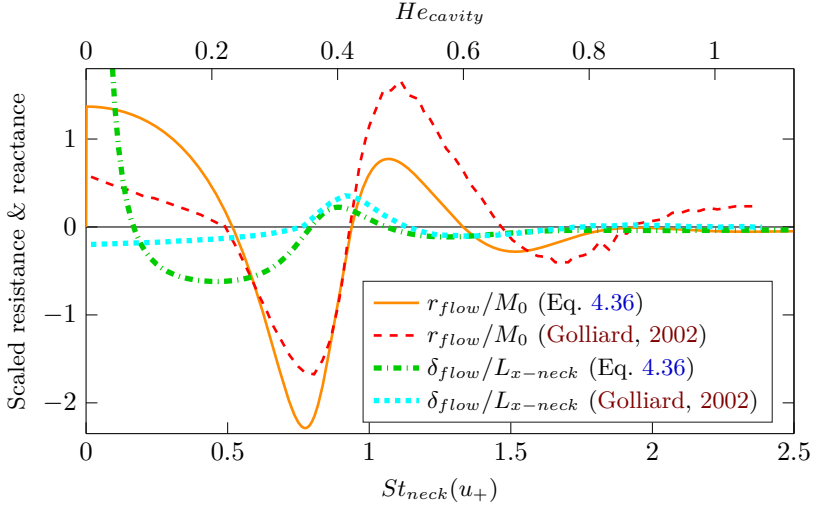


**Figure 8.1:** Validation of Howe’s impedance model Eq. 4.36 vs. experiment for  $u_+/u_0 = 0.39$  and  $\beta = 0.21$  (see Sect. 7.4). The resistance  $r_{flow}$  and the reactance  $\delta_{flow}$  are rescaled with the Mach number  $M_0$  and the streamwise neck length  $L_{x-neck}$ , respectively.

especially the Strouhal number scaling, i.e., the extrema positions and the zero-crossings match. At the zero-flow limit ( $St_{neck}$  at infinity) the impedance becomes zero, as expected:  $\lim_{St_{neck} \rightarrow \infty} Z_{flow} = 0$ . The sign of  $r_{flow}$  determines the direction of the energy transfer between the KH waves of the neck and the passing sound waves. The acoustic damping at low Strouhal numbers  $St_{neck} < 0.5$ , as well as the acoustic excitation between  $St_{neck} \in [0.5, 1]$ , is typical for all kind of neck geometries like circles, rectangles or triangles (Grace et al., 1998). The coupling of KH waves and acoustic waves can be viewed similarly to the fluid-resonant mechanism (Sect. 1.2). The difference is that instead of resonant cavity modes, the tunneling of external sound waves through the neck vortex sheet is considered (without cavity).

---

## 8.2 Model Interpretation, Validation, and Validity Range

The impact of  $u_+$  and  $\beta$  on  $Z_{flow}$  is as follows:  $u_+$  determines the central frequency scaling, which relates the Strouhal number  $St_{neck}$  to the frequency  $f$  (Eq. 4.31) or the Helmholtz number  $He_{cavity}$ . If  $u_+$  is modified, the entire Fig. 8.1 remains unchanged in terms of  $St_{neck}$  with the sole exception of the upper  $x$ -axis of  $He_{cavity}$ . Such  $Z_{flow}$  plotted over  $St_{neck}$  (as in Fig. 8.1) allows a universal representation.

$\beta$  tunes the amplitude of the complex-valued impedance  $Z_{flow}$  depending on the Strouhal number. If  $\beta$  is increased from zero to one, constantly new positive and negative bulges of  $r_{flow}$  and  $\delta_{flow}$  arise at higher and higher Strouhal numbers (cf. Howe, 1998, Fig. 5.3.8). In doing so, the new bulges have a slowly, shrinking amplitude with higher Strouhal number, while the amplitude and position of the low-frequency bulges remain almost the same. Here, the definition of  $\beta = 0.21$  by Eq. 7.8 overestimates low Strouhal number and underestimates high Strouhal number amplitudes, as shown in Fig. 8.1. This discrepancy is an indication that the single parameter  $\beta$  of Howe's theory is not sufficient to accurately describe low and high Strouhal number amplitudes simultaneously.

### 8.2.2 A New View on the Model Parameters $u_+$ , $\beta$

In conclusion, based on this just debated characteristic changes of  $Z_{flow}$  and based on Sect. 7.4, a reinterpretation of  $u_+$  and  $\beta$  suggests itself.  $u_+$  can be considered as the central vortex sheet velocity, i.e., the mean velocity at the central inflection point of the neck shear layer (defined by Eq. 7.6). Hence  $u_+$  is a central quantity of the vortex sheet, rather than a velocity located above the vortex sheet as suggested by the lower “+” index. In the following, the plus sign is kept to remind of its origin within Howe's theory.

## 8. Acoustical Results and Discussion

---

Instead of understanding  $\beta$  only as a velocity ratio  $u_-/u_+$  (Eq. 4.31)  $\beta$  should be more universally regarded as a measure of the shear layer growth within the opening. Other than the mean velocity difference below and above the vortex sheet  $\langle u_x \rangle (y_{\pm})$  (original interpretation), the growth of the shear layer thickness is equally affected by the opening thickness  $L_{y-neck}$  and the relative, incoming boundary layer thickness  $\vartheta = \delta_{99}/L_{x-neck}$ . The motivation to regard  $\beta$  as a general measure of the shear layer growth is as follows (see also discussion in Sect. 4.4): In the limit  $\beta = 1$ ,  $Z_{flow}$  has contributions (bulges) over the whole frequency range (and a purely imaginary-valued KH wave exponent of Eq. 4.30). If high frequencies have a more significant influence, small structures are more important, which indicates a thin vortex sheet and a minimal shear layer growth. By contrast, in the limit  $\beta = 0$ ,  $Z_{flow}$  has only low-frequency components, large structures are dominant, which requires a rapid shear layer growth within the streamwise opening length. As noted before (at the end of Sect. 7.4.3), Howe argues that the conductivity of an opening in two-sided flow, in practice is actually similar to the case of one-sided flow, because of the finite  $L_{y-neck}$  thickness. In other words, the recirculation area at the upstream side of the opening enhances the shear layer growth and therefore can be represented by an effectively smaller  $\beta$ . The ratio  $\vartheta = \delta_{99}/L_{x-neck}$  is inversely proportional to the fraction of the TBL profile, which penetrates the opening (see Sect. 8.3). Hence, a smaller relative boundary layer thickness  $\vartheta$  amplifies the shear layer growth and such increases  $\beta$ .

To sum up,  $\beta$  is (at least) a function of  $\langle u_x \rangle (y_{\pm})$ ,  $L_{y-neck}$ , and  $\vartheta$ . It remains to prove and explicitly quantify, these theory-based predictions about the qualitative behavior of  $\beta$ . Regarding  $u_+$ , its dependency on  $\langle u_c \rangle (y_+)$  or alternative on  $\langle u_x \rangle (y_+)$  is already discussed at the end of Sect. 7.4.2. In Sect. 8.3 the impact of  $\vartheta$  on  $u_+$  is analyzed.

### 8.2.3 Validation of the Helmholtz Resonator Model

Fig. 8.2 presents the application of the complete Helmholtz resonator model (Eq. 8.1) to the example problem (a) of Fig. 4.3. Here the SPL narrowband spectrum at the bottom of the cavity is shown. At the bottom, purely acoustical pressure fluctuations dominate (see discussion of Fig. 7.8). This has the advantage that without a Helmholtz decomposition the power spectral density  $\Phi_{bot}$  of the pressure is directly related to the SPL (Eq. 7.3). As a comparison, the  $xz$ -averaged SPL of the DNS and the experimental SPL of Golliard (2002, cavity C1, TBL B,  $L_{x-neck} = 14\text{mm}$ ,  $\delta_{99} = 10.9\text{mm}$ ) are plotted. Also, the model predictions of an alternative empirical model are taken from Golliard (2002, Sect. 5.3.1).

The predicted extrema conditions of the Helmholtz resonator model are matching the experimental and the DNS results. Violet circles denote the zeros of the *length* term  $\Lambda_\delta$  (Eq. 4.23): The first SPL peak of Fig. 8.2 at  $He_{cavity} = 0.13$  is the Helmholtz base mode. The second peak at  $He_{cavity} = 0.53$  is the first vertical  $y$ -cavity mode. Below  $He_{cavity} = 0.63$  the SPL of the new model, the experiment, and the DNS maximally deviates by  $\pm 7\text{dB}$ . Higher  $x$ - or  $z$ -cavity modes begin at  $He_{cavity} = L_{y-cavity}/2L_{x-cavity} = 0.72$ . Hence, the deviation of the model at  $He_{cavity} = 0.72$  is expected. Furthermore, since  $L_{x-cavity} = L_{z-cavity}$  all  $x$ - and  $z$ -cavity resonances even coincide, implicating a doubling of pressure. By virtue of simplicity, these higher transverse  $x$ - or  $z$ -modes are not included in the model because they are beyond the typical range of operation. Red stars denote the zeros of the *energy transfer* term  $\Delta_r$  (Eq. 4.24). Here the interchange between acoustical and fluid energy is balanced over the time average. Since the ratio  $S_{ratio} = S_{neck}/S_{cavity} = 0.14$  of Eq. 4.22 is small, they hardly contribute to the overall SPL at the cavity bottom. Only in the DNS

## 8. Acoustical Results and Discussion

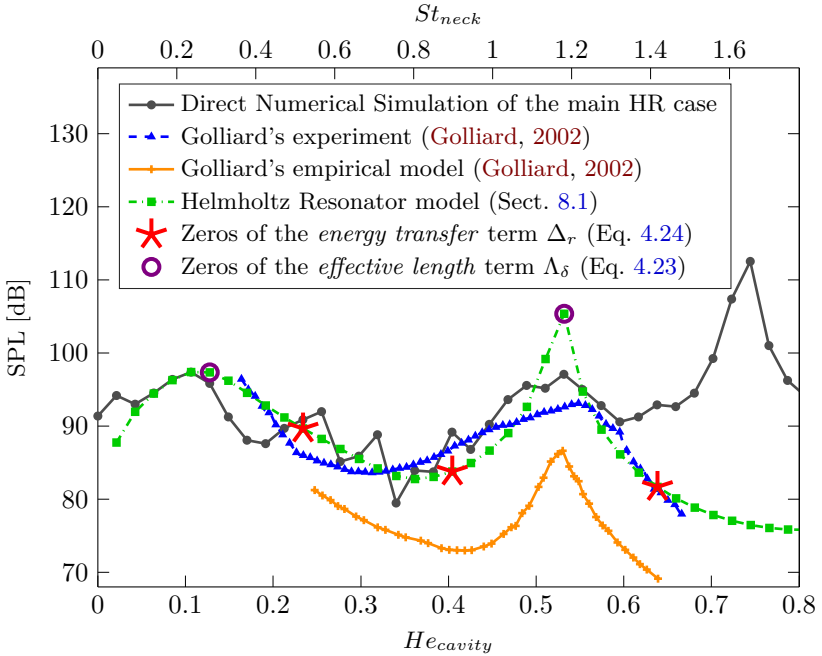


**Figure 8.2:** Narrowband SPL spectrum ( $\Delta H_{cavity} = 0.02 \leftrightarrow f_{bin} = 50$  Hz) centered at the bottom of the Helmholtz cavity (setup (a) of Fig. 4.3). For comparison, the measured SPL and the empirical model of Golliard (2002) are shown.

results, small local increases are visible at zero resistance. However, this might be up to the noise due to the limited time series available of 20ms (restriction of DNS resources, setup see in Sect. 5.3).

Golliard's empirical model is only plotted within its Helmholtz numbers validity range. Thereby, the Helmholtz number prediction of the first vertical  $y$ -cavity mode is in agreement with the other curves; however, a constant offset of about  $-10$ dB is apparent.

### 8.2.4 Validity Range of the Model

During the derivation of the model, the focus is on universal definitions of the governing parameters. However, only one single DNS run with  $M_0 = 0.112$  provided the reference data (see HR case in Sect. 5.3). To demonstrate its universal validity, the model is evaluated for the whole velocity range  $M_0 \in [0.01, 0.14]$  measured by Golliard (2002). In Figs. 8.3 and 8.4 the SPL model spectra are compared with the experimental measurements, respectively. To a great extent, both figures are in agreement at all velocities.

The zeros of the *effective length*  $\Lambda_\delta$  (Eq. 4.23, dotted black mainly vertical lines) are predominantly geometry dependent so that the position of the Helmholtz base mode ( $He_{cavity} = 0.13$ ) and the first vertical  $y$ -cavity mode ( $He_{cavity} = 0.53$ ) are almost velocity independent. In contrast, the zeros of the *energy transfer*  $\Delta_r$  (Eq. 4.24, dashed white diagonal lines), which correspond to a balanced energy interchange between the acoustical and the KH waves, scale as expected with the free stream velocity  $u_0$ . The overlap of both resonance conditions leads to a strong nonlinear interaction of the vortex-sheet with the cavity modes. Qualitatively similar behavior of these resonance conditions is also observed for example by Yang et al. (2009)'s experimental study of deep, open cavities (without a neck).

The new Helmholtz resonator model successfully predicts where the occurring physical phenomena are coupled: the Helmholtz base mode strongly couples with the KH waves of the neck between  $M_0 = 0.02$  and  $M_0 = 0.06$  resulting in a SPL beyond 120dB (see Fig. 8.3). It is known that such high sound pressure levels cause a scattering to higher harmonics (Förner et al., 2017). Experimentally these higher harmonics are visible in Fig. 8.4 at  $He_{cavity} = [1.4, 2.8, 4.2, 5.6]$ . The model

## 8. Acoustical Results and Discussion

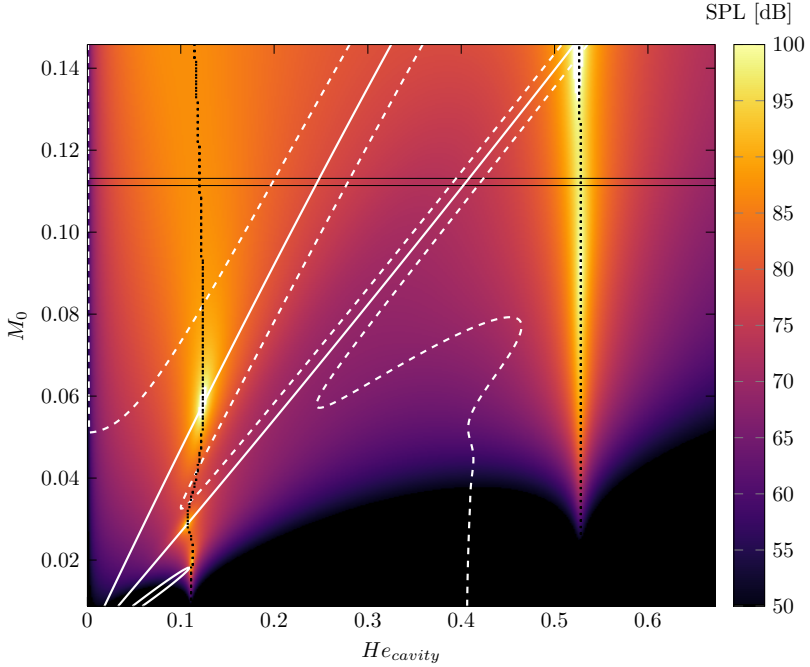


**Figure 8.3:** SPL spectrum ( $\Delta He_{cavity} = 0.002 \leftrightarrow f_{bin} = 4,3 \text{ Hz}$ ) predicted by the Helmholtz resonator model Eq. 4.28 for the cavity setup of Fig. 4.3 (a). The dotted black vertical lines mark the resonance conditions  $\cot(kl) = S_{ratio}(\delta_{jump} + \delta_{flow} + \delta_{rad})$ , i.e., the *length* term (Eq. 4.23). The white lines mark  $r_{flow} + r_{rad} = 0$  and the dashed white lines mark  $|r_{flow} + r_{rad}| = 0.07$ . So both white lines are related to the *energy transfer* term (Eq. 4.24). The black horizontal double line corresponds to the DNS case with  $M_0 = 0.112$  (see Fig. 8.2).

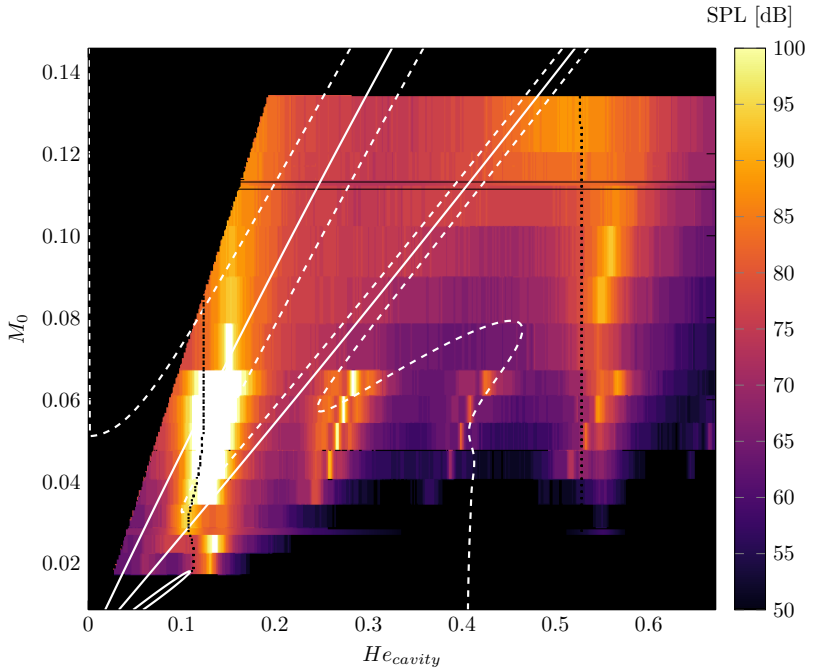


**Figure 8.4:** Measured SPL spectrum extracted from Golliard (2002) for the same conditions as in Fig. 8.3 (effective  $\Delta H e_{cavity} = 0.002 \leftrightarrow f_{bin} = 4,3$  Hz, original  $f_{bin,exp} = 1$  Hz). The black and white lines are a copy from Fig. 8.3. Golliard discarded the upper left black triangle due to wind tunnel noise.

predicts the initial resonance condition at  $He_{cavity} \in [0.11, 0.13]$  and at  $M_0 \in [0.02, 0.06]$  but does not predict scattered higher harmonics.

The right prediction of the resonance conditions by  $\Lambda_\delta(u_+, \beta)$  and  $\Delta_r(u_+, \beta)$  for the Helmholtz numbers  $He_{cavity} \in [0, 0.63]$  and for the Mach numbers  $M_0 \in [0.01, 0.14]$  also verifies the new  $u_+$  (generally Eq. 7.6, specifically Eq. 7.7) and  $\beta$  (Eq. 7.8) definitions, within these ranges.

### 8.3 Influence of the Boundary Layer Thickness on $u_+$

Beside  $u_0$ , the detailed influence of the incoming TBL is not directly included in the model transfer function (Eq. 4.28), but indirectly via the convection velocity  $\langle u_c \rangle$  ( $y = y_{\text{central inflection pt.}}$ ) as the selected  $u_+$  definition (Eq. 7.6). In the following, a relationship between  $u_+$  and the incoming boundary layer thickness is set up based on previous works. [Elder et al. \(1982\)](#) suggest studying  $u_c$  as a function of the relative boundary layer thickness  $\vartheta = \delta_{99}/L_{x-neck}$ . For  $\lim \vartheta \rightarrow 0$ , the thickness of [Howe's](#) shear layer is truly infinite thin as approximated before in Sect. 4.4. Hence,  $u_{+theo.} = u_+(\vartheta = 0)$  is defined as ideal reference value consistent with [Howe's](#) theory<sup>1</sup>. [Elder](#) uses  $u_{+theo.} = 0.51u_0$  ([Elder, 1980](#)).

In Fig. 8.5  $u_+/u_{+theo.}$  is plotted over  $\vartheta = \delta_{99}/L_{x-neck}$ . Beside [Elder et al.'s](#) results, also more recent results of [Golliard \(2002\)](#) are presented. With Fig. 8.5 [Golliard](#) can conflate all measured opening impedances  $Z_{flow}$  originating from various flow conditions ( $M_0 \in [0.11, 0.12]$ ;  $\delta_{99,neck}/L_{x-neck} \in [0.7, 5]$ ) from [Golliard's](#) B, C, E, F flow cases).

---

<sup>1</sup>Strictly speaking, [Elder et al.](#) were not applying [Howe's](#) theory but [Michalke's](#) linear stability theory of shear layer waves with a comparable convection velocity.

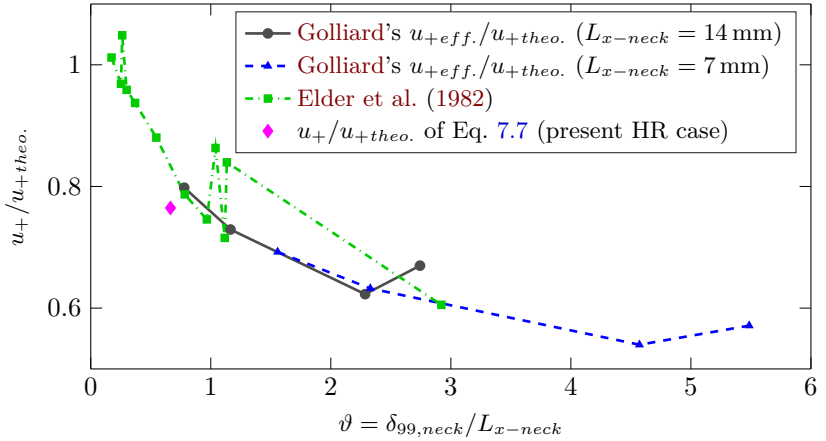


**Figure 8.5:** Portability of the new Helmholtz resonator model, i.e., its characteristic velocity parameter  $u_+$  to different ratios  $\vartheta = \delta_{99} / L_{x-neck}$  of the incoming TBL. Beside previous works by [Elder et al. \(1982\)](#) and [Golliard \(2002\)](#) also, the present HR DNS value is marked.

[Golliard's](#) crucial step to conflate its various measurements is the rescaling of the  $x$ -axis of Fig. 8.1, i.e.,  $St_{neck} = f L_{x,neck} / u_{+eff.}$  with an effective mean velocity  $u_{+eff.}$ . In Fig. 8.5, [Golliard's](#)  $u_{+eff.}$  and the new defined  $u_+ / u_0 = 0.39$  (Eq. 7.7) of the present HR case are normalized by [Elder's](#)  $u_{+theo.}$ , too. With deviations from the mean value of  $u_+ / u_{+theo.} = \pm 0.07$  all results match one another. A general trend of a falling mean velocity with increasing  $\vartheta = \delta_{99} / L_{x-neck}$  is clear: if  $\vartheta$  increases, just a shrinking, undermost fraction of the TBL profile is still able to penetrate in the neck. Since the lower layers of a TBL move slower, a decreasing  $u_+$  value is understandable.

To sum up, the  $u_+$  parameter of the new Helmholtz resonator model can capture the influence of  $\vartheta = \delta_{99} / L_{x-neck}$ . It remains to evaluate the new  $u_+$  definition of Eq. 7.6 also numerically for more than one value of  $\vartheta$ .

## 8.4 Spectral Analysis

The new Helmholtz resonator model points out several characteristic system frequencies, in which resonance conditions of the various physical mechanism are met. To recap all these characteristic frequencies Tab. 8.1 gives an overview of the purely acoustical resonances in Helmholtz numbers, whereas Tab. 8.2 contains fluid-dynamical resonances in Strouhal numbers. In both tables the far left column classifies the physical mechanism:  $M_{n_x n_y n_z}$  are acoustic cavity modes.  $K_n$  are fluid-dynamical KH modes. The three-dimensional mode number index notation  $n_x n_y n_z$  follows Eq. 1.4. The resonance condition related to each mechanism can be determined in various ways. Each column displays a different method to calculate the resonance condition corresponding to a mechanism.

In Tab. 8.1, one possibility to determine  $M_{n_x n_y n_z}$  are the DMD Helmholtz numbers (see next Sect. 8.4.1). A second estimate of the cavity modes  $M_{n_x n_y n_z}$  is given by Eq. 1.4, using the cavity dimensions only (no flow). A third improved calculation of all cavity depth modes of the type  $M_{0n_y 0}$  for  $n_y = 0, 1, 2, \dots$ , is provided by the new Helmholtz resonator model, i.e., by the zeros of its length term  $\Lambda_\delta = 0$  (violet circles in Fig. 8.2). Their maximal error is the interval of the DNS Helmholtz number bin  $\Delta H e_{cavity} = 0.02$  ( $f_{bin} = 50$  Hz).

In Tab. 8.2, one estimate of Strouhal numbers related to dominant KH waves is provided by Tam and Block with Eq. 1.3, being  $u_c = u_+$  (new definition of Eq. 7.6). The new Helmholtz resonator model describes acoustic waves, only. However, another indirect estimate of some KH resonances can be deduced eventually: since the vortex sheet related resistance of Eq. 4.36 causes maximal acoustical amplitudes in case of  $\Delta_r = 0$  (the transfer function Eq. 4.22 peaks), the vortex sheet displacement (i.e., the KH wave amplitude) is presumably locally

**Table 8.1:** Detection of the acoustic cavity modes  $M_{n_x n_y n_z}$  for the main HR case. Each column represents another method and equation to calculate its frequencies. All frequencies in this table are non-dimensionalized in terms of Helmholtz numbers  $He_{cavity}$ , to quickly recover cavity depth modes at  $[0.5, 1, 1.5, \dots]$ .

	DMD of the DNS	Cavity modes	New HR model $\Lambda_\delta = 0$
Type	Eq. 6.13	Eq. 1.4	Eq. 4.23
$M_{000}$	0.12	0.13	0.13
$M_{010}$	0.49	0.50	0.53
$M_{100/001}$	0.74	0.72	
$M_{110/011}$	0.89	0.88	
$M_{020}$	1.02	1.00	1.02
$M_{120/021}$	1.24	1.23	
$M_{200}$	1.46	1.44	
$M_{030}$	1.53	1.50	1.51

**Table 8.2:** Detection of fluid-dynamical KH waves  $K_n$  for the main HR case. Only selected, possible coupled, cavity modes are copied from Tab. 8.1 for comparison. All frequencies in this table are converted into the characteristic Strouhal numbers  $St_{neck}$ . Crossed out KH Strouhal numbers have an insignificant amplitude (see Sect. 8.4.2).

Type	DMD of the DNS Eq. 6.13	Tam and Block formula Eq. 1.3	New HR model	
			$\Delta_r = 0$ Eq. 4.24	$r_{flow} = 0$ Eq. 4.36
$K_1$	0.98	0.92	<del>0.52</del> 0.90	<del>0.52</del> 0.94
$M_{010}$	1.08			
$K_2$	1.60	1.86	<del>1.42</del>	<del>1.33</del>
$M_{100/001}$	1.63			
$K_3$	2.74	2.79		
$M_{120/021}$	2.74			

## 8. Acoustical Results and Discussion

---

maximal, too (qualitatively comparable to the coupling of KH modes with vertically tunneling acoustic waves as described by the fluid-resonant mechanism of Sect. 1.2). While doing so, the energy flux between acoustic and vortex sheet is balanced ( $\Delta_r = 0$ ).  $\Delta_r$  also includes radiation effects (in the form of  $r_{rad}$ , see Eq. 4.14). The pure vortex layer driven resistance is  $r_{flow}$  of Eq. 4.36 only. As possible KH wave maxima, the zeros of  $\Delta_r = 0$  (red stars in Fig. 8.2) and of  $r_{flow} = 0$  (zero-crossings in Fig. 8.1) are listed both in Tab. 8.2.

To assess which non-dimensional frequencies of Tabs. 8.1, 8.2 are most accurately predicted, a DMD (introduced in Sect. 6.1) and a Resolvent Analysis (introduced in Sect. 6.2) is conducted now.

### 8.4.1 Dynamic Mode Decomposition of Pressure

To decompose the DNS snapshots of the main HR case into their spectral components, a DMD is applied below (pseudocode 6.1). Thereby one can relate system modes (full vector fields) to frequencies of interest (scalar values). The full system mode helps to identify the physical mechanism, which is dominant at a particular frequency. As the input of the DMD algorithm, pressure  $xy$ -areas ( $z$ -centered in the middle of the cavity) are used. After execution of the DMD, the resulting modes are normalized by using all snapshots on average (see Sect. 6.1). Selected modes, which correspond to a characteristic non-dimensional frequency listed in Tab. 8.1 or in Tab. 8.2, are shown side by side in Fig. 8.6:

The cavity modes  $M_{n_x n_y n_z}$  can be rediscovered by the structure of their pressure mode inside the cavity. Their corresponding DMD eigenvalues, i.e., Helmholtz numbers listed in Tab. 8.1 or Strouhal numbers listed in Tab. 8.2 are an independent confirmation (based on the raw DNS data) that the new Helmholtz resonator model predicts the correct cavity resonance condition  $\Lambda_\delta = 0$ .

The KH modes occur in the neck region (upper cutout area in Fig. 8.6). They are manifested in alternating positive and negative pressure fluctuations of anti-clockwise and clockwise-spinning vortex cores (Howe's vortex sheet). The next section elaborates how the first three KH modes  $K_{1,2,3}$  presented in Fig. 8.6 could be identified.

## 8. Acoustical Results and Discussion

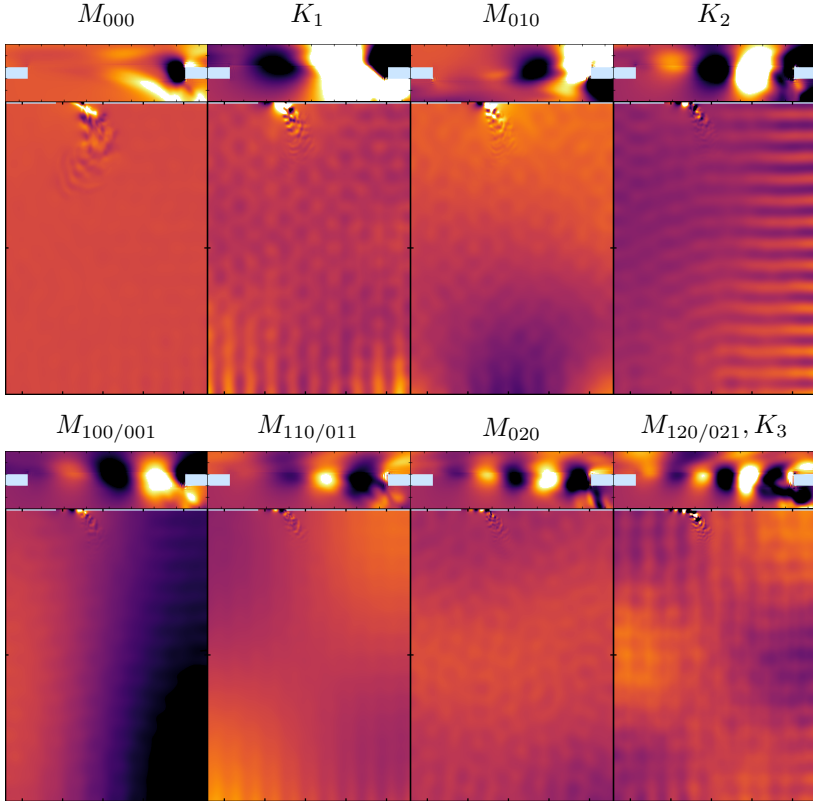
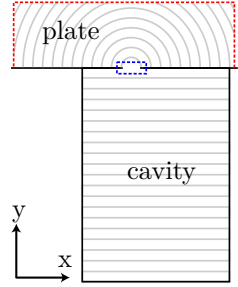


**Figure 8.6:** Selected pressure  $xy$ -modes (eigenvectors) of a Dynamic Mode Decomposition. The real part of the modes is shown. The color bar shows a range of  $\pm 2$  Pa. Pressures, which are exceeding this range, are either white or black. Each mode corresponds to a characteristic non-dimensional system frequency listed in Tab. 8.1 or in Tab. 8.2. For better visibility, each mode shows only a cutout of the DMD input field. The upper, greatly enlarged, cutout presents the neck region with the KH waves. The color of the wall is pale blue. The lower cutout presents the entire cavity with the acoustic cavity modes. In the auxiliary Fig. 8.7 the relative dimensions of these cutout areas are demonstrated. Since  $L_{x-cavity} = L_{z-cavity}$  cavity modes like  $M_{i,j,k}$  have the same frequency as  $M_{k,j,i}$ .

**Figure 8.7:** Auxiliary figure to illustrate the upper cutout area (blue dashed box) of the DMD modes depicted in Fig. 8.6 with respect to the entire calculation domain.



### 8.4.2 Identification of Kelvin-Helmholtz Waves

To detect KH waves and their characteristic Strouhal numbers the DMD pressure modes inside the neck region are evaluated in the following. One-dimensional  $x$ -lines of the  $xy$  pressure modes are extracted at  $y = 0$  (upper plate surface) and plotted over the Strouhal number in Fig. 8.8. In the displayed Strouhal number range between  $St_{neck} \in [0, 3.5]$  the first three KH modes are visible:

$K_1$  is approximately located between  $St_{neck} = 0.5$  and 1 with one positive and one negative pressure vortex core.

$K_2$  is approximately located between  $St_{neck} = 1.5$  and 2 with two positive and two negative pressure vortex cores.

$K_3$  is approximately located between  $St_{neck} = 2.5$  and 3 with three positive and three negative pressure vortex cores.

In contrast to the sharp cavity resonances  $M_{n_x n_y n_z}$ , the KH waves  $K_{1,2,3}$  are widely dispersed over a whole Strouhal number band. Depending, among others, on their interaction with acoustic cavity modes they are more or less pronounced. To find the strongest KH waves in Fig. 8.8, the absolute pressure value of all streamwise locations is added up

## 8. Acoustical Results and Discussion

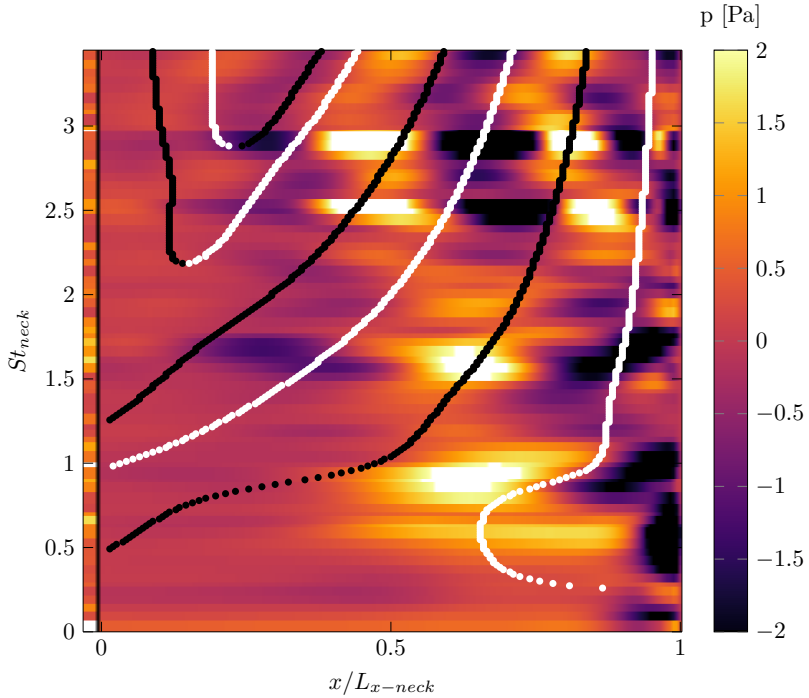


**Figure 8.8:** Series of DMD pressure modes inside the neck (at the neck topside  $y = 0$  and the spanwise neck center) ordered by their respective Strouhal number. The  $x$ -axis is the streamwise coordinate within the neck opening. The  $y$ -axis is  $St_{neck}$ . The very left column does not describe a location of the  $x$ -axis, but is the mean of its absolute row values (average over entire neck), thus highlighting dominant KH waves. For comparison purposes, the dotted black and white lines are just a copy of Fig. 8.9.

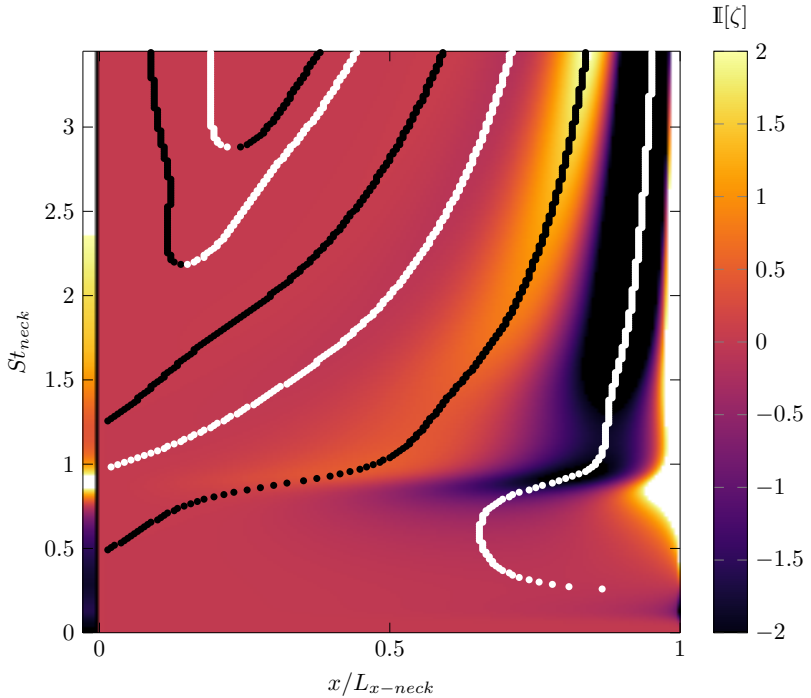


**Figure 8.9:** Vortex sheet displacement modeled by Howe’s theory of a rectangular opening (Eq. 4.30). The very left column does not describe a location of the  $x$ -axis, but is the mean of its absolute row values (average over entire neck), thus highlighting dominant waves. The dotted black and white lines mark the local maxima and minima of the vortex displacement, respectively.

This figure is adapted from Stein and Sesterhenn (2018).

## 8. Acoustical Results and Discussion

---

for each Strouhal number bin, normalized, color-coded and inserted on the left side (column) of the figure. In this way, for each  $K_{1,2,3}$  Strouhal number band, one distinct KH wave is revealed by the DMD at  $St_{neck} = 0.98, 1.60$  and  $2.74$ , respectively. These representative waves are shown in Fig. 8.6 and in Tab. 8.2.

By continuing the discussion of Tab. 8.2 started in Sect. 8.4, the second  $r_{flow}$  zero at  $St_{neck} = 0.94$  is close to a pronounced KH wave identified by the DMD of the raw DNS data at  $St_{neck} = 0.98$ . For the present conditions of the HR case, the first and third zero of  $r_{flow}$  have no visible excited KH waves in Fig. 8.8. Hence they are crossed out in Tab. 8.2. However, the zeros of  $r_{flow}$  might reveal an excited KH wave for another free stream Mach number  $M_0$  as observable in Fig. 8.4, where the first  $r_{flow}$  zero couples with the Helmholtz base mode  $M_{000}$  at  $M_0 \in [0.04, 0.06]$ . Higher KH waves ( $K_2, K_3$ ) begin at  $St_{neck} = 1.5$ . These exceed the scope of Howe’s simplified impedance model, which approaches zero above  $St_{neck} = 1.5$  (see Fig. 8.1). Consequently, even so, nonlinear resonances between the vortex sheet and the acoustics are correctly predicted in the low-frequency range (see Fig. 8.4 of Sect. 8.2.4),  $r_{flow}$  alone has limited use to identify excited KH waves.

Meanwhile, all three KH waves  $K_{1,2,3}$  (most accurately revealed by the DMD) can be estimated (within the fivefold error interval of  $\Delta St_{neck} = 0.05 \leftrightarrow f_{bin} = 50$  Hz) by Eq. 1.3 of Tam and Block, if one knows  $u_c$  a priori (see Tab. 8.2).

### 8.4.3 Vortex Sheet Displacement of Howe’s Conductivity Model

Howe’s impedance Eq. 4.36 of an opening under grazing flow, results from a model of the vortex sheet displacement  $\zeta(x, y)$  of this opening. One can contrast this vortex sheet displacement itself with the pressure

DMD modes of Fig. 8.8. Doing so, a better understanding of Howe’s model is provided, below.

In Fig. 8.9 the numerical solution of the Eq. 4.30 is plotted over the Strouhal number. Because the opening is rectangular, the vortex sheet displacement  $\zeta(x)$  is only  $x$  dependent and constant in spanwise direction. As in Fig. 8.8, the very left column is the sum of all absolute  $|\zeta(x)|$  values summed over  $x$ . The maximum value (white) of this left column at  $St_{neck} = 0.90$  (within the first Strouhal number band stated in Sect. 8.4.2) roughly estimates the dominant  $K_1$  wave, of similar accuracy to the second zero of  $r_{flow}$  or  $\Delta_r$  (cf. Tab. 8.2). Again, because Howe’s model has vanishing contributions above  $St_{neck} = 1.5$  (for instance, see discussion of  $r_{flow}$  at the end of Sect. 8.4.2), analyzing the maxima of  $\zeta$  does not reveal the exact frequencies of higher excited  $K_2, K_3 \dots$  waves.

To highlight all the Strouhal number dependent extrema of the vortex sheet displacement, the minima and maxima are marked by white and black lines, respectively. Qualitatively, the same structures are governing Figs. 8.9 and 8.8: as a general trend, the number of bulges increases with the Strouhal number. Also, the streamwise growth of the shear layer is recognizable by an amplitude, which is increasing with  $x$ .

To conclude this section, one can say that Howe’s vortex sheet displacement model incorporates true physical trends. However, only the low Strouhal number range up to the first  $K_1$  wave at  $St_{neck} \approx 1$  is quantitatively accurate, too.

### 8.4.4 Resolvent Analysis of Characteristic Frequencies

As introduced in Sect. 6.2 the resolvent corresponding to the DMD of Sect. 8.4.1 is calculated according to Eq. 6.15. Fig. 8.10 shows this resolvent in the surroundings of the characteristic DMD modes tabulated in Tabs. 8.1, 8.2. As expected, the DMD eigenvalues  $\lambda$  loosely scatter around a unit circle in the complex plane. The polar coordinate angle is directly related to the Strouhal number of the neck. Eigenvalues (blue crosses) inside the unit circle are damped, while eigenvalues outside the unit circle are excited (during the period of the snapshot series). The contour plot shows the logarithmic pseudospectrum. Under a large number of spectral system components used by the DMD, only the labeled eigenvalues correspond to the classified and distinct mechanisms of Tab. 8.1 and Tab. 8.2. By counting the number of contour lines between two eigenvalues, one can quantify their degree of coupling. It turns out that  $K_2$  and  $M_{100/001}$  are the most coupled, followed by the interaction of  $K_1$ , and  $M_{010}$ . The coupling of  $K_1$  and  $M_{010}$  is also reflected by the broadened  $M_{010}$  peak of Fig. 8.4 above  $M_0 = 0.11$ . All the other classified mechanism are unlinked. This unambiguous conclusion would not have been possible by simply comparing the similarity of their eigenvectors in Fig. 8.6. If the next contour line is far off an eigenvalue, this eigenvalues is sensitive to perturbations such as changed flow conditions or geometry modifications. One example of a sensitive eigenvalue is the Helmholtz base mode  $M_{000}$  with a large surrounding plateau (orange colored). Particularly stable modes are  $M_{110/011}$ ,  $M_{020}$ , and  $K_3, M_{120/021}$ .

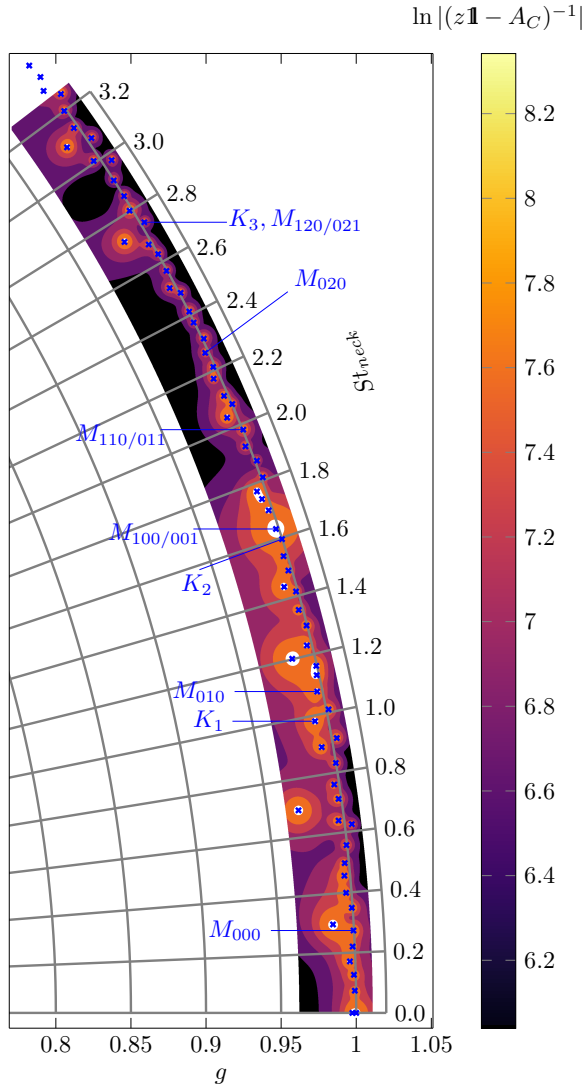


**Figure 8.10:** Resolvent of the DMD companion matrix (see Sect. 8.4.1). The polar coordinate radius  $g$  corresponds to the growth rate; the polar coordinate angle is the Strouhal number. Blue crosses mark eigenvalues. The blue labels of the eigenvalues are given in Tabs. 8.1, 8.2.



# Conclusion

Altogether, by combining and carrying on works by Howe, and Golliard a new sound prediction model of a Helmholtz resonator in turbulent, grazing flow is established (Sect. 8.1). The derivation of the model is based on a DNS. Goody's power spectral density function is selected as the most realistic acoustic source term of a TBL and adapted to the Helmholtz resonator model (Sect. 7.3.2).

The model is validated for low frequencies ( $He_{cavity} \in [0, 0.63]$ ) below the cutoff of higher transverse cavity modes and low Mach numbers from 0.01 to 0.14 (Sect. 8.2). These ranges comply with typical operating conditions of duct systems. (For example, in the present case, the Helmholtz base mode is  $He_{cavity} = 0.12$ .) Even though the new model is linear, successfully resonance conditions are predicted, and the coupling of the acoustical and fluid-dynamical phenomena is correctly represented (cf. Figs. 8.3 and 8.4). One example of this is the non-linear interaction of the Helmholtz base mode and the KH waves of the resonator neck, also experimentally observed and following a Resolvent Analysis of the raw DNS data.

To set up an unprecedented DNS database for the present case a multi-block parallelization method for complex geometries (Appx. D) is developed and implemented. In a weak scaling test a previous single-block parallelization is outperformed (Sect. D.3). New solutions to practical problems of skew-symmetric, finite-differences (like fluid flow around sharp edges) are developed (Sect. B.3).

The physical key point of this thesis is the correct description of the turbulence-acoustic interaction. The understanding of the related energy interchange is vital to predicting acoustical damping

## 9. Conclusion

---

or excitation. So far, Howe's existing theory of this interaction is of limited use, because its governing parameters  $u_+$  and  $\beta$  are defined for idealized conditions only (see Sect. 4.4). Hence, in the case of realistic conditions,  $u_+$  and  $\beta$  have to be fitted each time to match one particular case at least.

To solve this problem and to broaden the applicability of Howe's theory, a most significant contribution of this work is the new definition of  $u_+$  (Sect. 7.4.2) and  $\beta$  (Sect. 7.4.3), which is valid for turbulent background flow or an extended vortex sheet thickness, too (within the ranges mentioned above). This is the primary prerequisite to integrate Howe's theory into the present Helmholtz resonator model (Sect. 4.3). The novel definition of  $u_+$  and  $\beta$  is facilitated by a proceeding analysis of characteristic flow features. To this end, the crucial step is to make the neck vortex sheet (part of Howe's theory) spatially distinguishable from the turbulent background flow (not part of his theory). In Sect. 7.2 this requirement is achieved, using the three inflection points, which are newly identified. Finally,  $u_+$  is specified as the mean velocity at the center of the localized neck vortex sheet (to be precise at the central inflection point).  $1/\beta$  is a measure of the vortex sheet growth at the neck (Sect. 8.2.2). Also the physical existence of interim quantities of Howe's theory, like the vortex sheet displacement  $\zeta$  (Eq. 4.31), is proven through a Dynamic Mode Decomposition of pressure fluctuation snapshots (cf. Figs. 8.8, 8.9).

When applying the new model of a Helmholtz resonator, the user should take care. Because the turbulence-acoustic interaction is based on Howe's simplified impedance model (see Sect. 4.4), the following restrictions are found to be relevant: Different free stream velocities  $u_0$ , frequencies  $f$  and most geometry modifications<sup>1</sup> can be easily studied within the ranges  $He_{cavity} \in [0, 0.63]$ ,  $M_0 \in [0.01, 0.14]$  (Sect. 8.2.4).

---

<sup>1</sup>Eq. 4.30 can be solved for any  $S_{neck}(x, z)$  shape.

---

In contrast, effects, caused by wall thickness  $L_{y-neck}$  modifications or induced by an altered boundary layer thickness  $\delta_{99}$ , require to re-calculate  $u_+$  by evaluating its general definition (Eq. 7.6) for an appropriate reference database (continuation option of this work). As the first proof of concept, Sect. 8.3 demonstrates how an adjusted mean convection velocity  $u_+$  can account for an altered, incoming boundary layer thicknesses  $\delta_{99}$ .

Using the specific  $u_+$ ,  $\beta$  formulas (Eqs. 7.7, 7.8) derived from the present DNS data, and by comparison with experiments by other researchers, it is shown that changes in the frequency or the free stream velocity, have an appropriate impact on the model predictions (Sect. 8.2). Hence, the change of outer parameters is now traceably linked to the governing parameters, which in turn directly update the model predictions. Beside the knowledge gain, the new physically motivated definitions imply an improved design process of industrial applications. The model is based on a modular design (Sect. 4.2), which guarantees a flexible use and expandability.

The Helmholtz resonator model with its generalized parameters  $u_+$  and  $\beta$  is ready for use. An industrial user can directly apply it, by following its summary provided in Sect. 8.1. A priori, rather than by expensive tests, the sound spectrum can be directly tuned for frequencies of interest. Potential applications (Sect. 4.2.2) are duct systems as well as open areas with turbulent grazing flow, i.e., exhaust mufflers, jet engine liners, aircraft wheel wells, car wheel cases, window buffeting, trunk lids and door gaps, pipeline side branches, and wind instruments.



# Thermodynamics

# A

## A.1 The Ideal Gas

This section focuses on compressible gas mechanics. To describe macroscopic particle interactions, the most common approach of gas dynamics is to consider an ideal gas: non-interacting point particles and a simple **equation of state** are assumed, where the density depends only linearly on pressure, temperature, the molar mass  $M$  (gas molecule specific), and the general ideal gas constant  $R$ :

$$\rho(p, T) = \frac{M}{R} \frac{p}{T}. \quad (\text{A.1})$$

Instead of the general gas constant  $R$ , the specific molar mass, i.e., the specific gas constant

$$R_s \equiv \frac{R}{M} \quad (\text{A.2})$$

is often used. The **internal energy** of an ideal gas is given by the sum of all particle movements and interactions.

$$e = \frac{1}{\gamma - 1} \frac{p}{\rho} \quad (\text{A.3})$$

The change of internal energy according to the first law of thermodynamics is given by a heat transport  $dQ$  and a volume-work  $p dV$ :

$$de \equiv dQ - p dV. \quad (\text{A.4})$$

## A. Thermodynamics

---

$e$  is a thermodynamic function of state. Its total differential is

$$de(S, V) = \left( \frac{\partial e}{\partial S} \right)_V dS + \left( \frac{\partial e}{\partial V} \right)_S dV. \quad (\text{A.5})$$

The specific **heat capacity** at a constant volume is defined as energy change per temperature change:

$$C_V \equiv \left( \frac{\partial e}{\partial T} \right)_V. \quad (\text{A.6})$$

To change the variable dependence ( $V \rightarrow p$ ) of a thermodynamic function of state, a Legendre transformation is needed. In chemical systems, the **enthalpy** is often used

$$h(S, p) \equiv e + \frac{p}{\rho}, \quad (\text{A.7})$$

$$dh = dQ + V dp. \quad (\text{A.8})$$

The specific heat capacity at constant pressure is generally defined as entropy change per temperature change:

$$C_p \equiv \left( \frac{\partial h}{\partial T} \right)_p. \quad (\text{A.9})$$

Alternatively, the internal enthalpy of an ideal gas is given by:

$$h = \frac{\gamma}{\gamma - 1} \frac{p}{\rho} = \frac{\gamma}{\gamma - 1} \frac{R}{M} T. \quad (\text{A.10})$$

For the ideal gas, Eq. A.1 and Eq. A.10 imply

$$R/M = R_s = C_p - C_V.$$

The heat capacity ratio is defined as

$$\gamma \equiv \frac{C_p}{C_V} \tag{A.11}$$

and is called the adiabatic exponent or adiabatic gas constant (also known as the isentropic exponent). It follows from Eq. A.10 that the specific heat capacity at constant pressure (see the lower index of Eq. A.9) of an ideal gas is constant:

$$C_p = \frac{h}{T} = \frac{\gamma}{\gamma - 1} \frac{R}{M} = \frac{\gamma}{\gamma - 1} R_s. \tag{A.12}$$

The total energy density and the total enthalpy can be rewritten in terms of  $\rho$ ,  $\mathbf{u}$ ,  $p$  using the internal energy of an ideal gas (Eq. A.3), too:

$$E \equiv \rho e + \rho \frac{|\mathbf{u}|^2}{2} = \frac{p}{\gamma - 1} + \rho \frac{|\mathbf{u}|^2}{2}, \tag{A.13}$$

$$H \equiv h + \frac{|\mathbf{u}|^2}{2} = \frac{\gamma}{\gamma - 1} \frac{p}{\rho} + \frac{|\mathbf{u}|^2}{2}. \tag{A.14}$$

To predict the direction of physical processes, the concept of **entropy**  $s$  is useful. In statistical mechanics, it is defined as a measure of all microscopic states of a system which could be taken. Practically it is the contribution of energy which can not be used for work. In normal irreversible processes, it is therefore always increasing. The second law of thermodynamics expresses this concept as

$$0 \leq ds \equiv \frac{dQ}{T}. \tag{A.15}$$

The reversibility of the process is expressed through  $ds = 0$ . In nature reversible processes are much rarer: linear, acoustic waves are a good approximation. Insertion of the differential enthalpy Eq. A.8 in Eq. A.15

## A. Thermodynamics

---

gives

$$ds = \frac{dh}{T} - \frac{dp}{\rho T}. \quad (\text{A.16})$$

With the definition of the heat capacity and the ideal gas law (Eq. A.1), it follows

$$ds = C_p \frac{dT}{T} - (C_p - C_V) \frac{dp}{p} = C_V \frac{dp}{p} - C_p \frac{d\rho}{\rho}. \quad (\text{A.17})$$

Integration leads to various relations of an ideal gas. One important is

$$0 \leq \frac{s - s_1}{C_V} = \ln \left[ \frac{p}{p_1} \left( \frac{\rho_1}{\rho} \right)^\gamma \right]. \quad (\text{A.18})$$

The latter expression is used to detect which changes of states are physically allowed. In literature, such relations are often referred to as entropy constraint. Such for constant  $s$  the **isentropic relation**

$$\frac{p}{p_1} = \left( \frac{\rho}{\rho_1} \right)^\gamma \quad (\text{A.19})$$

is derived. Pure acoustic waves, can be initialized using a Gaussian pulse in pressure, Eq. A.19 for the related density and zero initial velocity.

# Finite Differences

# B

The **Finite Differences Method** (FDM) discretizes the calculation domain into a grid consisting of nodal points. This implies a pointwise approximate solution that exists only at a gridpoint and depends only on neighboring nodes. The FDM can be implemented particularly effectively if the grid is topologically equivalent to a Cartesian coordinate system (regular structured). Finite differences approximate all the differential operators of the NSEs. In such a discrete form the NSEs become an assignment rule between interacting neighboring nodes. The numerical order of the discretized operators determines the number of interacting neighboring nodes. The clear form of the FDM and the free choice of discretized operators make this method highly adjustable. For example, it is especially easy to obtain high order schemes. The adjustability is the reason why this method is chosen to enforce perfect conservation (Sect. B.2).

The foundation of the FDM is the definition of the derivation:

$$\partial_x u(x) = \lim_{\Delta \rightarrow 0} \frac{u(x + \Delta) - u(x)}{\Delta}. \quad (\text{B.1})$$

A close-meshed three-dimensional grid can approximate all points of the three-dimensional space (physical world). The grid spacing is called  $\Delta$ . In such a way the slope or derivation of any quantity is given by its change between two grid nodes divided by the node difference  $\Delta$ .

Central symmetric methods take into account the isotropy of space and time and treat all local and temporal neighbors equally. Later this equal treatment of all space and time directions is essential to guarantee

## B. Finite Differences

---

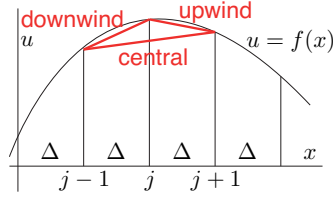


**Figure B.1:** FDM: Downwind, Upwind and Central differences scheme.

conservation laws (see Sect. B.2). In contrast, upwind or downwind methods consider only nearby points of one side (see Fig. B.1).

In the following, Finite Differences operators acting in n-dimensional space on distorted grids with varying node distance are derived.

## B.1 Finite Differences Derivation Schemes

### 1D Grids

Given a variable  $u$  at the  $j^{\text{th}}$  node of a regular one-dimensional grid with a constant node spacing  $\Delta$ , the interaction between two nodes can be expressed by the Taylor series

$$u_{j+n} = \sum_k \frac{(n\Delta)^k}{k!} u_j^{(k)}. \quad (\text{B.2})$$

If  $n$  is a positive integer, Eq. B.2 describes an upwind node (relative to  $j$ ); if  $n$  is a negative integer Eq. B.2 describes a downwind node, respectively. A derivation can be estimated by any combination of neighboring nodes (finite differences):

$$\partial_x u_j = \sum_{m=j-q}^{j+r} \alpha_m u_m. \quad (\text{B.3})$$

The more interacting nodes contribute, the higher can be the resulting order of the discretized operator.

### Upwind 1<sup>st</sup> Order Scheme

Taking into account only the first upwind neighbor leads to the simplest upwind difference quotient:

$$\partial_x u_j = \frac{u_{j+1} - u_j}{\Delta}, \quad (\text{B.4})$$

neglecting errors of the order of  $\Delta \partial_x^2 u_j$  and higher. If a periodic grid is assumed and  $N$  is the total number of nodes, the relation  $u_{j+N} = u_j$  is valid. Written in terms of  $\mathbf{u} = (u_1, u_2, \dots, u_N)^T$  the matrix form is

$$\partial_x \mathbf{u} = D \mathbf{u} \quad \text{with} \quad D = \frac{1}{\Delta} \begin{pmatrix} -1 & 0 & \dots & 0 & 1 \\ 1 & \ddots & \ddots & & 0 \\ 0 & \ddots & -1 & \ddots & \vdots \\ \vdots & \ddots & \ddots & \ddots & 0 \\ 0 & \dots & 0 & 1 & -1 \end{pmatrix}. \quad (\text{B.5})$$

The elements in the upper right or lower left corner of the matrix  $D$  impose periodic conditions. They couple the first and last gridpoints and lead to a zero summing up any column. Derivation of the unit vector  $\mathbf{1} = (1, 1, \dots, 1)^T$  has to hold zero, such the summation of each row gives zero, too.

## Central Differences Scheme of 2<sup>nd</sup> Order

Symmetric combination of one upwind and one downwind neighbor leads to

$$\partial_x u_j = \frac{u_{j+1} - u_{j-1}}{2\Delta} \quad \text{with} \quad D = \frac{1}{2\Delta} \begin{pmatrix} 0 & +1 & 0 & \dots & -1 \\ \vdots & \vdots & \vdots & \vdots & \vdots \\ 0 & -1 & 0 & +1 & 0 \\ \vdots & \vdots & \vdots & \vdots & \vdots \\ +1 & \dots & 0 & -1 & 0 \end{pmatrix}. \quad (\text{B.6})$$

## Distorted Higher Dimensional Grids

FDM techniques are based on structured grids consisting of a quadrilateral grid (physical domain) in 2D or any skew cuboids in 3D. This allows a bijective map of the physical grid nodes to a uniform Cartesian grid (array stored in the computer). Let A be the coordinate system of a uniform Cartesian grid and B any distorted one (quadrilateral in 2D or cuboid in 3D). To apply any operator of the NSE, the variables expressed in the physical basis B (possible distorted) must be transformed into the uniform Cartesian grid A, first.

### Local Basis in 3D

Two three-dimensional coordinate systems are given: A with the vectors named  $\mathbf{r} = (x, y, z)^T$  and the basis  $[\hat{e}_x, \hat{e}_y, \hat{e}_z]$  and B with the vectors  $\boldsymbol{\xi} = (\xi, \eta, \zeta)^T$  and the basis  $[\hat{e}_\xi, \hat{e}_\eta, \hat{e}_\zeta]$ . The coordinate system B is mapped into A by the transformation  $\mathbf{r} = \mathbf{r}(\xi, \eta, \zeta)$ . Such at any given (local) point  $\boldsymbol{\xi}_0 = (\xi_0, \eta_0, \zeta_0)^T$  the basis vectors of B can be expressed

in terms of A by

$$\hat{e}_i(\xi_0, \eta_0, \zeta_0) = \partial_i \mathbf{r}(\xi, \eta, \zeta)|_{\xi=\xi_0} \text{ for } i = \xi, \eta, \zeta. \quad (\text{B.7})$$

## Differential Operators in 3D

The Divergence, the Gradient, and the Laplace operator are (locally) given by

$$\nabla \mathbf{u} = \frac{1}{J} \sum_{i=\xi, \eta, \zeta}^{cyclic} \partial_i (\hat{e}_j \times \hat{e}_k) \mathbf{u}, \quad (\text{B.8})$$

$$\nabla \varphi = \frac{1}{J} \sum_{i=\xi, \eta, \zeta}^{cyclic} \partial_i (\hat{e}_j \times \hat{e}_k) \varphi \quad (\text{B.9})$$

in the uniform Cartesian basis A with  $\mathbf{u} = u\hat{e}_x + v\hat{e}_y + w\hat{e}_z = (u, v, w)^T$ . The Jacobi functional determinant is

$$J(\xi, \eta, \zeta) = \det(\hat{e}_\xi, \hat{e}_\eta, \hat{e}_\zeta) = (\hat{e}_\xi \times \hat{e}_\eta) \hat{e}_\zeta. \quad (\text{B.10})$$

The Laplacian follows by the composition of the Divergence and the Gradient

$$\Delta \varphi(\xi, \eta, \zeta) = \nabla(\nabla \varphi). \quad (\text{B.11})$$

For its explicit calculation the components of the Jacobi matrix tensor  $g_{ij} = \hat{e}_i^T \hat{e}_j$  (for  $i = \xi, \eta, \zeta$ ) are needed.

## B.2 Fully Conservative Finite Differences

This section shows, how to install full conservation properties in the FDM. Instead of utilizing the complex set of discretized NSEs the conservation method is illustrated on the one-dimensional example of a single homogeneous PDE holding one variable  $y$ :

$$\partial_t y + m(y)y = 0, \tag{B.12}$$

where  $m$  is any function performing spatial derivatives  $\partial_x$ . The discretized version looks like

$$\partial_t \mathbf{y} + M(\mathbf{y}) \mathbf{y} = 0, \tag{B.13}$$

where  $M$  is any matrix holding the discretized spatial derivatives. The type of discrete derivation (Upwind, Downwind or Central) is not specified yet. The discrete variable  $\mathbf{y}$  has become a vector. Its entries contain the variable values  $y_i$  at the corresponding gridpoints.

The **theorem of the telescoping sum** states: To guaranty conservation of the Euclidean norm of  $|\mathbf{y}|$  the telescoping sum property  $\sum_i M_{ij} = 0$  is required for each  $j$ .

Trivially the telescoping sum of a column is equal to multiplying the unity vector  $\mathbf{1} = (1, \dots, 1)^T$  from the left. Such the norm of  $y$  changes in time with:

$$\partial_t |\mathbf{y}| = -\mathbf{1} M \mathbf{y}. \tag{B.14}$$

Periodic boundaries always imply  $\mathbf{1} M = 0$  and such guarantee conservation of  $|\mathbf{y}|$ . This is independent of the type of discrete

derivation.

The **theorem of skew symmetry** states: To conserve the norm of quadratic quantities  $|\mathbf{y}|^2$ ,  $M$  has to be skew-symmetric.

A general not purely skew-symmetric PDE (Partial Differential Equation) system  $\partial_t \mathbf{y} + M \mathbf{y} = 0$  can be separated into a skew-symmetric part  $S = (M - M^T)/2$  and a not skew-symmetric contribution  $F = (M + M^T)/2$ :

$$\partial_t \mathbf{y} + S \mathbf{y} + F \mathbf{y} = 0. \quad (\text{B.15})$$

Multiplication from the left with  $\mathbf{y}^T$  leads to the quadratic norm of  $\mathbf{y}$ :

$$\frac{1}{2} \partial_t |\mathbf{y}|^2 + \mathbf{y}^T S \mathbf{y} + \mathbf{y}^T F \mathbf{y} = 0. \quad (\text{B.16})$$

Skew-symmetric forms have lots of useful properties: They are quadratic. The diagonal entries and the determinant is zero. Also, quadratic forms like  $\mathbf{y}^T S \mathbf{y}$  are zero. The latter is easily demonstrated by

$$\begin{aligned} 2\mathbf{u}^T S \mathbf{u} &= \mathbf{u}^T S \mathbf{u} + \underbrace{\mathbf{u}^T S \mathbf{u}}_{\text{scalar}} \\ &= \mathbf{u}^T S \mathbf{u} + (\mathbf{u}^T S \mathbf{u})^T \\ &= \mathbf{u}^T S \mathbf{u} + \mathbf{u}^T S^T \mathbf{u} \\ &= \mathbf{u}^T S \mathbf{u} - \mathbf{u}^T S \mathbf{u} \\ &= 0. \end{aligned}$$

## B. Finite Differences

---

In such a way the conservation of quadratic quantities is guaranteed up to the not skew-symmetric contributions:

$$\partial_t |\mathbf{y}|^2 = -2\mathbf{y}^T F \mathbf{y}. \quad (\text{B.17})$$

The discrete matrix operators of the central derivation schemes (Eq. B.6) with periodic boundaries are always skew-symmetric. In contrast Upwind and Downwind schemes are not skew-symmetric.

The conclusion is: If a central symmetric derivation scheme is selected, the conservation of quadratic quantities is guaranteed. The kinetic energy in the NSEs is precisely such a quadratic quantity.

In case of non-periodic boundaries, central derivation schemes hold not skew-symmetric entries, as well as a non zero telescoping sum. These deviating entries show up only in the vicinity of the boundaries and depict the effect of incoming and outgoing flux. Therefore they are no conservation violating anomalies but a normal physical process.

Hence, the second conclusion is: In case of a central symmetric derivation scheme the not skew-symmetric, sparsely populated matrix  $F$  represents fluxes across the borders of the calculation domain. Thus Eqs. B.14 and B.17 show the total net flux of the quantity  $y$  and  $y^2$  at the boundaries, respectively.

Without a stint, the same procedure can be transferred to proof conservative properties of the discretized NSEs as published in [Reiss \(2015\)](#). Fig. B.2 provides a numerical proof of the conservation properties of the discretized NSE's (Eqs. 5.3 - 5.5).

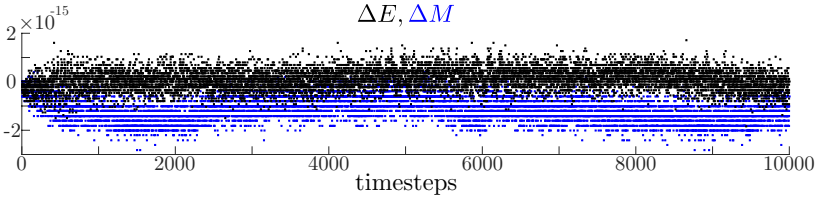


**Figure B.2:** Normalized conservation error at machine precision (double precision floating point format) of mass (marked by blue dots) and total energy (marked by black dots) over 10000 steps. The observable discrete jumps indicate numerical rounding errors in the last digit. A three-dimensional acoustic spherical wave is simulated in a periodic domain.

## B.3 Challenges of Fully Conservative, Skew-Symmetric Finite-Differences

In the following, the challenges for the implementation of the Skew-Symmetric FDM are outlined and possible solutions are presented.

### $\pi$ -Mode Blindness

All central schemes do not perceive oscillations, alternating between direct grid neighbors, i.e., the derivation of  $\mathbf{q} = (+1, -1, +1, -1, \dots)^T$  is zero. This results in a diverging accumulation of energy in this so-called highest  $\pi$ -mode of the grid.

The **solution** is to apply a conservative filter. In the present case, a 4<sup>th</sup>-order Pade-type filter with a late cutoff frequency by [Gaitonde and Visbal \(2000\)](#) is used.

### Order Decay at Boundaries without Ghostpoints

To preserve the necessary telescoping sum property and skew symmetry (see Sect. B.2) of the derivation stencil at the boundary (especially for walls) so-called summation-by parts (SBP) differentiation matrices must be used (Strand, 1994). These split the derivation into two parts. First, a skew-symmetry matrix  $Q$  (partial derivation) with a telescoping sum property is applied to the field (matrix multiplication). Second, a weight matrix  $W$  is pointwise multiplied (for each gridpoint) to complete the partial (incomplete) derivation matrix  $Q$  at terms near the boundary. Hence, a derivation of the field  $\mathbf{u}$  in the  $\xi$  direction becomes

$$\partial_\xi \mathbf{u} = W_\xi .* Q_\xi \mathbf{u}, \quad (\text{B.18})$$

being  $.*$  a pointwise multiplication. Even though the conservation can be preserved this way, it implies an order decay at the boundary always (relative to the inner points).

To **overcome** this restriction, additional degrees of freedoms can be provided by virtual ghostpoints (behind the original boundary). In the present case, symmetric boundary conditions fulfill this purpose (see Sect. C.4).

### No Conservation at Sharp Edges without Ghostpoints

In two- or three-dimensional geometries, fluid may stream around a sharp edge such as, in the present HR case with a rectangular neck opening (see Fig. 2.1). At solid edges ( $270^\circ$  fluid), summation-by parts matrices (cf. Eq. B.18) have weight matrices of the form

$$\partial_\eta W_\xi \neq 0, \quad \partial_\xi W_\eta \neq 0, \quad (\text{B.19})$$

which ruins conservation properties, locally at the edge. In case of a 1<sup>st</sup> order boundary stencil, this problem can be circumvented. However, it remains for higher orders than 1, to the best of the author's knowledge (Jarolin, 2017).

Again, using symmetric boundary conditions with ghostpoints (Sect. C.4), all weight factors are one, and the problem **is solved**.

#### Expensive Time Stepping

Similar to symmetric space discretization, full conservation is only given for symmetric time discretization, too. This requires to use implicit time integration schemes, which are much more expensive than explicit time steppers.

A partial **solution** is to apply an explicit scheme only during the initial, transition period of the simulation. Only if a statistically steady regime is reached and the data collection is started, a conservative, implicit time discretization is used.

Even if an explicit Runge-Kutta scheme is applied, *not all conservation benefits are lost*. This is demonstrated by Brouwer (2016) with Fig. B.3. Brouwer simulated a slightly unresolved test case including small-scale velocity perturbations close to the grid spacing: While increasing the temporal resolution (keeping the total time constant and lowering  $\Delta t = \text{total time}/\text{timesteps}$ ), the total energy conservation error of the conservative, skew-symmetric formulation (Eqs. 5.3 - 5.5) reaches machine precision ( $10^{-15}$ ), while the energy conservation in case of the convective formulation (Eq. 3.13) is limited (at  $10^{-12}$ ).

## B. Finite Differences

---

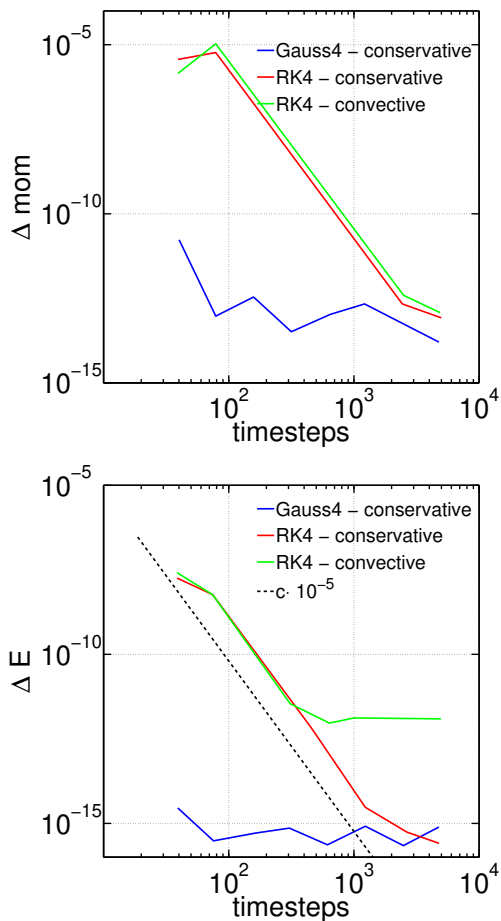


**Figure B.3:** Comparison of the conservative and the convective formulation of the NSE's using an explicit 4<sup>th</sup> order Runge-Kutta and an implicit 4<sup>th</sup> order Gauss-collocation time integrator. On the top, the normalized momentum conservation error and on the bottom side the normalized total energy conservation error is shown.

# Boundary Conditions

# C

This chapter states all numerical boundary conditions needed to conduct the present DNSs. The implementation of physical correct boundary conditions requires knowledge of the surrounding system, which is consistent with the interior.<sup>1</sup>

## C.1 Method of Characteristics

To analyze the dependencies between different parts of flow the method of characteristics is a powerful tool: It delivers a generalized separation of variables to solve a PDE analytically. Furthermore, the method predicts how disturbances evolve and is essential to set boundaries values in a numerical simulation, which do not contradict the inner values. The requirement of this method are quasi-linearity and hyperbolicity:

The hyperbolicity assures that a transformation to uncoupled so-called characteristic variables exists. Physically this is, among others, reflected by a bounded interval of flow dependencies, a finite propagation speed of information in the fluid. For a certain time step, only neighboring particles within a fixed range can interact. Mathematically the hyperbolicity is expressed by diagonalizability of the PDE system. Such a hyperbolic system is given if convective transport dominates and diffusion and friction are negligible (LeVeque, 1992). The Euler equations as a special case of the NSEs have exactly this feature. Since

---

<sup>1</sup>In the author's experience one of the most difficult practical problems of computational fluid dynamics, besides the management of terabytes of data.

### C. Boundary Conditions

---

convective transport is dominating, the Lagrange representation (Eq. 3.15) is a good starting point for the following discussion.

The Euler equations can be written quasi-linear. Their matrix coefficients still couple different vector entries. Consequently, to linearize the PDE matrix, locally constant coefficients need to be assumed.

Making use of the isentropic relation  $c^2 = \gamma p / \rho$  (Eq. 4.5) the Euler equations can be written in the matrix form

$$D_t \mathbf{q} = \partial_t \mathbf{q} + Ax \partial_x \mathbf{q} + Ay \partial_y \mathbf{q} + Az \partial_z \mathbf{q} = \mathbf{0}, \text{ being} \quad (\text{C.1})$$

$$\mathbf{q} = \begin{pmatrix} \rho \\ u \\ v \\ w \\ p \end{pmatrix}, \quad \mathbf{x} = \begin{pmatrix} x \\ y \\ z \end{pmatrix}, \quad \mathbf{u} = \begin{pmatrix} u \\ v \\ w \end{pmatrix}, \quad (\text{C.2})$$

$$Ax = \begin{pmatrix} u & \rho & 0 & 0 & 0 \\ 0 & u & 0 & 0 & \frac{1}{\rho} \\ 0 & 0 & u & 0 & 0 \\ 0 & 0 & 0 & u & 0 \\ 0 & \rho c^2 & 0 & 0 & u \end{pmatrix}, \quad Ay = \begin{pmatrix} v & 0 & \rho & 0 & 0 \\ 0 & v & 0 & 0 & 0 \\ 0 & 0 & v & 0 & \frac{1}{\rho} \\ 0 & 0 & 0 & v & 0 \\ 0 & 0 & \rho c^2 & 0 & v \end{pmatrix},$$

$$Az = \begin{pmatrix} w & 0 & 0 & \rho & 0 \\ 0 & w & 0 & 0 & 0 \\ 0 & 0 & w & 0 & 0 \\ 0 & 0 & 0 & w & \frac{1}{\rho} \\ 0 & 0 & 0 & \rho c^2 & w \end{pmatrix}. \quad (\text{C.3})$$

The tensor  $\mathbf{A}$  describes a system of quasi-linear, first-order partial differential equation. In this case, hyperbolicity is given (Hirsch, 1990b), if the system admits plane wave solutions like

$$\mathbf{q} = \mathbf{q}_0 e^{i(\mathbf{k}\mathbf{x} - \lambda t)} \quad (\text{C.4})$$

with the local wave vector  $|\mathbf{k}| = 1$  and the frequency  $\lambda$ . These frequencies are the characteristic velocities of the system. Insertion of Eq. C.4 in Eq. C.1 leads to

$$[Ax\ kx + Ay\ ky + Az\ kz - \lambda\mathbf{1}] \mathbf{q}_0 = 0, \quad (\text{C.5})$$

which has non-trivial solutions when its determinant

$$\det [Ax\ kx + Ay\ ky + Az\ kz - \lambda\mathbf{1}] \quad (\text{C.6})$$

vanishes. There are five real eigenvalues and eigenvectors (Hirsch, 1990b). The matrix  $Ax\ kx + Ay\ ky + Az\ kz$  can be diagonalized by selecting a local constant set of matrix coefficients and keeping  $\mathbf{k}$  constant. This leads to

$$A = L\lambda L^{-1} \quad (\text{C.7})$$

### C. Boundary Conditions

---

with the local basis of eigenvectors [Hirsch \(1990a\)](#)

$$L = \begin{pmatrix} 1 & 0 & 0 & \frac{\rho}{2c} & \frac{\rho}{2c} \\ 0 & -kz & ky & \frac{kx}{c} & -\frac{kx}{2} \\ 0 & -\frac{kykz}{kx} & -\frac{kx^2+kz^2}{kx} & \frac{ky}{2} & -\frac{ky}{2} \\ 0 & \frac{kx^2+ky^2}{kx} & \frac{kykz}{kx} & \frac{kz}{2} & -\frac{kz}{2} \\ 0 & 0 & 0 & \frac{c\rho}{2} & \frac{c\rho}{2} \end{pmatrix}, \quad (\text{C.8})$$

$$L^{-1} = \begin{pmatrix} 1 & 0 & 0 & 0 & \frac{-1}{c^2} \\ 0 & -kz & 0 & kx & 0 \\ 0 & ky & -kx & 0 & 0 \\ 0 & kx & ky & kz & \frac{1}{c\rho} \\ 0 & -kx & -ky & -kz & \frac{1}{c\rho} \end{pmatrix},$$

and the corresponding diagonal matrix holding the characteristic velocities (eigenvalues):

$$\lambda = \begin{pmatrix} \mathbf{k}u & 0 & 0 & 0 & 0 \\ 0 & \mathbf{k}u & 0 & 0 & 0 \\ 0 & 0 & \mathbf{k}u & 0 & 0 \\ 0 & 0 & 0 & \mathbf{k}u + c & 0 \\ 0 & 0 & 0 & 0 & \mathbf{k}u - c \end{pmatrix}. \quad (\text{C.9})$$

The first Euler equation [C.1](#) can be rewritten by multiplication with  $L^{-1}$  from the left and the introduction of the new characteristic variable  $\mathbf{w} = L^{-1}\mathbf{q}$ :

$$D_t \mathbf{w} = \partial_t \mathbf{w} + (L^{-1} \mathbf{A} L) \bullet \nabla \mathbf{w} = \mathbf{0}. \quad (\text{C.10})$$

Now the initial problem is decoupled into 5 independent scalar equations. The total differential  $D_t \mathbf{w}$  explicitly written is

$$D_t \mathbf{w} = \partial_t \mathbf{w} + \frac{d\mathbf{x}}{dt} \bullet \nabla \mathbf{w}. \quad (\text{C.11})$$

If one compares the last two equations the constancy ( $d\mathbf{w} = L^{-1}d\mathbf{q} = \mathbf{0}$ ) of the characteristic variables  $\mathbf{w}$  in time

$$d\mathbf{w} = \begin{pmatrix} d\rho - \frac{dp}{c^2} \\ dwkx - dukz \\ duky - dvkx \\ \frac{dp}{c^2} + d\mathbf{u} \mathbf{k} \\ \frac{dp}{c^2} - d\mathbf{u} \mathbf{k} \end{pmatrix} = 0 \quad (\text{C.12})$$

along their characteristic paths  $x_i$

$$\frac{d\mathbf{x}_i}{dt} = (L^{-1} \mathbf{A} L)_i \quad (\text{C.13})$$

is clear. This is known as Riemann invariance.

Three perturbation waves propagate each at their characteristic speed  $\mathbf{k}\mathbf{u}$ ,  $\mathbf{k}\mathbf{u} + c$ ,  $\mathbf{k}\mathbf{u} - c$  (Eq. C.9) along their corresponding characteristic path  $\mathbf{x}$ . These three waves are known as entropy wave (contact discontinuity), streamwise-, as well as upstream-propagating acoustic wave, respectively (LeVeque, 1992).

## C. Boundary Conditions

---

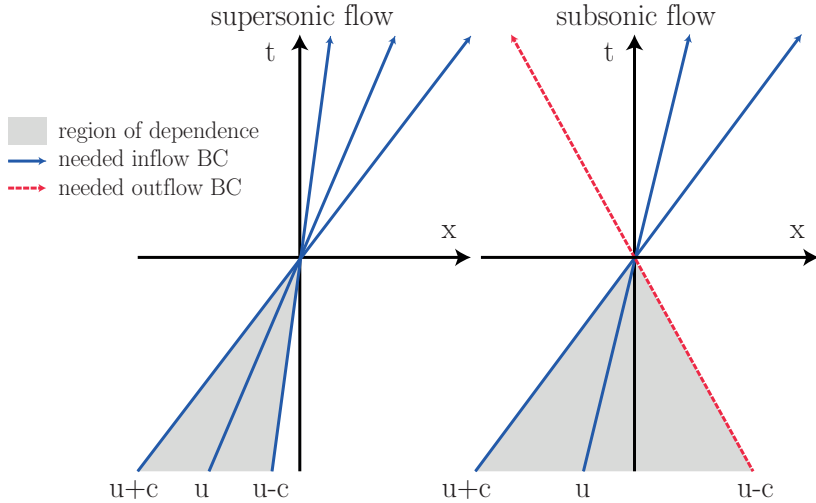


**Figure C.1:** Propagation of characteristic variables in one-dimensional inviscid, diffusionless flow.

## C.2 Non-Reflective Boundary Conditions with Characteristics

The knowledge of flow dependencies is essential to set boundary values. See figure C.1 for an illustration. Arbitrarily, chosen values are contradicting their neighboring inflowing information and cause instabilities. The boundary values  $\mathbf{q}$  which depend on the interior domain have to be defined by the physics of the interior (numerical iteration output  $\mathbf{q}_{int}$ ). Variables which depend on the outside must be set according to the type of boundary (external values  $\mathbf{q}_{ext}$ ). Unfortunately, the boundary values  $\mathbf{q}$  depend on internal and external information at the same time. One physical solution is given if a coordinate transformation  $\mathbf{w} = L^{-1}\mathbf{q}$  to characteristic variables  $\mathbf{w}$

## C.2 Non-Reflective Boundary Conditions with Characteristics

exits. In these coordinates, inflowing and outflowing information are separable by their characteristic velocities (eigenvalues  $\lambda$ ). The vector  $\mathbf{k}$  is chosen orthogonal to the boundary surface of the flow area. If and only if an eigenvalue is

$$\lambda = \mathbf{k}\mathbf{u}, \mathbf{k}\mathbf{u} \pm c < 0, \quad (\text{C.14})$$

its characteristic variable is inflowing. The corresponding characteristic boundary entries  $w$  are set directly according to the boundary information (open boundary condition):

$$w = w_{ext}. \quad (\text{C.15})$$

If and only if an eigenvalue is

$$\lambda = \mathbf{k}\mathbf{u}, \mathbf{k}\mathbf{u} \pm c > 0, \quad (\text{C.16})$$

its characteristic variable is outflowing. Only, in this case,  $w$  is defined by the interior:

$$w = w_{int}. \quad (\text{C.17})$$

Together this can be formalized by

$$\mathbf{w} = \mathbf{w}_{ext} + d\mathbf{w}_{corr.}, \quad (\text{C.18})$$

where the entries of the correction term  $d\mathbf{w}_{corr.}$  are given by the projector  $P$ :

$$dw_{corr.} = P(dw) = \begin{cases} 0 & \text{if } \lambda < 0 \\ dw = w_{int} - w_{ext} & \text{if } \lambda > 0 \end{cases}.$$

## C. Boundary Conditions

---

$P$  acts only on the characteristic variables  $\mathbf{w}$ . Concluding, this described scheme is written in the normal variables  $\mathbf{q}$  utilizing the results of (Sec. C.1):

$$\begin{aligned}\mathbf{q} &= \mathbf{q}_{ext} + L [d\mathbf{w}_{corr.}], \\ &= \mathbf{q}_{ext} + L [P(\mathbf{w}_{int} - \mathbf{w}_{ext})], \\ &= \mathbf{q}_{ext} + L [P (L^{-1}(\mathbf{q}_{int} - \mathbf{q}_{ext}))].\end{aligned}\tag{C.19}$$

### C.3 Non-Reflecting Boundary Conditions with a Sponge Layer

Non-reflective conditions are based on the method of characteristics. They can not deal with viscous phenomena (cf. Sect. C.2)). This causes numerical artifacts: For example, if vortices are partially truncated by the boundary, while they are about to leave the computational domain, strong spurious aerodynamic fluctuation arise. To absorb these numerical artifacts, a sponge layer can be applied. This sponge layer “drags” the instantaneous variables  $\mathbf{q}$  of the NSE towards a reference state  $\mathbf{q}_{ref}$ , given before. This “drag” is implemented as an additional source term of the NSEs right-hand-side:

$$\mathbf{s}_p = -\alpha(\mathbf{x})(\mathbf{q} - \mathbf{q}_{ref}).\tag{C.20}$$

To minimize numerical reflections, both the sponge strength  $\alpha(\mathbf{x})$  and the reference state  $\mathbf{q}_{ref}$  have to be chosen carefully. Here,  $\mathbf{q}_{ref}$  is chosen to be the mean flow field. In contrast to the non-reflective boundary conditions, not just the very last gridpoint of the computational domain is treated but an extended layer. Typically, the sponge strength  $\alpha(x)$  is computed as a function of the distance from the boundaries and

### C.3 Non-Reflecting Boundary Conditions with a Sponge Layer

---

increases from zero at the inside domain to  $\alpha_{max}$  at the boundary (Schulze, 2011):

$$\alpha(x) = \frac{\alpha_{max}}{2} \left\{ 1 + \operatorname{erf} \left( \frac{2}{SL_w} (x - SL_c) \right) \right\}, \quad (\text{C.21})$$

being  $SL_c$  the sponge layer center and  $SL_w$  the sponge layer width. In the present work,  $SL_c$  is set with 20 gridpoints distance to the domain edge, and  $SL_w$  is extended over 40 gridpoints.  $\alpha_{max} = 0.0001$  is determined in test simulations to ensure stable conditions and to minimize spurious reflections. To further increase stability and computational performance an additional quadratic grid stretching can be applied at the end of the computational domain.

Furthermore, a sponge layer can also be combined with other boundary conditions like non-reflecting characteristics.

## C.4 Symmetric Boundary Condition: An Adiabatic, No-Slip Wall

For symmetric boundary conditions, the variables are mirrored on a plane of symmetry, i.e., the wall surface. In case of an adiabatic, no-slip wall the pressure and the density are mirrored symmetrically (anti-node on the wall), while all velocity component are mirrored anti-symmetrically (node on the wall).

Thereby the mirrored points extend the computational grid, which ended originally at the plane of symmetry. This extension zone is also known as ghost layer.

For a central, 4<sup>th</sup> order spatial derivation a five-point-stencil requires a ghost layer of two extra points (the number of secondary diagonals). If the adiabatic, no-slip wall is located at the grid index  $i = 0$  the mirrored ghostpoints at  $i = -2, -1$  are set according to

$$\rho_i = +\rho_{-i}, \quad (\text{C.22})$$

$$p_i = +p_{-i}, \quad (\text{C.23})$$

$$\mathbf{u}_i = -\mathbf{u}_{-i}. \quad (\text{C.24})$$

Directly on the wall, these boundary conditions imply, that  $\mathbf{u}_{i=0}$  is zero and that the wall normal derivations of  $\rho$  and  $p$  are also zero (using a central derivation), such that the wall normal heat flux is zero, too.

# Parallelization

# D

The content of this chapter is adapted from **Stein and Sesterhenn (2019b)**.

The parallelization (MPI) is achieved by a hybrid approach using a multi-block-code with a ghost layer synchronization as well as block internal decomposition into CPUs. Thereby the multi-block-code parallelization strategy is newly developed in the scope of this thesis.

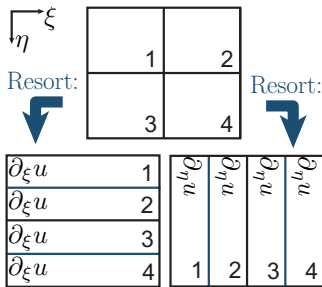


**Figure D.1:** Single-block parallelization scheme: A cube-shaped domain is reshaped according to the direction of the derivatives.

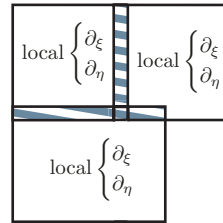


**Figure D.2:** Multi-block parallelization scheme: Interblock communication between differently shaped cubes is accomplished by synchronized layers of overlapping ghostpoints.

## D.1 Single-Block (SB) Parallelization

Before performing a derivative, the single-block scheme redistributes the data between the cores such that stripes in the direction of the desired

## D. Parallelization

---

derivative are created (Fig. D.1). By this, the derivatives are calculated in the whole block at once without dealing with core-to-core interfaces. This is especially useful for compact (i.e., implicit) derivatives. Since units of well-structured data are sent predictably, this procedure is surprisingly efficient. However, if the number of cores gets beyond 1000, the communication overhead becomes the bottleneck. Moreover, the computing space is restricted to a single cartesian block, suitable for large academic research studies with simple geometry.

### D.2 Multi-Block (MB) Parallelization

The most straightforward procedure to parallelize the calculation of large and complex geometries is to split up the grid into manageable sub-pieces, called blocks here (Fig. D.2). To exchange information between neighbored blocks, small overlapping regions are synchronized. The size of this strip of so-called ghost-points matches the width of the derivative stencil. This is especially simple for explicit derivatives, while for compact derivatives, the parallel solution creates extra effort. In contrast to the SB parallelization scheme the optimal number of effective gridpoints per core is reduced by the number of ghostpoints, but therefore the communication overhead almost grows no worse than linear (see weak scaling in Fig. D.4). Besides the more efficient data communication, this method has a further advantage: more general multi-block grids can be created.

Thereby, the SB and the MB parallelization can be combined easily. This allows load balancing and adjustment to different hardware.

## D.3 Scaling Tests

To prove the suitability of the fluid solver on a supercomputer (Tier-0/1 system), its scalability is discussed now. All the following scaling tests were conducted on a Cray XC40 machine with a Haswell E5-2680 V3 processor (30MB cache per core, 24 cores and 128GB RAM per node). For the utilized “Navier-Stokes Fortran” solver the optimal load of gridpoints per core is  $\approx 29^3$ , the “sweet spot”. The measurements of wall time per steps were averaged over 100 steps.

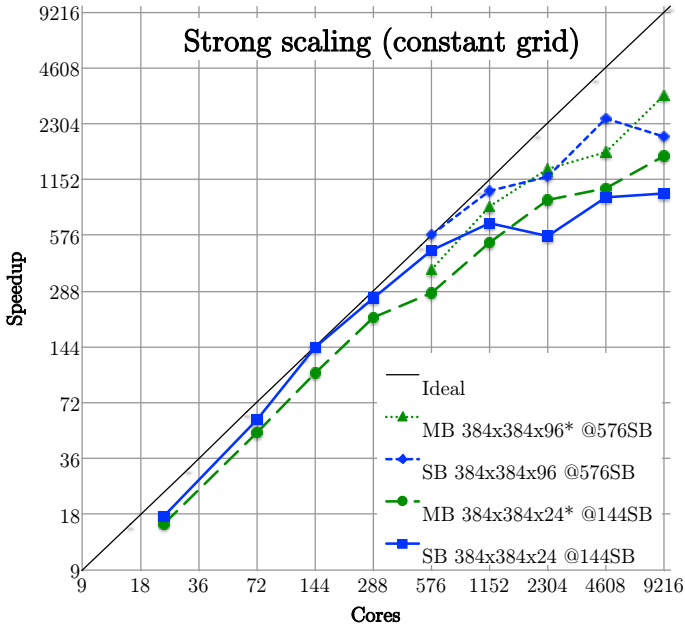


**Figure D.3:** Strong scalability. Two different resolutions of  $384 \times 384 \times 96$ ,  $384 \times 384 \times 24$  and both available parallelization strategies SB, MB are tested. \* denotes the number of computational gridpoints including virtual ghostpoints.

## D. Parallelization

---

In the case of **strong scaling**, all values are rescaled in such a way, that the SB data point closest to the sweet spot exactly lies on the ideal linear curve (both  $384 \times 384 \times 24$  points per 144 cores and  $384 \times 384 \times 96$  points per 576 cores result in  $\approx 29^3$  gridpoints per core). The used rescaling factors are denoted in the legend of Fig. D.3 behind the @-sign. As shown in Fig. D.3 the values below the sweet spot display a super-linear scaling, probably due to a cache overflow (too many gridpoints per core). Values above the sweet spot have no cache bottleneck anymore (few gridpoints per core) and most likely suffer from the communication overhead. To achieve comparability, the MB scaling runs have the same number of physical gridpoints as the SB runs (see legend of Fig. D.3). Since the effective computational domain is bigger due to a ghost layer of four gridpoints per dimension the sweet spot of the MB case is shifted to slightly higher values. This is visible especially for the larger case with a resolution of  $384 \times 384 \times 96$ . To include the loss of runtime because of an increased computational domain the rescaling factor of the SB case is used for the MB case too. Roughly speaking, both parallelization schemes display a similar strong scaling speedup.

Fig. D.4 shows **weak scaling**: In the case of weak scaling the gridpoints per core match the sweet spot  $\approx 29^3$  directly. Therefore, cache effects are minimized. The comparable effective computational domain in the MB case is  $\approx (29 - 4)^3$  with a ghost layer of four points. Again for both parallelization schemes, the same rescaling factor is used: This is the wall time per step and per core in case of 24 cores with SB parallelization. While the SB method loses 50% efficiency between 24 and 9216 cores, the MB method stays close to linear scaling. The present fluid solver always works on the sweet spot (weak scaling), and such makes use of this nearly ideal MB scaling.

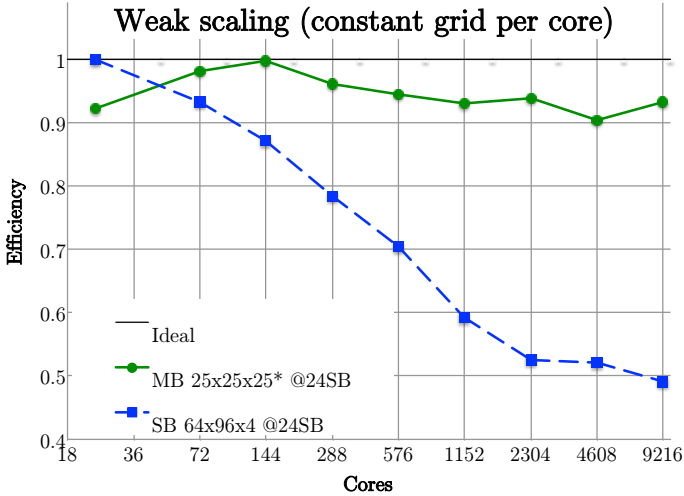


**Figure D.4:** Weak scalability at the sweet spot of  $64 \times 96 \times 4 \approx (25 + 4)^3$  gridpoints per core. With more cores, the MB parallelization strategy has much better efficiency than the SB scheme. \* denotes the number of physical gridpoints excluding virtual ghostpoints.

## Informative Value of Strong Scaling Tests

An issue rarely mentioned is the manipulability of strong scaling tests: With increasing core number the reduction of cache/RAM overflow can be equally balanced with an increase of the communication overhead. Such two problems cancel out each other and result in ideal scaling. Fig. D.5 provides an example (SB parallelization). The upper spuriously ideal curve is rescaled at 512 cores and calculated with  $81^3$  gridpoints per core, while the lower curve is rescaled at 32 cores and calculated with  $32^3$  gridpoints per core. In the second case, the problem size reflects the sweet spot of the program, with a minimized cache overflow. This case holds an actual informative value of the communication overhead above

## D. Parallelization

---

32 cores ( $x$ -axis of Fig. D.5) and of the cache overflow below 32 cores (super linear scaling). In the first spuriously ideal case the problem size is 16 times bigger and such implies heavy cache/RAM overflow superposed with communication overhead. The presented ideal scaling curve has no informative value.

As done here, it is recommended to invest some time to identify the machine dependent optimal load of gridpoints per core (sweet spot) of the program by starting with a low number of gridpoints per core first, which excludes cache/RAM exhaustion effects.

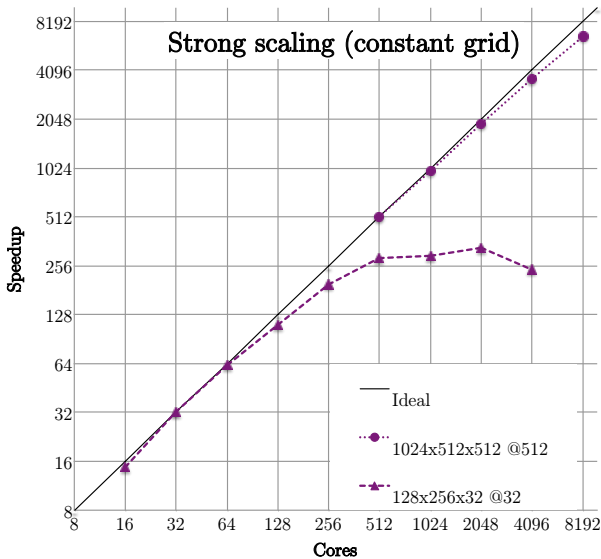


**Figure D.5:** Example of the manipulability of strong scaling tests. The upper spuriously ideal curve is normalized at 512 cores with  $81^3$  gridpoints per core, causing cache/RAM overflow and communication overhead at once. The lower curve is calculated on the same supercomputer solving the same problem but is normalized at 32 cores with  $32^3$  gridpoints per core, mainly causing communication overhead.

# My Publications

## Original Papers

- Bengoechea, S., **Stein, L.**, Reiss, J., Sesterhenn, J.: Numerical Investigation of Reactive and Non-reactive Richtmyer-Meshkov Instabilities. In: Active Flow and Combustion Control 2014, pp. 343–361. Springer (2014). [https://doi.org/10.1007/978-3-319-11967-0\\_21](https://doi.org/10.1007/978-3-319-11967-0_21)
- Stein, L.**, Reiss, J., Sesterhenn, J.: Numerical Simulation of a Resonant Cavity: Acoustical Response Under Grazing Turbulent Flow. New Results Numer. Exp. Fluid Mech. XI **136**, 671–681 (2018). [https://doi.org/10.1007/978-3-319-64519-3\\_60](https://doi.org/10.1007/978-3-319-64519-3_60)
- Stein, L.**, Sesterhenn, J.: How to Predict the Sound Spectrum of a Helmholtz Resonator under Grazing Turbulent Flow. In: Fortschritte Der Akustik - DAGA 2018 44. Jahrestagung Für Akustik, ISBN 9783939296133, pp. 497–500. Deutsche Gesellschaft für Akustik, Munich (2018)
- Stein, L.**, Sesterhenn, J.: An acoustic model of a Helmholtz resonator under a grazing turbulent boundary layer. Acta Mech. **230** (2019a). <https://doi.org/10.1007/s00707-018-2354-5>
- Stein, L.**, Sesterhenn, J.: Direct Numerical Simulation of Turbulent Flow Past an Acoustic Cavity Resonator. High Perform. Comput. Sci. Eng. ' 18 (2019b). [https://doi.org/10.1007/978-3-030-13325-2\\_16](https://doi.org/10.1007/978-3-030-13325-2_16)

## Conferences

- Stein, L.**, Reiss, J., Sesterhenn, J.: Reactive Compressible Flows with Skew Symmetric Schemes. In: GAMM Jahrestagung - 84th Annual Meeting. Gesellschaft für Angewandte Mathematik und Mechanik, Novi Sad (2013)
- Stein, L.**, Sesterhenn, J.: Direct Numerical Simulation of a Helmholtz resonator excited by a low Mach number turbulent flow. In: 11th International ERCOFTAC Symposium on Engineering Turbulence Modelling and Measurements. European Research Community on Flow, Turbulence and Combustion, Palermo (2016a)
- Stein, L.**, Sesterhenn, J.: Numerical Simulation of a Resonant Cavity. In: 20. DGLR-Fach-Symposium. Deutsche Strömungsmechanische Arbeitsgemeinschaft, Braunschweig (2016b)
- Stein, L.**, Sesterhenn, J.: Modelling of a Liner driven by a Turbulent Boundary Layer. In: 4. Workshop Strömungsschall in Luftfahrt, Fahrzeug- Und Anlagentechnik. Deutsche Gesellschaft für Akustik e.V., Vienna (2017a)
- Stein, L.**, Sesterhenn, J.: Pressure Statistics Modification of a Turbulent Boundary Layer Due to the Presence of a Helmholtz Resonator. In: European Turbulence Conference 16. European Mechanics Society, Stockholm (2017b)
- Stein, L.**, Sesterhenn, J.: Acoustic Model of a Helmholtz Resonator Under Grazing Turbulent Flow. In: Computational Experiment in Aeroacoustics. Kaliningrad (2018a)
- Stein, L.**, Sesterhenn, J.: How to Predict the Sound Spectrum of a Helmholtz Resonator under Grazing Turbulent Flow. In: DAGA - 44th German Annual Conference on Acoustics ISBN 9783939296133, pp. 497–500. Deutsche Gesellschaft für Akustik, Munich (2018b)

# Supervised Master Theses

Gourdazi, A.: Temperature effects on aeroacoustics of a subsonic jet flow from an open pipe (2018)

Jarolin, K.: Randbedingungen mit scharfen Ecken für erhaltende Finite-Differenzen-Verfahren (2017)

Kruse, P.: Untersuchung der Dynamik des Helmholtz-Resonators mittels modaler Zerlegung (2015)



# References

- Ahuja, K., Mendoza, J.: Effects of Cavity Dimensions, Boundary Layer, and Temperature on Cavity Noise With Emphasis on Benchmark Data To Validate Computational Aeroacoustic Codes. Tech. Rep. 4653, NASA, Georgia Institute of Technology (1995)
- Alamo, J.C., Jiménez, J.: Estimation of turbulent convection velocities and corrections to Taylor’s approximation. *J. Fluid Mech.* **640**, 5 (2009)
- Alessio, S.M.: Digital Signal Processing and Spectral Analysis for Scientists. Springer (2016)
- Anderson, J.D.: Fundamentals of Aerodynamics. McGraw-Hill Series in Aeronautical and Aerospace Engineering, 2nd ed edn. McGraw-Hill, New York (1991)
- Arguillat, B., Ricot, D., Bailly, C., Robert, G.: Measured wavenumber: Frequency spectrum associated with acoustic and aerodynamic wall pressure fluctuations. *The J. Acoust. Soc. Am.* **128**, 1647–1655 (2010)
- Bijl, H.: Computation of flow at all speeds with a staggered scheme. PhD Thesis, TU Delft, Delft University of Technology (1999)
- Bistrián, D.A., Navon, I.M.: Comparison of optimized Dynamic Mode Decomposition vs POD for the shallow water equations model reduction with large-time-step observations. *Int. J. Numer. Meth. Fluids* p. 25 (2014)
- Blake, W.K.: Turbulent boundary-layer wall-pressure fluctuations on smooth and rough walls. *J. Fluid Mech.* **44**(04), 637 (1970)
- Brès, G.A., Colonius, T.: Three-dimensional instabilities in compressible flow over open cavities. *J. Fluid Mech.* **599**, 309–339 (2008)
- Brouwer, J.: A Study of Transonic Shock-wave/boundary-layer Interactions Using Conservative, Skew-symmetric Finite-differences. Ph.D. thesis, Technischen Universität Berlin (2016)
- Brouwer, J., Reiss, J., Sesterhenn, J.: Conservative Finite Differences as an Alternative to Finite Volume for Compressible Flows. In: Fuhrmann, J.,

## REFERENCES

---

- Ohlberger, M., Rohde, C. (eds.) *Finite Volumes for Complex Applications VII- Methods and Theoretical Aspects*, vol. 77, pp. 169–176. Springer International Publishing, Cham (2014)
- Cammilleri, A., Gueniat, F., Carlier, J., Pastur, L., Memin, E., Lusseyran, F., Artana, G.: POD-spectral decomposition for fluid flow analysis and model reduction. *Theor. Comput. Fluid Dyn.* **27**(6), 787–815 (2013)
- Chase, D.: The character of the turbulent wall pressure spectrum at subconvective wavenumbers and a suggested comprehensive model. *J. Sound Vib.* **112**(1), 125–147 (1987)
- Chen, K.K., Tu, J.H., Rowley, C.W.: Variants of Dynamic Mode Decomposition: Boundary Condition, Koopman, and Fourier Analyses. *J. Nonlinear Sci.* **22**(6), 887–915 (2012)
- Coles, D.: The law of the wake in the turbulent boundary layer. *J. Fluid Mech.* **1**(02), 191 (1956)
- Dequand, S., Hulshoff, S., Hirschberg, a.: Self-sustained oscillations in a closed side branch system. *J. Sound Vib.* **265**(2), 359–386 (2003a)
- Dequand, S., Luo, X., Willems, J., Hirschberg, A.: Helmholtz-Like Resonator Self-Sustained Oscillations, Part 1: Acoustical Measurements and Analytical Models. *AIAA J.* **41**(3), 408–415 (2003b)
- Driest, E.R.V.: On Turbulent Flow Near a Wall. *J. Aeronaut. Sci.* **23**(11), 1007–1011 (1956)
- East, L.: Aerodynamically induced resonance in rectangular cavities. *J. Sound Vib.* **3**(3), 277–287 (1966)
- Ehrenfried, K.: *Strömungsakustik: Skript zur Vorlesung*. No. 1 in *Berliner Hochschulskripte*. Mensch-und-Buch-Verlag, Berlin (2004)
- Elder, S.A.: Edgetones versus pipetones. *The J. Acoust. Soc. Am.* **64**(6), 1721–1723 (1978)
- Elder, S.A.: Forced oscillations of a separated shear layer with application to cavity flow-tone effects. *The J. Acoust. Soc. Am.* **67**(3), 774–781 (1980)

## REFERENCES

---

- Elder, S.A., Farabee, T.M., DeMetz, F.C.: Mechanisms of flow-excited cavity tones at low Mach number. *J. Acoust. Soc. Am.* **72**(2), 532–549 (1982)
- Eldredge, J., Bodony, D., Shoeybi, M.: Numerical Investigation of the Acoustic Behavior of a Multi-Perforated Liner. In: 28th AIAA Aeroacoustics Conference. American Institute of Aeronautics and Astronautics (2007)
- Förner, K., Tournadre, J., Martinez-Lera, P., Polifke, W.: Scattering to Higher Harmonics for Quarter Wave and Helmholtz Resonators. *AIAA J.* **55**(4), 1194–1204 (2017)
- Gaitonde, D.V., Visbal, M.R.: Pade-Type Higher-Order Boundary Filters for the Navier-Stokes Equations. *AIAA J.* **38**(11), 2103–2112 (2000)
- Gloerfelt, X.: Cavity noise (Lecture) (2009)
- Gloerfelt, X., Berland, J.: Turbulent boundary-layer noise: Direct radiation at Mach number 0.5. *J. Fluid Mech.* **723**, 318–351 (2013)
- Gloerfelt, X., Bogey, C., Bailly, C.: LES of the noise radiated by a flow over a rectangular cavity. In: ERCOFTAC Workshop on LES for Acoustics, pp. 1–12 (2002)
- Gloerfelt, X., Lafon, P.: Direct computation of the noise induced by a turbulent flow through a diaphragm in a duct at low Mach number. *Comput. Fluids* **37**(4), 388–401 (2008)
- Goldschmidt, V.W., Young, M.F., Ott, E.S.: Turbulent convective velocities (broadband and wavenumber dependent) in a plane jet. *J. Fluid Mech.* **105**(-1), 327 (1981)
- Golliard, J.: Noise of Helmholtz-resonator like cavities excited by a low Mach-number turbulent flow. Ph.D. thesis, University of Poitiers (2002)
- Goody, M.: Empirical Spectral Model of Surface Pressure Fluctuations. *AIAA J.* **42**(9), 1788–1794 (2004)
- Gordner, A.: Numerische Simulation nichtlinearer Aeroakustik bei kleinen Machzahlen. Dissertation, Ruprecht-Karls-Universität Heidelberg (2005)

## REFERENCES

---

- Grace, S., Howe, M., Horan, K., Grace, S., Howe, M., Horan, K.: The influence of grazing flow on the Rayleigh conductivity of an aperture of arbitrary shape. In: 3rd AIAA/CEAS Aeroacoustics Conference. American Institute of Aeronautics and Astronautics (1997)
- Grace, S.M., Horan, K.P., Howe, M.S.: The Influence of Shape on the Rayleigh Conductivity of a Wall Aperture in the Presence of Grazing Flow. *J. Fluids Struct.* **12**(3), 335–351 (1998)
- Guarini, S.E., Moser, R.D., Shariff, K., Wray, A.: Direct numerical simulation of a supersonic turbulent boundary layer at Mach 2.5. *J. Fluid Mech.* **414**, 1–33 (2000)
- Guéniat, F., Mathelin, L., Pastur, L.R.: A dynamic mode decomposition approach for large and arbitrarily sampled systems. *Phys. Fluids* **27**(2), 025,113 (2015)
- Hémon, P., Santi, F., Amandolèse, X.: On the pressure oscillations inside a deep cavity excited by a grazing airflow. *Eur. J. Mech. - B/Fluids* **23**(4), 617–632 (2004)
- Hersh, A., Walker, B., Celano, J.: Helmholtz Resonator Impedance Model, Part 1: Nonlinear Behavior. *AIAA journal* **41**(5) (2003)
- Hirsch, C.: Numerical Computation of Internal and External Flows - Volume 2: Computational Methods for Inviscid and Viscous Flows. John Wiley & Sons (1990a)
- Hirsch, C.: Numerical Computation of Internal and External Flows. Vol. 1: Fundamentals of Numerical Discretization. 1 edn. John Wiley & Sons (1990b)
- Hirschberg, A., Rienstra, S.W.: An Introduction to Aeroacoustics (2017)
- Hopkins, E.J., Inouye, M.: An evaluation of theories for predicting turbulent skin friction and heat transfer on flat plates at supersonic and hypersonic Mach numbers. *AIAA J.* **9**(6), 993–1003 (1971)
- Howe, M.: Influence of cross-sectional shape on the conductivity of a wall aperture in mean flow. *J. Sound Vib.* **207**(5), 601–616 (1997a)
- Howe, M.S.: The influence of mean shear on unsteady aperture flow, with application to acoustical diffraction and self-sustained cavity oscillations. *J. Fluid Mech.* **109**(-1), 125 (1981a)

## REFERENCES

---

- Howe, M.S.: On the Theory of Unsteady Shearing Flow over a Slot. *Philos. Transactions Royal Soc. A: Math. Phys. Eng. Sci.* **303**(1475), 151–180 (1981b)
- Howe, M.S.: Edge, cavity and aperture tones at very low Mach numbers. *J. Fluid Mech.* **330**, 61–84 (1997b)
- Howe, M.S.: *Acoustics of Fluid-Structure Interactions*. Cambridge monographs on mechanics (1998)
- Hu, N., Appel, C., Herr, M., Ewert, R., Reiche, N.: Numerical Study of Wall Pressure Fluctuations for Zero and Non-Zero Pressure Gradient Turbulent Boundary Layers. In: 22nd AIAA/CEAS Aeroacoustics Conference (2016)
- Hwang, Y., Bonness, W.K., Hambric, S.A.: Comparison of semi-empirical models for turbulent boundary layer wall pressure spectra. *J. Sound Vib.* **319**(1-2), 199–217 (2009)
- Iqbal, A., Selamet, A.: A two-dimensional computational study of the flow effect on the acoustic behaviour of Helmholtz resonators. *Int. J. Veh. Noise Vib.* **6**, 130–148 (2010)
- Kim, J., Hussain, F.: Propagation velocity of perturbations in turbulent channel flow. *Phys. Fluids A: Fluid Dyn.* **5**(3), 695–706 (1993)
- Koch, W.: Acoustic Resonances in Rectangular Open Cavities. *AIAA J.* **43**(11), 2342–2349 (2005)
- Kooijman, G., Hirschberg, A., Golliard, J.: Acoustical response of orifices under grazing flow: Effect of boundary layer profile and edge geometry. *J. Sound Vib.* **315**(4-5), 849–874 (2008)
- Kook, H., Mongeau, L.: Analysis of the Periodic Pressure Fluctuations Induced By Flow Over a Cavity. *J. Sound Vib.* **251**(5), 823–846 (2002)
- L.D. Landau, E.M. Lifshitz: *Fluid Mechanics*. Butterworth-Heinemann (2011)
- Lele, S.K.: Compact finite difference schemes with spectral-like resolution. *J. Comput. Phys.* **103**(1), 16–42 (1992)
- LeVeque, R.J.: *Numerical Methods for Conservation Laws*. Birkhäuser, Basel (1992)
- Ma, R., Slaboch, P.E., Morris, S.C.: Fluid mechanics of the flow-excited Helmholtz resonator. *J. Fluid Mech.* **623**, 1 (2009)

## REFERENCES

---

- Michalke, A.: On Spatially Growing Disturbances in an Inviscid Shear Layer. *J. Fluid Mech.* **23**(3), 521–544 (1965)
- Morinishi, Y.: Skew-symmetric form of convective terms and fully conservative finite difference schemes for variable density low-Mach number flows. *J. Comput. Phys.* **229**(2), 276–300 (2010)
- Morkovin, M.: Effects of compressibility on turbulent flows. *Mécanique de la Turbul.* **367** (1962)
- Morse, P.M., Feshbach, H.: *Methods of Theoretical Physics. International Series in Pure and Applied Physics.* McGraw-Hill, Boston, Mass (1953)
- Morse, P.M., Ingard, K.U.: *Theoretical Acoustics.* 1 edn. Princeton University Press, Princeton, N.J (1968)
- Munjaj, M.L.: *Acoustics of Ducts and Mufflers with Application to Exhaust and Ventilation System Design.* Wiley (1987)
- Peat, K.S., Ih, J.G., Lee, S.H.: The acoustic impedance of a circular orifice in grazing mean flow: Comparison with theory. *The J. Acoust. Soc. Am.* **114**(6), 3076–3086 (2003)
- Pirozzoli, S., Bernardini, M.: Turbulence in supersonic boundary layers at moderate Reynolds number. *J. Fluid Mech.* **688**, 120–168 (2011)
- Pirozzoli, S., Bernardini, M., Grasso, F.: Characterization of coherent vortical structures in a supersonic turbulent boundary layer. *J. Fluid Mech.* **613** (2008)
- Pirozzoli, S., Bernardini, M., Grasso, F.: Direct numerical simulation of transonic shock/boundary layer interaction under conditions of incipient separation. *J. Fluid Mech.* **657**, 361–393 (2010)
- Poinsot, T.J., Lele, S.K.: Boundary conditions for direct simulations of compressible viscous flows. *J. Comput. Phys.* **101**, 104–129 (1992)
- Pope, S.: *Turbulent Flows.* Cambridge University Press (2000)
- Radavich, P.M., Selamet, A., Novak, J.M.: A computational approach for flow-acoustic coupling in closed side branches. *The J. Acoust. Soc. Am.* **109**(4), 1343 (2001)

## REFERENCES

---

- Reichardt, H.: Vollständige Darstellung der turbulenten Geschwindigkeitsverteilung in glatten Leitungen. *Zeitschrift für Angewandte Math. und Mech.* **31**(7), 208–219 (1951)
- Reiss, J.: A Family of Energy Stable, Skew-Symmetric Finite Difference Schemes on Collocated Grids: A Simple Way to Avoid Odd–Even Decoupling. *J. Sci. Comput.* **65**(2), 821–838 (2015)
- Roche, J.M., Leylekan, L., Delattre, G., Vuillot, F.: Aircraft Fan Noise Absorption: DNS of the Acoustic Dissipation of Resonant Liners. In: 30th AIAA Aeroacoustics Conference (2009)
- Rockwell, D.: Prediction of Oscillation Frequencies for Unstable Flow Past Cavities. *J. Fluids Eng.* **99**(2), 294 (1977)
- Rockwell, D., Naudascher, E.: Self-Sustained Oscillations of Impinging Free Shear Layers. *Annu. Rev. Fluid Mech.* **11**(1), 67–94 (1979)
- Rossiter, J.: Wind-Tunnel Experiments on the Flow over Rectangular Cavities at Subsonic and Transonic Speeds. *Aeronaut. Res. Council. Reports Memo.* **3438** (1964)
- Rowley, C.W., Colonius, T., Basu, A.J.: On self-sustained oscillations in two-dimensional compressible flow over rectangular cavities. *J. Fluid Mech.* **455**, 315–346 (2002)
- Rowley, C.W., Mezić, I., Bagheri, S., Schlatter, P., Henningson, D.S.: Spectral analysis of nonlinear flows. *J. Fluid Mech.* **641**(Rowley 2005), 115–127 (2009)
- Rudy, D.H., Strikwerda, J.C.: A nonreflecting outflow boundary condition for subsonic navier-stokes calculations. *J. Comput. Phys.* **36**(1), 55–70 (1980)
- Salze, E., Bailly, C., Marsden, O., Jondeau, E., Juve, D.: An experimental characterisation of wall pressure wavevector-frequency spectra in the presence of pressure gradients. In: 20th AIAA/CEAS Aeroacoustics Conference. American Institute of Aeronautics and Astronautics (2014)
- Schlichting, H.: *Boundary-Layer Theory*. 7 edn. McGraw-Hill (1979)
- Schmid, P., Sesterhenn, J.: Dynamic Mode Decomposition of numerical and experimental data. In: American Physical Society, 61st Annual Meeting of the APS Division of Fluid Dynamics (2008)

## REFERENCES

---

- Schmid, P.J.: Dynamic mode decomposition of numerical and experimental data. *J. Fluid Mech.* **656**, 5–28 (2010)
- Schmid, P.J.: *Stability and Transition in Shear Flows*. Springer (2012)
- Schulze, J.: Adjoint based Jet-Noise Minimization. Ph.D. thesis, Technischen Universität Berlin (2011)
- Selle, L., Nicoud, F., Poinso, T.: Actual Impedance of Nonreflecting Boundary Conditions: Implications for Computation of Resonators. *AIAA J.* **42**(5), 958–964 (2004)
- Sesterhenn, J.: A characteristic-type formulation of the Navier-Stokes equations for high order upwind schemes. *Comput. Fluids* **30**, 37–67 (2001)
- Stanislas, M., Perret, L., Foucaut, J.M.: Vortical structures in the turbulent boundary layer: A possible route to a universal representation. *J. Fluid Mech.* **602** (2008)
- Strand, B.: Summation by Parts for Finite Difference Approximations for  $d/dx$ . *J. Comput. Phys.* **110**(1), 47–67 (1994)
- Subbareddy, P.K., Candler, G.V.: A fully discrete, kinetic energy consistent finite-volume scheme for compressible flows. *J. Comput. Phys.* **228**(5), 1347–1364 (2009)
- Tam, C., Block, P.: On the tones and pressure oscillations induced by flow over rectangular cavities. *J. Fluid Mech.* **89**(02), 373 (1978)
- Tam, C., Ju, H., Jones, M., Watson, W., Parrott, T.: A computational and experimental study of slit resonators. *J. Sound Vib.* **284**, 947–984 (2005)
- Tam, C.K., Ju, H., Jones, M., Watson, W., Parrott, T.: A computational and experimental study of resonators in three dimensions. *J. Sound Vib.* **329**(24), 5164–5193 (2010)
- Tang, S.: On Helmholtz resonators with tapered necks. *J. Sound Vib.* **279**(3-5), 1085–1096 (2005)
- Tissot, G., Cordier, L., Benard, N., Noack, B.R.: Model reduction using Dynamic Mode Decomposition. *Comptes Rendus Mécanique* **342**(6-7), 410–416 (2014)

## REFERENCES

---

- Towne, A., Cavalieri, A.V.G., Jordan, P., Colonius, T., Schmidt, O., Jaunet, V., Brès, G.A.: Acoustic resonance in the potential core of subsonic jets. *J. Fluid Mech.* **825**, 1113–1152 (2017)
- Trefethen, L.N.: Spectra and Pseudospectra. In: Ainsworth, M., Levesley, J., Marletta, M. (eds.) *The Graduate Student's Guide to Numerical Analysis '98*, vol. 26, pp. 217–250. Springer Berlin Heidelberg, Berlin, Heidelberg (1999)
- Viazzo, S., Dejoan, A., Schiestel, R.: Spectral features of the wall-pressure fluctuations in turbulent wall flows with and without perturbations using LES. *Int. J. Heat Fluid Flow* **22**(1), 39–52 (2001)
- White, F.: *Viscous Fluid Flow*. 3 edn. Mac Graw Hill (2006)
- Yamouni, S., Sipp, D., Jacquin, L.: Interaction between feedback aeroacoustic and acoustic resonance mechanisms in a cavity flow: A global stability analysis. *J. Fluid Mech.* **717**, 134–165 (2013)
- Yang, Y., Rockwell, D., Lai-Fook Cody, K., Pollack, M.: Generation of tones due to flow past a deep cavity: Effect of streamwise length. *J. Fluids Struct.* **25**(2), 364–388 (2009)





In this thesis, for the first time, a Direct Numerical Simulation of a three-dimensional Helmholtz resonator under turbulent grazing flow is conducted, and an unprecedented database is set up. A universal acoustic model of a Helmholtz resonator in a turbulent flow is derived, based on the new numerical database, previous theories by Howe, and experiments by Golliard. This acoustic model stands out through its uniquely defined and physically meaningful parameters, instead of fitted constants dependent on expensive test series. The new model enables the user to understand and to trace back how a modification of design parameters (geometry, fluid condition) affects the sound spectrum. It simplifies the design process of cavity absorbers.

